

AN ABSTRACT OF THE THESIS OF

Kei-Wean Calvin Yang for the degree of Doctor of Philosophy


in Electrical and Computer Engineering presented on

October 23, 1981

Title: Electrical and Optical Measurements on a.c. Thin-film Electro-  
luminescent Devices

Signature redacted for privacy.

Abstract approved: \_\_\_\_\_

 S.J.T. Owen

Development of a suitable thin-film technology has stimulated research in, and production of, a.c. thin film electroluminescent (ACTFEL) devices. The aim of this thesis is to provide a better understanding of the physical processes associated with the device characteristics of such ACTFEL devices. The unique phenomena exhibited by these devices leads to a variety of possible novel display applications. Since the device is still in the experimental stage of development few studies have been made of the physical processes leading to the observed phenomena. This is in marked contrast to other areas of semiconductor device research in which the physical processes responsible for device behavior are well understood.

The results of detailed device characterization, along with an interpretation of the physical processes responsible, are discussed in this thesis. Included here are the basic electrical, optical and thermal properties of the device as well as its hysteresis behavior which

enables inherent memory devices to be fabricated. The hysteresis characteristic allows the sample to be set in either an emissive or non-emissive mode when subjected to the same excitation voltage.

A model for the interpretation of the hysteresis behavior is presented which describes the physical processes leading to a negative resistance effect within the thin film, in this case Mn doped ZnS. The negative resistance instability in turn is used to explain the hysteresis in the brightness/voltage characteristic. Computer simulations of the model provide information on how to improve these memory characteristic and certain improvements in device behavior have been verified experimentally.

© Copyright by Kei-Wean Calvin Yang  
October 23, 1981  
All rights reserved

ELECTRICAL AND OPTICAL MEASUREMENTS ON A.C.  
THIN-FILM ELECTROLUMINESCENT DEVICES

by

Kei-Wean Calvin Yang

A THESIS

submitted to

Oregon State University

in partial fulfillment of  
the requirements for the  
degree of

Doctor of Philosophy

Completed October 23, 1981

Commencement June 1982

## ACKNOWLEDGEMENTS

I would like to express my sincere thankness to my adviser Professor S. John T. Owen for his constant support, encouragement, advising, and suggestions. Without his assistance, this dissertation would never have been accomplished over the time frame that had involved.

I also like to thank Professors Thomas K. Plant and Leland C. Jensen for their kind assistance throughout this thesis work. The effort that Professor Plant had contributed during the initiation of the EL measurement laboratory is especially acknowledged.

Thanks are due to Mr. David H. Smith for many fruitful discussions and suggestions. Thanks are also due to Dr. Christopher N. King for many helpful comments and for the supply of the ACTFEL devices that were used in this research work.

I would like to thank my parents for their encouragement as well as their effort to provide me with the opportunity to acquire an advanced education out of an extremely difficult financial situation.

Special thanks are due to Fanling, my wife, for her ever lasting encouragement, advice, and assistance, so that I can concentrate on my research without having to worry about any otherwise inevitable tasks. I also have benefited immensely from my wife's scientific background, the windowed thermally released charge (WTRC) and the residual field induced charge (RFIC) measurements that were developed in this thesis work are a direct result of many brainstorming discussions with her.

The constant support of Mr. John J. McCormick and financial assistance from the Display Research Department at Tektronix, Inc. is heartily appreciated.

## TABLE OF CONTENTS

I	INTRODUCTION . . . . .	1
	1.1 History . . . . .	1
	1.2 Outline of Thesis . . . . .	3
II	EXPERIMENTAL . . . . .	6
	2.1 Sample Fabrication . . . . .	6
	2.2 Experimental Apparatus . . . . .	8
III	THE PHYSICS OF DEVICE OPERATION AND DEVICE CHARACTERISTICS .	14
	3.1 Light Emission Mechanism . . . . .	14
	3.2 The Manganese Ion Excitation Mechanism . . . . .	23
	3.3 The Average Brightness and The Frequency Saturation Phenomenon . . . . .	28
	3.4 The Brightness vs. Driving Voltage Curves (B-V curves), and The Hysteresis Behavior . . . . .	34
	3.5 The Polarization Phenomenon . . . . .	42
	3.6 Writing and Erasing of a ZnS:Mn ACTFEL Device Having Inherent Memory Effect . . . . .	52
	3.7 The Aging Effect . . . . .	57
	3.8 A Model for The Electrical Writing and Erasing Process . . . . .	61
IV	TIME RESOLVED ELECTROLUMINESCENT SPECTRA . . . . .	69
	4.1 Experimental Technique . . . . .	69
	4.2 Time Resolved Spectra . . . . .	71
	4.3 Discussion . . . . .	74
V	THE TEMPERATURE EFFECT . . . . .	81
	5.1 Introduction . . . . .	81
	5.2 Experimental . . . . .	81
	5.3 Results and Analysis . . . . .	82
	5.3.1 Effects on Electroluminescent Brightness . . .	82
	5.3.2 Effects on Polarization . . . . .	86
	5.3.3 Variations of Radiation Decay Time with Temperature . . . . .	89
	5.3.4 Excitation Efficiency of $Mn^{+2}$ Ions . . . . .	94
	5.3.5 Hysteresis Variation with Temperature . . . . .	99
	5.4 Summary . . . . .	101
VI	THERMALLY RELEASED AND RESIDUAL FIELD INDUCED CHARGE MEASUREMENT . . . . .	103
	6.1 Introduction . . . . .	103
	6.2 The Windowed Thermally Released Charge Measurement (WTRC) . . . . .	104
	6.3 The Residual Field Induced Charge Measurement (RFIC) .	114
	6.4 Discussion . . . . .	124

VII	THE PHOTOCONDUCTIVITY MEASUREMENT . . . . .	125
	7.1 Introduction . . . . .	125
	7.2 Experimental . . . . .	127
	7.3 Results and Analysis . . . . .	134
	7.4 Summary . . . . .	143
VIII	A MODEL FOR THE NEGATIVE RESISTANCE EFFECT AND ITS IMPLICATIONS ON THE ELECTRICAL CONTROL OF HYSTERESIS IN ACTFEL DEVICES. .	146
	8.1 Introduction . . . . .	146
	8.2 The Negative Resistance Model . . . . .	149
	8.3 Transition Between The Hysteretic and Nonhysteretic States Via Electrical Control . . . . .	164
	8.4 Discussions . . . . .	168
IVI	CONCLUSIONS . . . . .	170
	BIBLIOGRAPHY . . . . .	174

## LIST OF FIGURES

<u>Figure</u>		<u>Page</u>
2.1	A crossectional view of the a.c. thin film electroluminescent device	7
2.2	Measurement system for investigations of the time resolved spectra	10
2.3	The crossectional view of the dewar system	11
2.4	The spectra response of the monochromatic light source	13
3.1	Schematic representation of the 3d electrons of the $Mn^{+2}$ ion	15
3.2	Schematic diagram of the $Mn^{+2}$ ion energy level in free space and a cubic lattice environment	17
3.3	The electroluminescent spectra at different temperatures	20
3.4	Configurational diagram of a $Mn^{+2}$ ion in cubic lattice	21
3.5	Mechanisms for the $Mn^{+2}$ ion excitation process	25
3.6	An equivalent circuit diagram of the ZnS:Mn ACTFEL device	27
3.7	The timing diagram of the driving voltage, the induced current and the emitted light pulses	29
3.8	Average brightness versus driving frequency plot	32
3.9	The B-V curve of a low Mn-doping sample	35
3.10.(a)	The B-V curve of a high Mn-doping sample	37
3.10.(b)	The B-V curve of a single conduction filament	38
3.10.(c)	The equivalent circuit of a hysteric sample	40
3.11	Effectiveness of the erasing pulses versus its amplitude	41
3.12	The hysteresis of the driving pulse width effect	41
3.13	Amplitude of the light pulses as a function of the previous driving voltage polarity	44
3.14	The Sawyer and Tower circuit for measuring the polarization effect	45



3.15	The Q-V diagram of the ZnS:Mn ACTFEL device	49
3.16	The P-V curves for samples with different Mn-doping	53
3.17	The pulse with dependence of the B-V curve and the writing mechanism for the pulse width modulation effect	55
3.18	The aging effect on the B-V curve	59
3.19	The timing diagram of the driving voltage and the sensing capacitor voltage	60
4.1	Measurement system for the time resolved spectra	70
4.2	The full EL light pulse versus time	72
4.3	Low pass filtered EL emission ( $\lambda < 500$ nm) versus time	72
4.4	The time resolved spectra of a sample with no Mn-doping	73
4.5	The time resolved spectra of a ZnS:Mn sample with non-hysteric doping	75
4.6	The linear plot of EL intensity at various wavelengths	76
4.7	EL emission spectra for a heavily doped hysteric sample at $t=0$	77
4.8	Model of the self-activated centers	79
5.1	The measurement system for investigating temperature effect	83
5.2	Polarization versus peak driving voltage at various temperatures	85
5.3	The B-V curves at various temperatures	87
5.4	Normalized brightness and polarization as a function of temperature	88
5.5	Relative "leakage" current versus temperature	90
5.6	Possible decay channels of a $Mn^{+2}$ ion	92
5.7	Normalized plot of light output versus time at different device temperatures	95
5.8	Linear plot of loght output versus time with temperature as a parameter	97
5.9	Possible hot electron energy distribution at two different device temperatures	100

5.10	Hysteresis width versus temperature for various samples	100
6.1	The crosssectional view of the special sample used to study the insulator traps	105
6.2	The band diagram of the special sample when first subjected to an external biasing voltage	105
6.3	The system diagram for the thermally released charge measurement	106
6.4	The control signal timing diagram for the WTRC measurement	109
6.5	The transient current at various device temperatures	110
6.6	The WTRC signal plotted against device temperature	112
6.7	The Arrhenius plot of the WTRC data shown in figure 6.6	113
6.8	The Frenkel-Poole effect	115
6.9	The timing diagram of the biasing voltage and the total amount of charge that had flown in the RFIC experiment	116
6.10	The schematic diagram of the RFIC measurement	119
6.11	The ZnS layer field enhancement effect	121
6.12	The RFIC signal for three different Mn-doped samples	123
7.1	The schematic diagram for the photoconductivity experiment	128
7.2	The system and control timing diagram for the photoconductivity experiment	133
7.3	The spectra response of the monochromatic light source	135
7.4	The Photoconductivity response of a sample	136
7.5	The long wavelength photoconductivity response for the sample in figure 7.4	137
7.6	The semi-log plot of the EL photoconductivity versus incident photon energy	139
7.7	The relative EL photoconductivity at 5400Å as a function of the device Mn-doping concentration	139
7.8	The photoconductivity spectra response of an EL sample at both the fresh and the aged status	141

7.9	The long wavelength photoconductivity response under either the electrical or the optical erasure methods	142
8.1	The B-V diagram of a single conduction filament	147
8.2	The Q-V diagram of a hysteric EL sample	148
8.3	The band diagram of a metal-Zns-metal system under an external biasing voltage	151
8.4	The band diagram of the ACTFEL device when under an external biasing voltage	155
8.5	The computer simulation of the field enhancement effect	158
8.6	The Q-V diagram of an asymmetric ACTFEL sample with different insulators on either side of the ZnS layer	163
8.7	The waveform used for electrical control of the device hysteresis behavior	167
8.8	The effect of the spike driving waveform on the B-V diagram of a hysteretic sample	167

# Electrical and Optical Measurements on a.c. Thin-film Electroluminescent Devices

## INTRODUCTION

### 1.1 History

The most efficient way for a machine to communicate interactively with a human operator is by way of an information display device. Current display technology is dominated by the cathode ray tubes, (CRT). Although CRT's provided satisfactory performance in terms of the display contrast, brightness, addressability, and long operation life time, they have several undesirable features. CRT's are too bulky, they consume too much power and require very high voltages for operation, the manufacturing costs are high, and it is difficult to make a large display screen out of them. To circumvent these problems, alternative flat panel display devices which are capable of displaying large volume of information at the same time have been proposed. These flat panel displays are either passive or active devices.

Of the passive display devices, the most promising are liquid crystal and electrophoretic displays [1]. These devices operate on the principle of controlled scattering of ambient light and therefore are suitable for applications in environments where the ambient light level is high. Active display devices are able to emit light by themselves. Such devices includes the plasma displays and electroluminescent displays. One unique feature of the electroluminescent display devices, not common to other flat panel displays, is that they

are completely solid state and therefore suitable for automated mass production.

The electroluminescent devices can be roughly classified into four categories [2]: d.c. powder electroluminescent, a.c. powder electroluminescent, d.c. thin film electroluminescent, and a.c. thin film electroluminescent. Among these four types, the a.c. thin film electroluminescent, or ACTFEL, devices exhibit many interesting features and are currently receiving the most attention. In this thesis, the optical and electrical characteristics of ZnS:Mn ACTFEL devices are examined.

The basic structure of ACTFEL devices was first reported by Inoguchi et al [3], recent works showed that such devices have demonstrated long operation life time, high brightness and high efficiency, multiple choice of colors, and a memory effect, they also have a relatively easy fabrication procedures for making large area panels. These characteristics, especially those of high brightness and memory effect, have made the ACTFEL devices the most promising for matrix addressed flat panel displays. Because when addressing a matrixed display device, it is necessary to use multiplexing technique to minimize the driving electronics. As the panel size increases, the total pixel<sup>\*</sup> number to be multiplexed also increases in proportion to the size of the display area. This forces the addressing repetition rate to decrease. However, by taking advantage of the memory effect of the ACTFEL devices, the whole panel can be excited at the

---

\* A pixel is the smallest addressable displaying area of a display device.

same time under a low frequency sustaining voltage, and selective areas where light emission is required, can be triggered on by addressing them once with a writing voltage. This will relax the requirement of a high multiplexing rate to address large matrixed display panels, whilst still maintaining a high level of brightness.

Another major application of the memory effect allows the ACTFEL device to operate as the faceplate of a storage CRT [4]. The unique features of the device will provide image storage having selectively erasable, extremely high resolution (essentially limited by the resolution of the addressing electron beam), and practically unlimited number of grey scales capabilities. Many of the detailed physical processes behind ACTFEL device operation are under investigation. This thesis will be devoted to an examination of the electrical and optical characteristics of such devices.

## 1.2 Outline of Thesis

The subjects of chapter II include descriptions of the detailed device fabrication procedures as well as a discussion of the experimental procedures used in this study. Special attention is given to the experimental techniques for ensuring accurate data acquisition. The physics of device operation is introduced in chapter III, together with a discussion of the detailed electronic transitions associated with the electroluminescent property of the ACTFEL device. The intermediate portion of the chapter presents the basic device characteristics with the intent of preparing a sufficient technical background for the remainder of this thesis. Interesting phenomena

which are discussed include the device brightness saturation effect, the aging effect, the memory effect, and the polarization effect. In the latter sections, some important physical quantities which determine the crucial device characteristics are outlined. A theoretical analysis on the electrical writing and erasing mechanism of a memory ACTFEL device is also presented.

Chapter IV describes self-activated deep-center luminescence in terms of measurements on the time resolved electroluminescence spectra of the ACTFEL device. This self-activated luminescent band provides a convenient way for qualitative measuring of the average kinetic energy of the hot electrons which are associated with the device dissipative conduction current. The relationships among this self-activated emission band, the normal manganese emission band, and the device manganese doping concentration, are also studied.

The effects of temperature on the performance of the ZnS:Mn ACTFEL devices are discussed in chapter V. Investigations of the physical phenomena responsible for the device characteristics are made, based on systematic observations of the optical and electrical characteristics as a function of device temperature.

Chapter VI introduces two newly developed experimental techniques for thermally probing the trap structures within different portions of the ACTFEL devices. These techniques are called the windowed thermally released charge (WTRC) measurement and the residual field induced charge (RFIC) measurement. The former examines the trap distribution within samples consisting of a single layer of insulating films sandwiched between two conductor electrodes, and the latter is

an attempt to survey specifically the traps within the ZnS layer of the ACTFEL devices. The investigation of the effects of optical probing on the devices by studying their photoconductivity spectra response via another new technique for the measurement of photoconductivity appears in chapter VII. This new measuring technique has many unique features which reveal phenomena which cannot be obtained by the traditional a.c. measurement. With this technique, the existence of deep lying impurity states, as well as the self-activated centers, are investigated. Studies are also made on the effects of aging and  $Mn^{+2}$  doping on the device photoconductivity, and the results are in good agreement with the previous thermal probing data obtained from the RFIC measurement.

Chapter VIII is devoted to the modeling of negative resistance behavior associated with the device memory behavior. The directions that are suggested by this model for the improvement of the negative resistance effect are compared with experimental results. This model is then used in an attempt to achieve electrical control of the memory effect.

Finally, a summary of the new interesting results of this investigation is presented and some suggestions for future work that may extend and take advantage of this research, is outlined.



## EXPERIMENTAL

### 2.1 Sample Fabrication

The structure of the ACTFEL samples examined throughout this thesis work is based on that first reported by Inoguchi et al [3]. The cross-sectional view of the device is shown in figure 2.1 and the detailed procedures of the sample fabrication process are now described.

A solid film of indium tin oxide (ITO) transparent conductor, which serves as the front electrode of the device, was first coated onto a 7059 glass substrate. This substrate was then mounted onto the planetary of a vacuum chamber for deposition of the insulator and the active layer films. In order to ensure a better film stoichiometry, during the deposition of both of these films, the glass substrate temperature was maintained at a relatively high level, about 250°C [4]. The reduced evaporant sticking coefficient, due to the high substrate temperature was counteracted by raising the dynamic pressure of each evaporant via the hot wall technique [5]. The material used for the two insulator films was either  $Y_2O_3$  or  $Y_2O_3$  and  $Al_2O_3$  double layers, which were evaporated with an electron beam gun.

In the deposition of the Mn doped ZnS active layer, two separate quartz oscillators were used to control the co-evaporation rate of both the ZnS pure material and the manganese metal sources. The resultant manganese mole concentration, specified as the ratio of

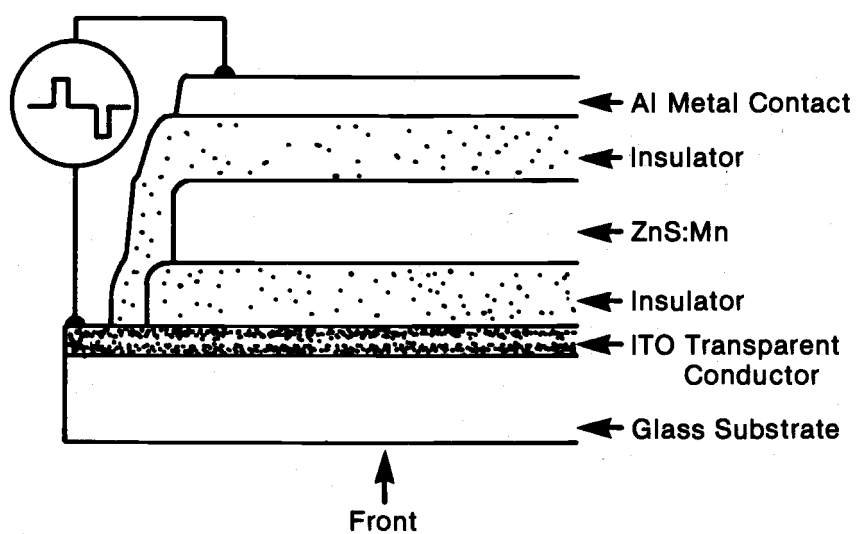


Figure 2.1 A crosssectional view of a ZnS:Mn a.c. thin film electroluminescent device.

the number of manganese atoms to that of the zinc atoms, was measured by the atomic absorption method [6]. For the test samples used here, the  $\text{Mn}^{+2}$  concentration ranges from 0 to 2.8 mole%. The crystal structure of the ZnS film was found, from X-ray analysis, to be of poly-type and predominantly cubic structure with its [111] axis perpendicular to the surface of the glass substrate [6], [7].

After deposition of the insulator and the active layer films, the sample was annealed at 450°C in vacuum for one hour to improve its luminescence efficiency. The rear aluminum electrode, having a diameter of 0.125 inch, was then defined through a metal mask via electron beam evaporation of a 99.999% pure aluminum ingot.\*

## 2.2 Experimental Apparatus

The excitation voltage which was used to study the devices electroluminescence consisted a sequence of alternating polarity, narrow pulses with variable pulse width and pulse rise time. The repetition rate of the excitation voltage ranged from 50 to 2KHZ. The displacement and dissipative currents induced by the excitation voltage were monitored by the so called sensing capacitor technique [8]. A linear low-leakage polyester capacitor connected in series with the ACTFEL sample, integrates the overall device current, the individual current contribution being obtained by examining the voltage waveform across this sensing capacitor [9].

For the time resolved electroluminescence spectra analysis, a Jerrell-Ash model 82-210 1/4 meter monochromator, together with a

---

\* supplied by The Varian Inc.

set of Melles Griot colored glass order sorting filters, was used to select the wavelengths of the incident light. The output light was detected with an RCA 4840 photomultiplier tube. The photomultiplier output was terminated in a  $50\Omega$  resistor and therefore had a response time of less than 20ns. The output signal was then fed into a Princeton Applied Research model 162 boxcar signal averager via two model 164 gated integrators. The sampling aperture delay time of the gated integrators can vary from 10ns up to 500  $\mu$ s after the triggering pulse. An even longer delay time can be obtained, if necessary, via a custom installed timing resistor inside the 162 boxcar averager main frame.

This system readily allows the measurement and recording of fast varying signals. Figure 2.2 is an example of the system set up for the time resolved spectra measurement. Detailed set up for other measurements are described in the relating chapters.

The studies of temperature effects were carried out with a home made dewar system, figure 2.3, which is capable of covering a temperature range from 90K to 500K. Two quartz windows on the side wall of the dewar facilitated the optical measurements without any significant attenuation of light transmission over the photon energy range studied. The dewar temperature was controlled by a proportional temperature controller, which provided a very stable temperature control to within  $\pm 0.1^\circ\text{C}$ , and the sample temperature was measured with a copper-constantan, type T, thermocouple.

The monochromatic light used in the photoconductivity measurement was generated by a Baush & Lomb 45 watt quartz halogen light source,

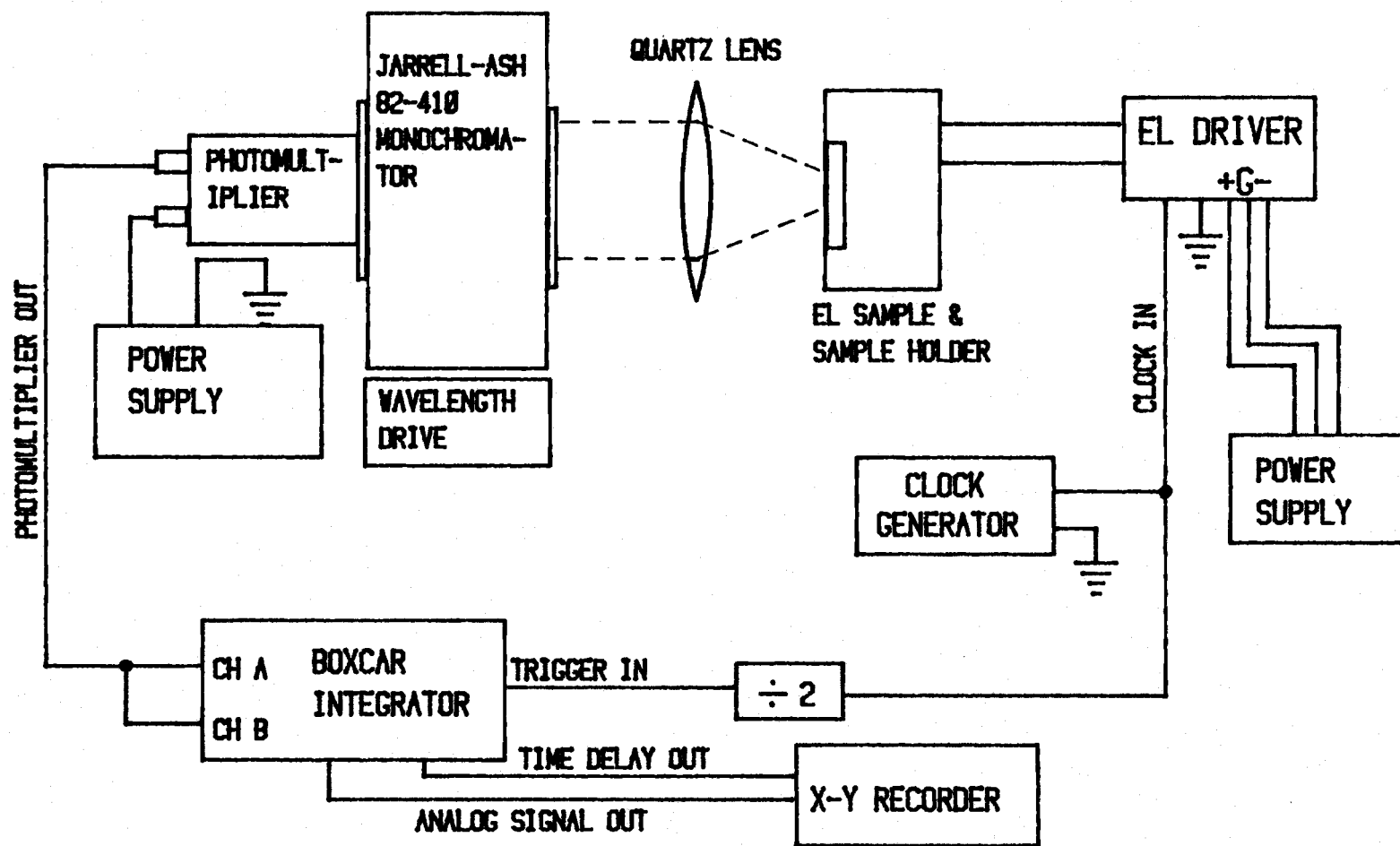


Figure 2.2 Measurement system for investigations of time resolved spectra.

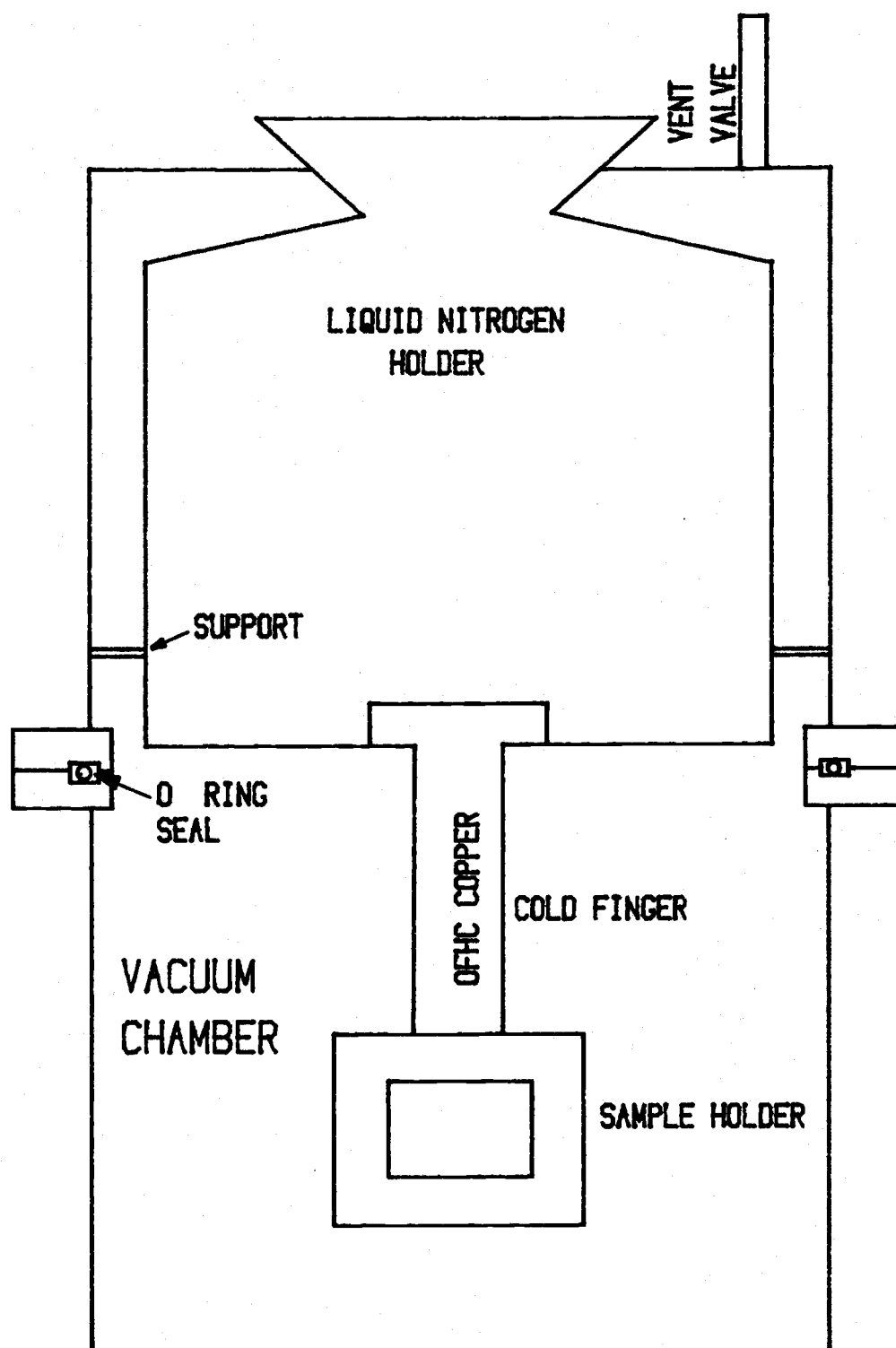


Figure 2.3 The cross-sectional view of the dewar system.

in conjunction with the Jarrell-Ash monochromator, the order sorting filters, and the focusing optics. The samples are quite transparent, i.e. exhibit very small light absorption, thus the induced photocurrent is also small. In order to minimize signal noise, the photocurrent was measured by the integration method and, to avoid off set errors introduced by the finite input current of the measuring instrument, a Keithley model 616 electrometer was used as the measuring instrument. The same measuring technique was also used in both the Windowed Thermally Released Charge (WTRC) experiment and the Residual Field Induced Charge (RFIC) measurement. Calibration of the monochromatic light source was done with a Laser Precision Corp. model RK3440 pyroelectric radiometer. The spectra output, after passing through all the necessary optics and the sample substrate up to the first insulator layer, is shown in figure 2.4. The spectra curve was separated into three sections in order to avoid second order interference effects.

Automation of the measuring system was achieved by the use of a Motorola 6800 microprocessor based Heath-Kit single-board micro-computer which communicates with the external instruments via a number of interface networks. The block diagram of the system is shown in figure 7.2.

The slowly varying signals, such as the brightness versus peak driving voltages and the electroluminescent spectra etc., were monitored with a Tektronix 7313 storage oscilloscope and the fast signals, e.g. the electroluminescent light pulses and the driving voltages etc., were measured with a Tektronix 7603, 500 MHZ oscilloscope.

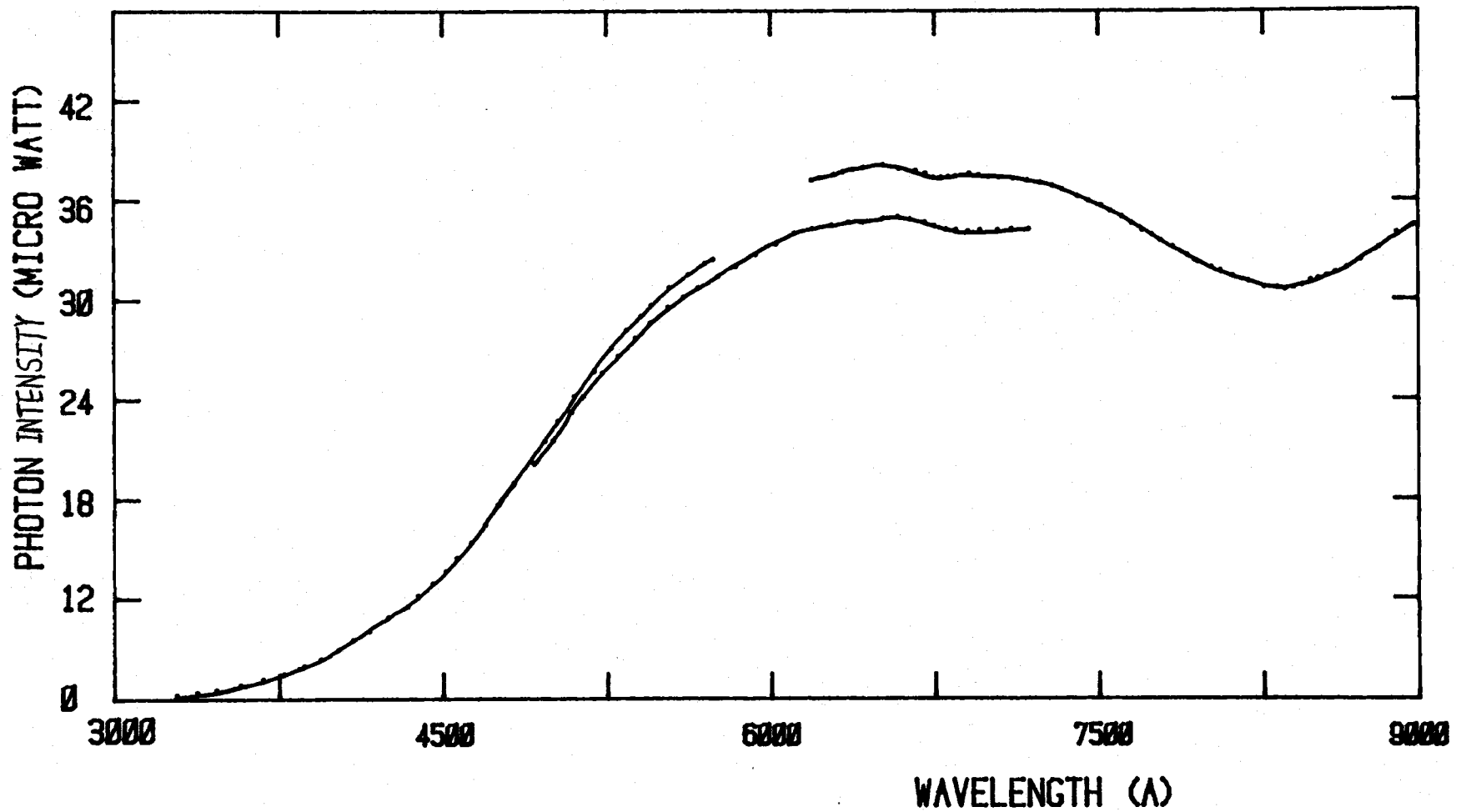


Figure 2.4 The spectra distribution of the light intensity of the monochromatic light source including the necessary focusing and order sorting optics. The segments correspond to three different order sorting filters for each wavelength region.



## THE PHYSICS OF DEVICE OPERATION AND DEVICE CHARACTERISTICS

### 3.1 Light Emission Mechanism

The light emission of a ZnS:Mn ACTFEL device exhibits a nonlinear dependence upon the amplitude of the driving voltage. This nonlinear behavior is associated with the dielectric properties of the ZnS layer. When a driving voltage pulse is applied to the device which establishes an electric field within the ZnS film in excess of  $2 \times 10^6 \text{ V/cm}$ , the ZnS will break down and dissipative conduction currents will flow which increase rapidly with increasing driving voltage amplitude. The electroluminescent emission, which is caused by excitation and radiative de-excitation of the  $\text{Mn}^{+2}$  ion dopant, is seen to be related directly with this dissipative current component [10]. A free  $\text{Mn}^{+2}$  ion, whose electronic configuration is  $1s^2 2s^2 2p^6 3s^2 3p^6 3d^5$ , has a spherically symmetrical ground state  $^6S$  in which all of its five 3d electrons have their spin parallel to each other. In the low lying excited states, one of the five electron spins is flipped over, this electron will be referred to as the "odd" electron later, and gives rise to a series of quartet levels:  $^4G$ ,  $^4P$ ,  $^4D$  and  $^4F$ , in the order of increasing energy. In figure 3.1, a schematic representation of how those five electrons are distributed among the 3d orbitals for each of the above quartet levels is shown. In all the rows of the figure, there are five short horizontal bars, they represent the five 3d orbitals of a manganese ion, each with a specific Z axis projection of the orbital angular

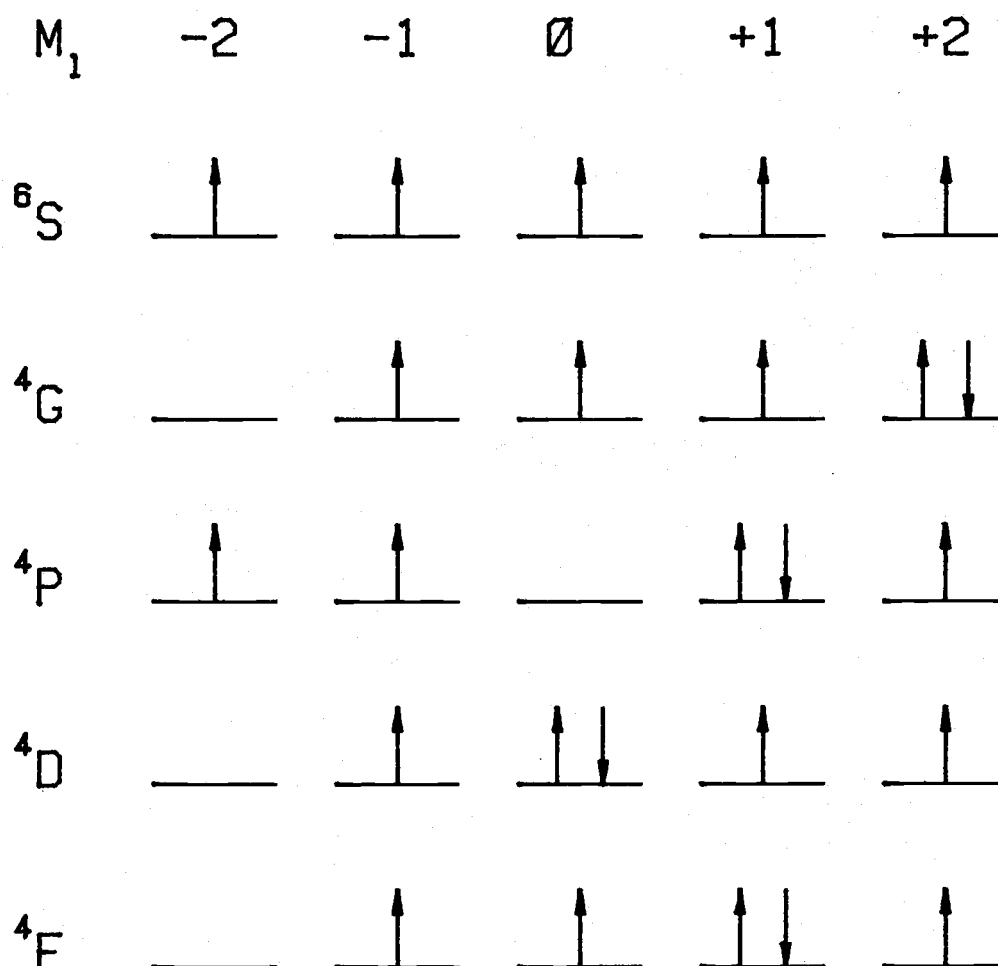


Figure 3.1 Schematic representation of the distribution of the 3d electrons for the low lying excited states and the ground state of a  $Mn^{+2}$  ion. All the levels have a  $3d^5$  configuration. The arrows represent electrons with their spin aligned either up or down.

momentum  $M_\ell$ . The vertical arrows on top of them represent the occupation of electrons in each orbital, the orientation of the arrows signify the spin quantum numbers  $m_s$ , of the residing electrons to be either  $+1/2$  or  $-1/2$ .

The low lying quartet excited states, inside the tetrahedral crystal field of the cubic ZnS host lattice, are further split into more closely spaced states according to the symmetry of the crystal field environment. The symbols representing those new states, following the nomenclature of crystal field theory [11], and their relative energy levels in the cubic crystal lattice, are shown in figure 3.2.

The manganese ion excitation processes involve transitions from the  ${}^6A_1$  ground state, to one of the five excited states [12]:  ${}^4T_1$ ,  ${}^4T_2$ ,  ${}^4A_1+{}^4E$ ,  ${}^4T_1$ , and  ${}^4T_2+{}^4E$ , as are shown in the figure. These excitation transitions have been observed both in the absorption spectrum of ZnS:Mn cubic crystals [13] and in the photoluminescence spectrum of ZnS:Mn thin films [12], [14]. The five absorption maxima occur at wavelengths near 3900Å, 4300Å, 4650Å, 4980Å, and 5350Å respectively [15]. Once an electron is excited into one of these levels, it then rapidly returns to the lowest  ${}^4T_1$  state via multi-phonon processes. The subsequent radiative transition from the  ${}^4T_1$  state to the  ${}^6A_1$  state, which involves the spin reversal of the "odd" electron, is forbidden by the selection rules [13], [16]. In figure 3.2, some of these transition processes are also shown. Two of the selection rules that are violated by these transitions are described as follows [17], [18]:

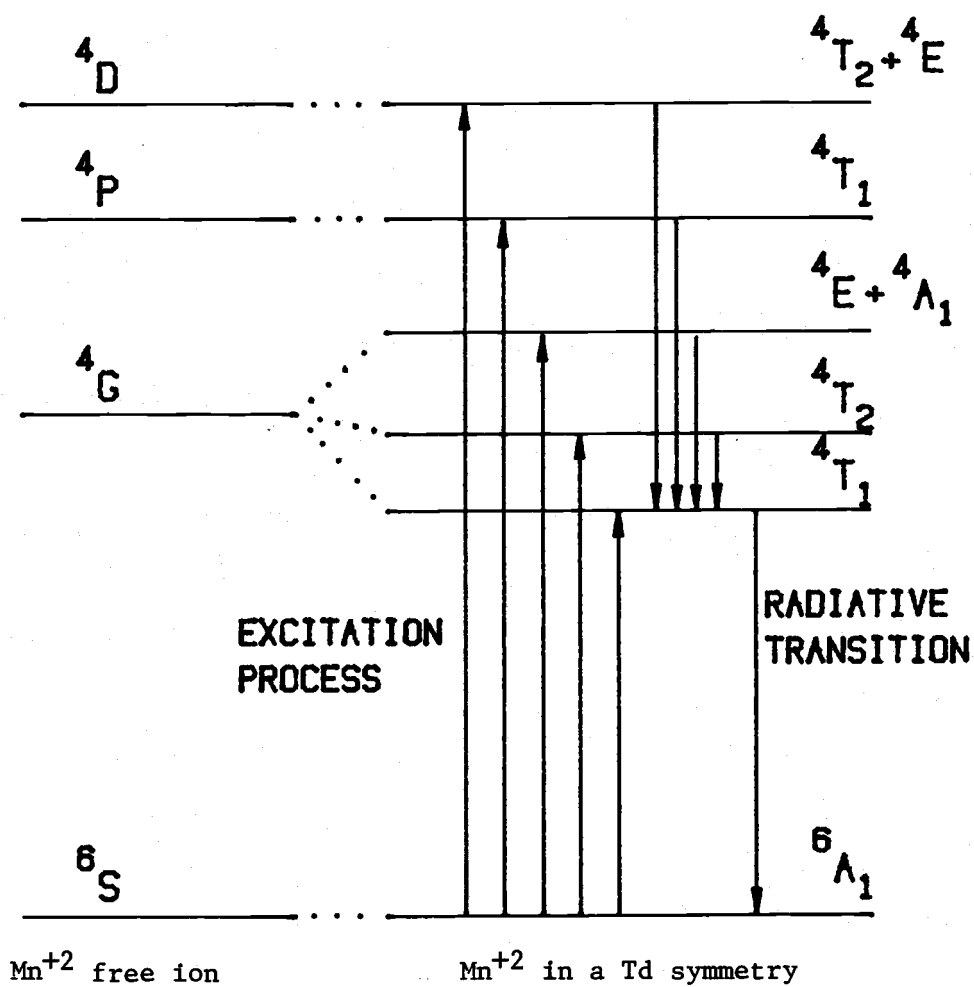


Figure 3.2 Schematic diagram of the  $\text{Mn}^{+2}$  ion energy level in free space (left) and a cubic lattice environment (right). The arrows indicate the excitation and relaxation transitions.

- (i) The only allowed transitions are between configurations where only one electron has its angular momentum quantum number  $\ell$  changed, and this  $\ell$  must change by either +1 or -1 unit in that transition.
- (ii) In the Russell-Saunders coupling scheme, transitions between states of different multiplicities are not allowed.

It is clear that the violation of the first rule is due to the spin flipping processes during transitions between the ground state and the five excited states, where all the transitions are still within the same  $3d^5$  configuration of the  $Mn^{+2}$  ion, therefore, no change of the  $\ell$  quantum number of any of the five electrons takes place. Rule number two is also violated since the spin reversal changes the total spin quantum number from  $5/2$  to  $3/2$  or vice versa, therefore the multiplicity changes between six and four accordingly. However, neither of the above selection rules is strictly rigorous, otherwise the luminescence efficiency of the ZnS:Mn ACTFEL devices (about  $1\sim 4$  lumens per watt) would not be so high. In fact the spin orbital coupling of the  $3d$  electrons has relaxed these rules to some extent [16].

Nonetheless, the transitions are strongly forbidden, which results in a relatively long life time for the  ${}^4T_1$  excited state of the  $Mn^{+2}$  ion, therefore the luminescent decay from this excited state to the  ${}^6A_1$  ground state suffers from competitions with other nonradiative decay channels [19].

The luminescent emission spectrum, which peaks at  $5860\overset{\circ}{A}$  [13], [15], has a very broad half width even at low temperatures. In figure

3.3, the electroluminescence spectra of a sample with 0.78 mole%  $\text{Mn}^{+2}$  doping at two different temperatures are shown. It is seen that the half-width of the emission spectra cover approximately 400Å at 135K and about 560Å at 300K. The origin of this phenomenon is best explained with the configurational model [13], [16]. The configurational coordinate diagram of the  ${}^6\text{A}_1$  ground state and the lowest  ${}^4\text{T}_1$  excited state of a  $\text{Mn}^{+2}$  ion is shown in figure 3.4. The figure indicates that the configurational coordinates of the energy minima of these two states do not coincide with each other. In photo-excitation of a  $\text{Mn}^{+2}$  ion, route number one, the maximum absorption band would occur at the photon energy equals  $E_1$ . Once excited into the upper band, the electron will then move toward the energy minimum of the  ${}^4\text{T}_1$  level via emission of a number of vibrational quanta, i.e., the multiphonon process. The radiative decay which follows route number two shown in the figure, will then emit a photon with the most probable energy given by:

$$h\nu_e = E_1 - nh\nu_T - mh\nu_A \quad (3.1)$$

where  $h\nu_e$  is the emitted photon energy,  $h\nu_T$  is the vibrational quantum of the first excited state  ${}^4\text{T}_1$ ,  $h\nu_A$  is the vibrational quantum of the ground state  ${}^6\text{A}_1$ ,  $n$  is the mean number of emitted phonons after the electron has been excited into the  ${}^4\text{T}_1$  level, and  $m$  is the mean number of emitted phonons after the radiative transition back to the  ${}^6\text{A}_1$  level.

It is clear from equation (3.1) that the emission photon energy is generally smaller than that required to excite the absorption. This phenomenon is known as the Stokes' shift which is quite common in

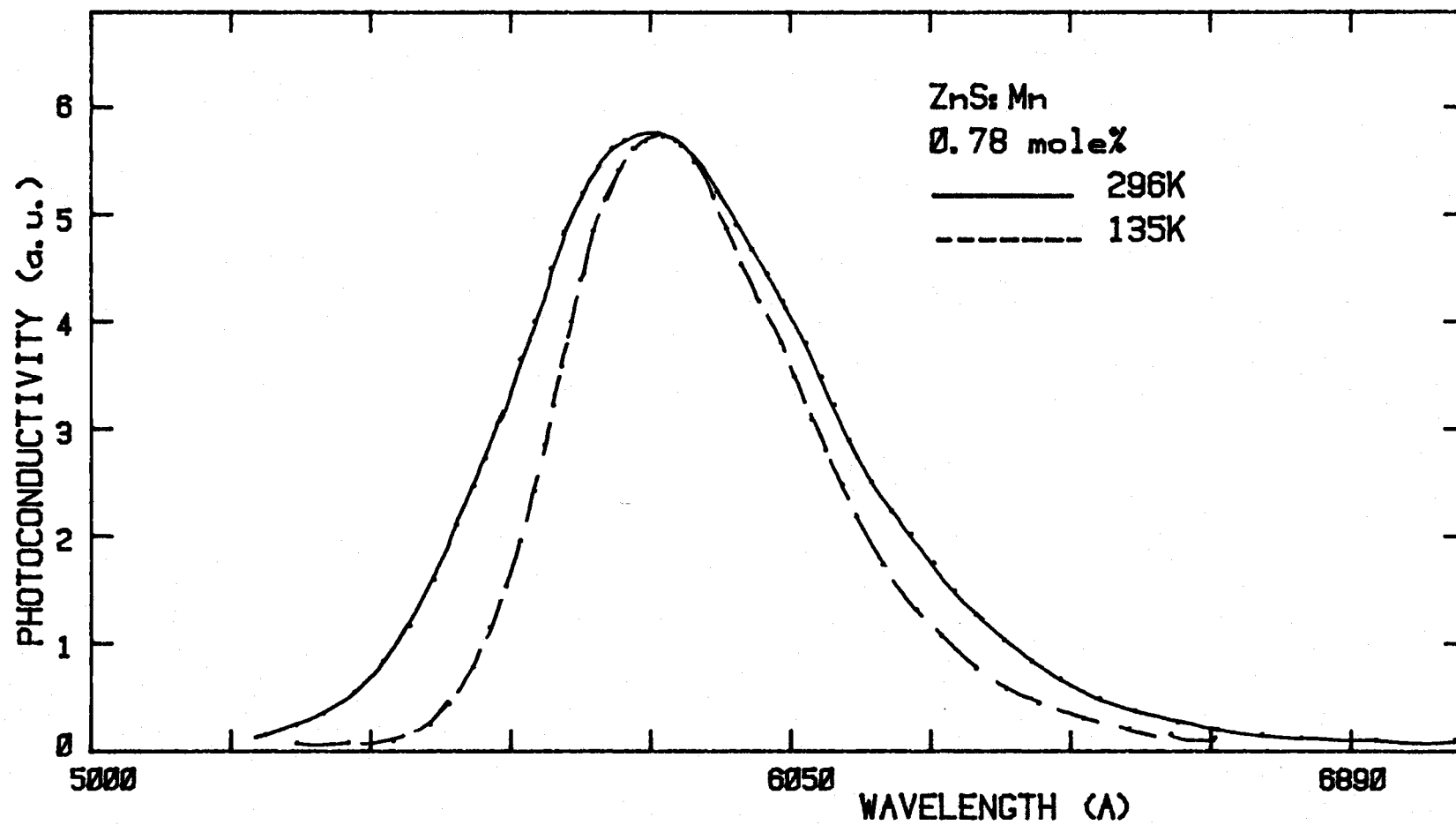


Figure 3.3 The electroluminescent spectra of an ACTFEL device at different temperatures.

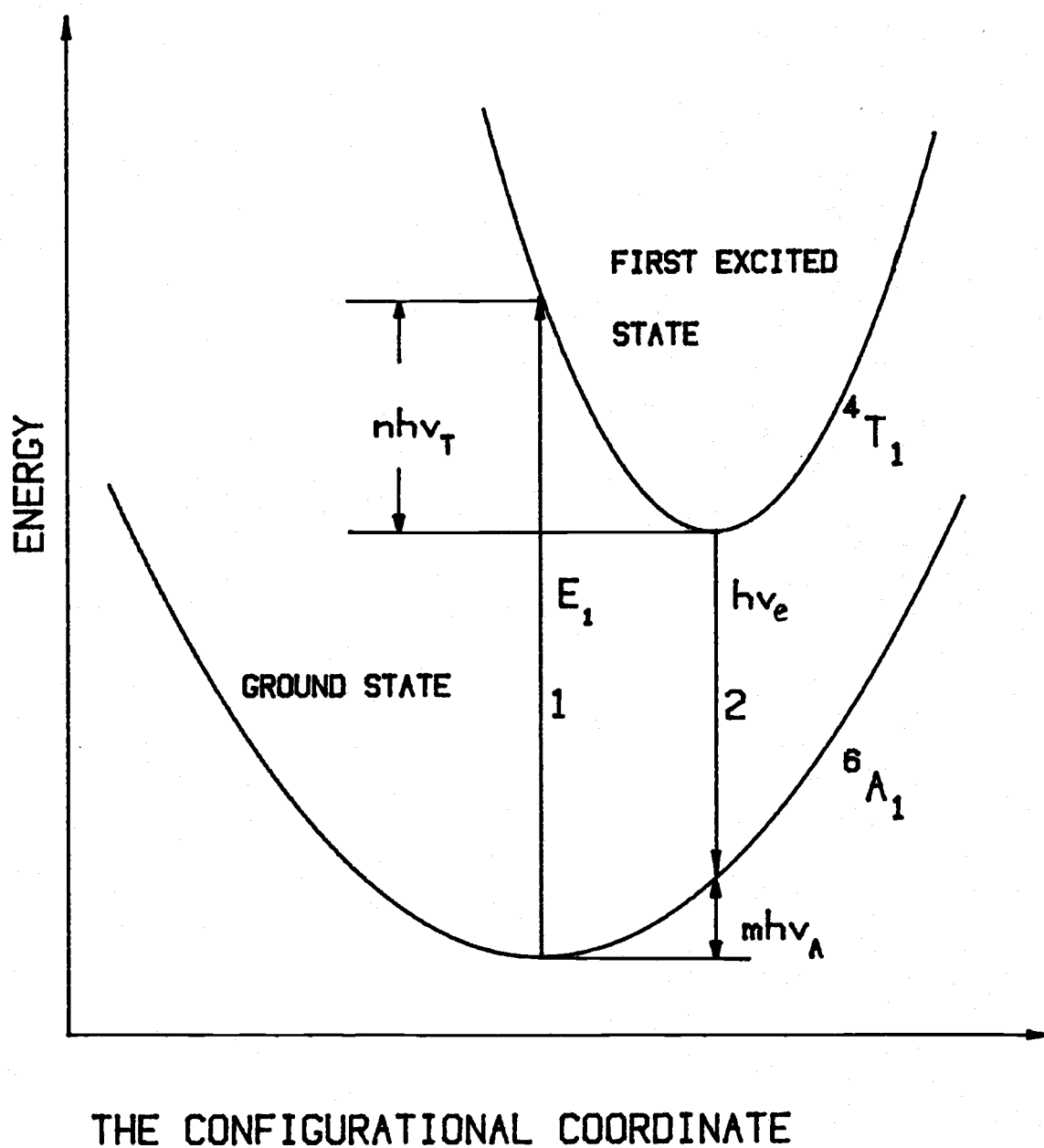


Figure 3.4 Configurational diagram of a  $\text{Mn}^{2+}$  ion in the cubic lattice.  $E_1$  is the energy required for excitation,  $h\nu_e$  is the emitted photon energy, and  $nh\nu_T$  and  $m h\nu_A$  are phonons that are involved in the excitation and the relaxation processes.



the case of deep center luminescence [13]. The Stokes' shift is a very important characteristic of the ACTFEL devices since it implies that the ZnS:Mn film will be transparent to its own emission. Therefore, unlike for the case of p-n junction injection electroluminescence found in LED's, where the luminescent centers have to be engineered to reside as close to the device surface as possible so as to minimize the re-absorption effect, there is no restrictions on either the whereabouts of  $Mn^{+2}$  ions within the ZnS:Mn film, or the upper limit of the film thickness.

The observed emission spectrum of the device is a statistical summation of transitions from different manganese ions, where each of them undertakes a radiative decay from a certain vibrational level  $n$  in the  ${}^4T_1$  state to some other vibrational level  $m$  in the  ${}^6A_1$  state. The probability for the initial state to be such that the electron is at the  $n$ th vibrational level of the  ${}^4T_1$  state,  $Prob^n$ , is proportional to

$$Prob^n \propto \exp(-nh\nu_T/kT) \quad (3.2)$$

where  $k$  is Boltzmann's constant,  $h$  is Plank's constant, and  $T$  is the device temperature in degree Kelvin. The probability that the final state of the transition is at any of the vibrational levels in the  ${}^6A_1$  state is equally probable, and therefore has a value of unity. According to time dependent perturbation theory [20], [21], the probability of radiative transition between the  $n$ th vibrational level of the excited state and the  $m$ th vibrational level in the ground state is given by

$$Prob(n,m) \propto \left| \mu_{eg}^{nm} \right|^2 \quad (3.3)$$

where  $\mu_{eg}^{nm}$  is the matrix element relating the initial and the final states of the transition. The overall electroluminescence spectrum can now be described as [16]:

$$\begin{aligned} I(\nu) &= \sum_{nm} \text{Prob}^n \text{Prob}(n,m) \delta(E_e^n - E_g^m - h\nu) \\ &= \sum_{nm} \exp(-nh\nu_T/kT) \left| \mu_{eg}^{nm} \right|^2 \delta(E_e^n - E_g^m - h\nu) \end{aligned} \quad (3.4)$$

where is a proportional constant,  $\nu$  is the frequency of the emitted photon,  $E_e^n$  and  $E_g^m$  represent the energies of the  $n$ th vibrational level in the excited state and the  $m$ th vibrational level in the ground state respectively,  $\delta$  is the Dirac delta function and  $I(\nu)$  represents the emission spectrum intensity at photon frequency  $\nu$ .

Since there are many vibrational levels within both the excited state and the ground state, equation (3.4) suggests that the emission band will have a broad half-width. At near zero degree absolute temperature, the vibrational levels in the excited state are frozen out except for the zero energy level, i.e.,  $n = 0$ , as is indicated by equation (3.2). However, transitions to any of the ground state vibrational levels is still equally likely to occur, therefore for  $T = 0$  equation (3.4) reduces to

$$I(\nu) = \sum_m \left| \mu_{eg}^{0m} \right|^2 \delta(E_e^0 - E_g^m - h\nu) \quad (3.5)$$

From this equation, it is seen that even at  $T = 0$ , the electroluminescence spectra will have a broad half-width as is suggested in figure 3.3.

### 3.2 The Manganese Ion Excitation Mechanism

The detailed dominant mechanism for excitation of  $\text{Mn}^{+2}$  ions in the ZnS:Mn ACTFEL devices is still controversial [22~24]. The two

prevailing arguments are:

- (i) The direct impact process [25], [26], where the basic features are illustrated in figure 3.5(a): Bound electrons are tunneled out from their trapping centers and accelerated to sufficient kinetic energies under the influence of the biasing high electric field, they then collide with  $\text{Mn}^{+2}$  ions and excite the latter into the excited state.
- (ii) The resonant energy transfer process which is similar to the excitation mechanism in powder electroluminescence [24]. Hot electrons first generate electron-hole pair via collision excitation, as the electron-hole pair recombines, the energy is resonantly transferred to a  $\text{Mn}^{+2}$  ion and thus accomplishes the excitation process.

Recently, Tanaka et al [23] provided major experimental evidence, from time resolved photoluminescence and electroluminescence spectroscopy, to show that the hot electron direct impact on to  $\text{Mn}^{+2}$  ions is the dominant process for manganese excitation. However, other workers have been unable to duplicate their experimental results [27]. Nonetheless, whichever process is the dominant excitation mechanism, hot electron collision is an important process in the operation of ACTFEL devices and is responsible for the generation of a fast-decaying broad luminescent emission band observed in the time resolved electroluminescence spectra analysis [28].

The terminology "hot electrons" used here implies that there is no thermal equilibrium between the electrons and lattice phonons

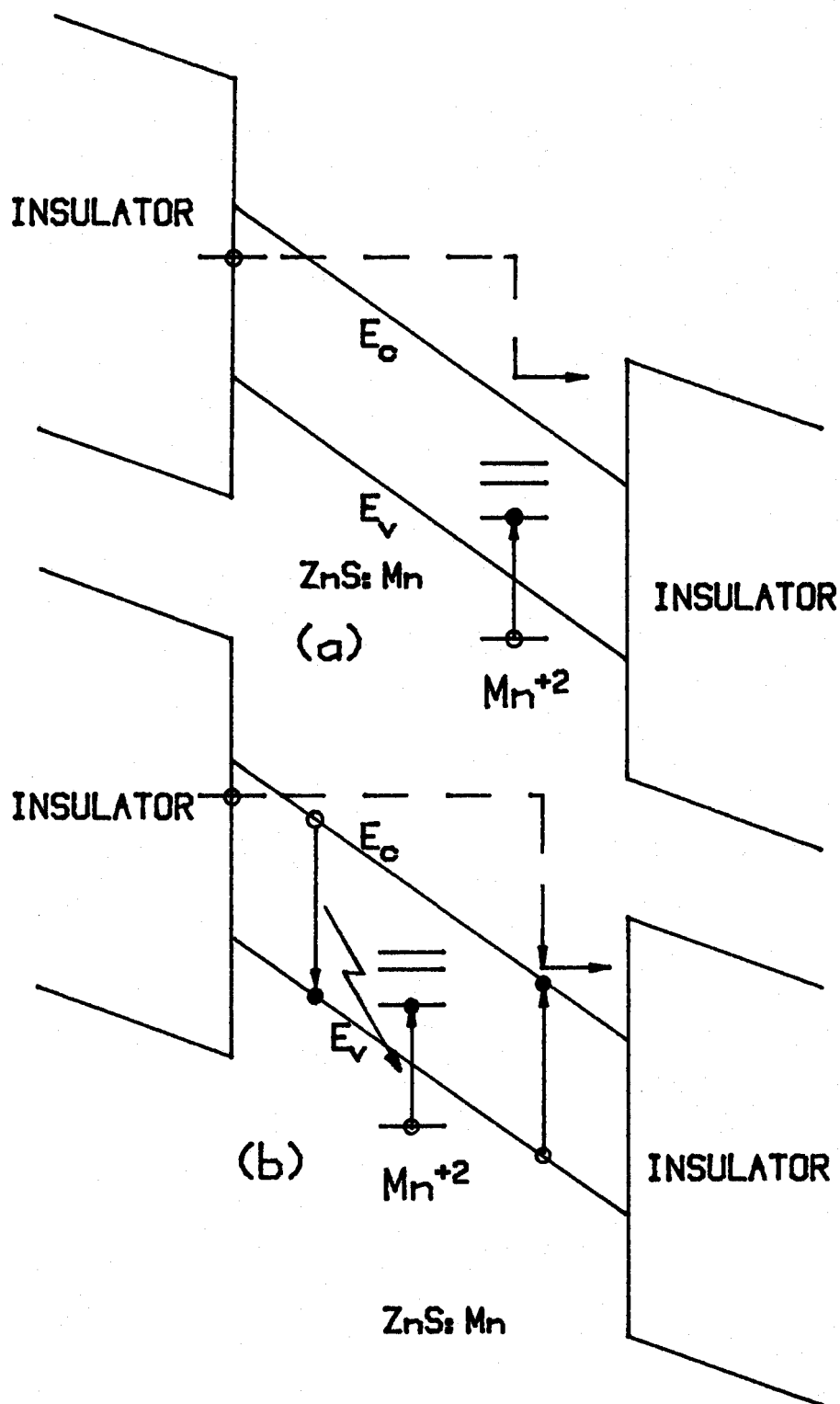


Figure 3.5 Mechanisms for the  $Mn^{+2}$  ion excitation process.  
 (a) the hot electron direct impact excitation process &  
 (b) collision of hot electrons first generate electron pairs,  
 then the energy is transferred to the  $Mn^{+2}$  ion and  
 excites it to the excited state.

[25], i.e., the electrons are running in the ballistic mode and can have a kinetic energy much larger than that would be predicted according to the equal partition principle. In other words, these electrons are characterized by a temperature  $T_C$  which is much greater than the device temperature  $T$ . Based on these observations and the device structure, a simplified equivalent circuit of the device is shown in figure 3.6. The insulating layers are represented by a pair of pure capacitors, since generally these insulators have a very small loss tangent. When the driving voltage is below the threshold level, the ZnS:Mn layer exhibits very little conductance and behaves like a capacitor, as the threshold level is exceeded, ZnS conduction current starts to flow and clamps the resulting electric field to the threshold level  $E_{TH}$ . Thus, the ZnS:Mn layer is represented by a capacitor in parallel with a pair of back to back zener diodes.

From this equivalent circuit it is clear that, before the threshold voltage  $V_{TH}$  is reached, the input voltage distributes itself among the films as

$$V_i = C_Z V_{in} / (C_i + C_Z) \quad (3.6)$$

and

$$V_Z = C_i V_{in} / (C_i + C_Z) \quad (3.7)$$

where  $V_{in}$  is the input voltage amplitude,  $C_i$  is the total insulator capacitance with  $V_i$  as the voltage across them,  $C_Z$  is the ZnS layer capacitance and the voltage across it is  $V_Z$ .

For the input voltage  $V_{in} > V_{TH}$ , ZnS will become conducting and the total amount of conducted charge  $Q_{tot}$  is given by

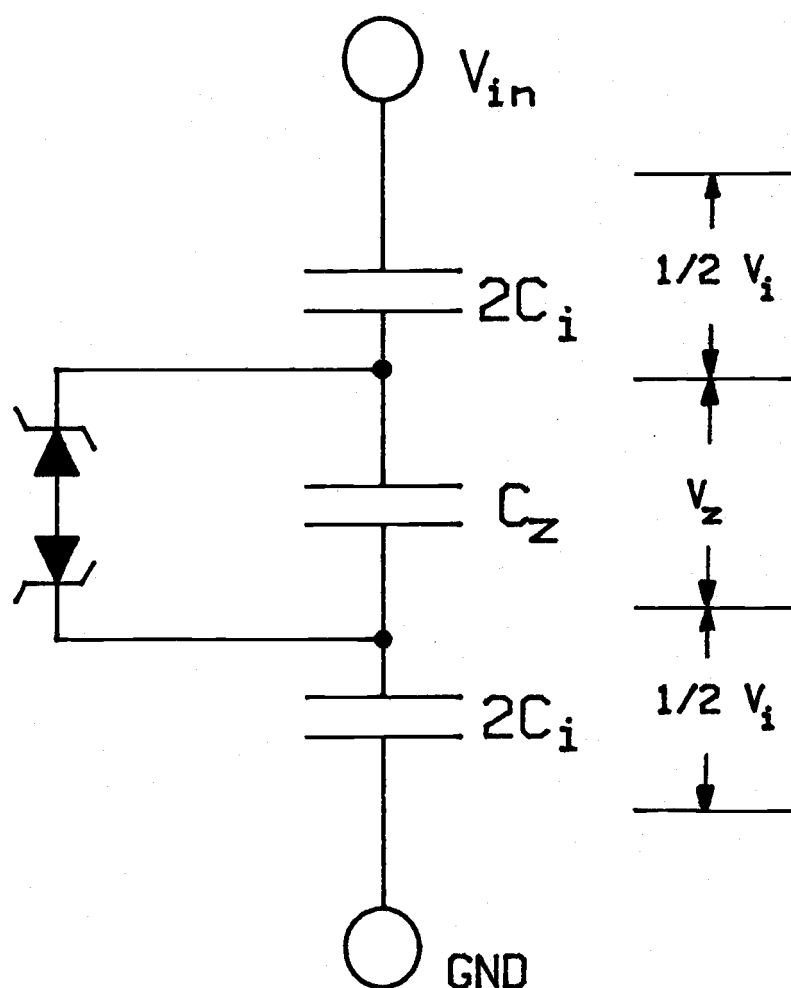


Figure 3.6 An equivalent circuit diagram of the ZnS:Mn ACTFEL device where  $2C_i$  is the capacitance of each insulator layer and  $C_z$  is the ZnS film capacitance. The break down strength of the ZnS layer is  $V$  and is represented by the zener diodes.

$$\begin{aligned}
Q_{tot} &= \int_0^T i_{dissp}(t) dt = \int_0^T i_{tot}(t) dt - Q_{displ} \\
&= 2[(V_{in} - E_{TH} d_z) C_i - C_i C_z V_{in} / (C_i + C_z)] \quad (3.8)
\end{aligned}$$

where  $i_{tot}$  is the total device current,  $i_{dissp}$  is the dissipative current component,  $T$  is the driving voltage pulse width,  $Q_{displ}$  is the displacement charge,  $E_{TH}$  is the ZnS layer break down electric field strength and  $d_z$  is its film thickness.

The factor of 2 in equation (3.8) is due to the polarization phenomenon which will be discussed in the next section. Under steady state conditions, this conducted charge travels back and forth between the two ZnS-insulator interfaces under the excitation voltage. The power input to the ZnS layer can thus be described as

$$\text{Power} = 2fQ_{tot} E_{TH} d_z \quad (3.9)$$

where  $f$  is the frequency of the driving voltage; the factor of 2 is due to the two pulses, of opposite polarity, for each frequency cycle. The expression in this equation is only an approximate since the internal ZnS electric field is not a constant during the conduction cycle. This will be discussed in more detail later, in chapter 8.

### 3.3 The Average Brightness and the Frequency Saturation Phenomenon

Provided that the driving voltage amplitude is not too far above the threshold level, the electroluminescent light output of an ACTFEL device is proportional to the dissipative current component.

In figure 3.7, the timing relationship among the driving voltage pulse, the induced device transient current, and the corresponding light output is shown. It is seen that the electroluminescent emission

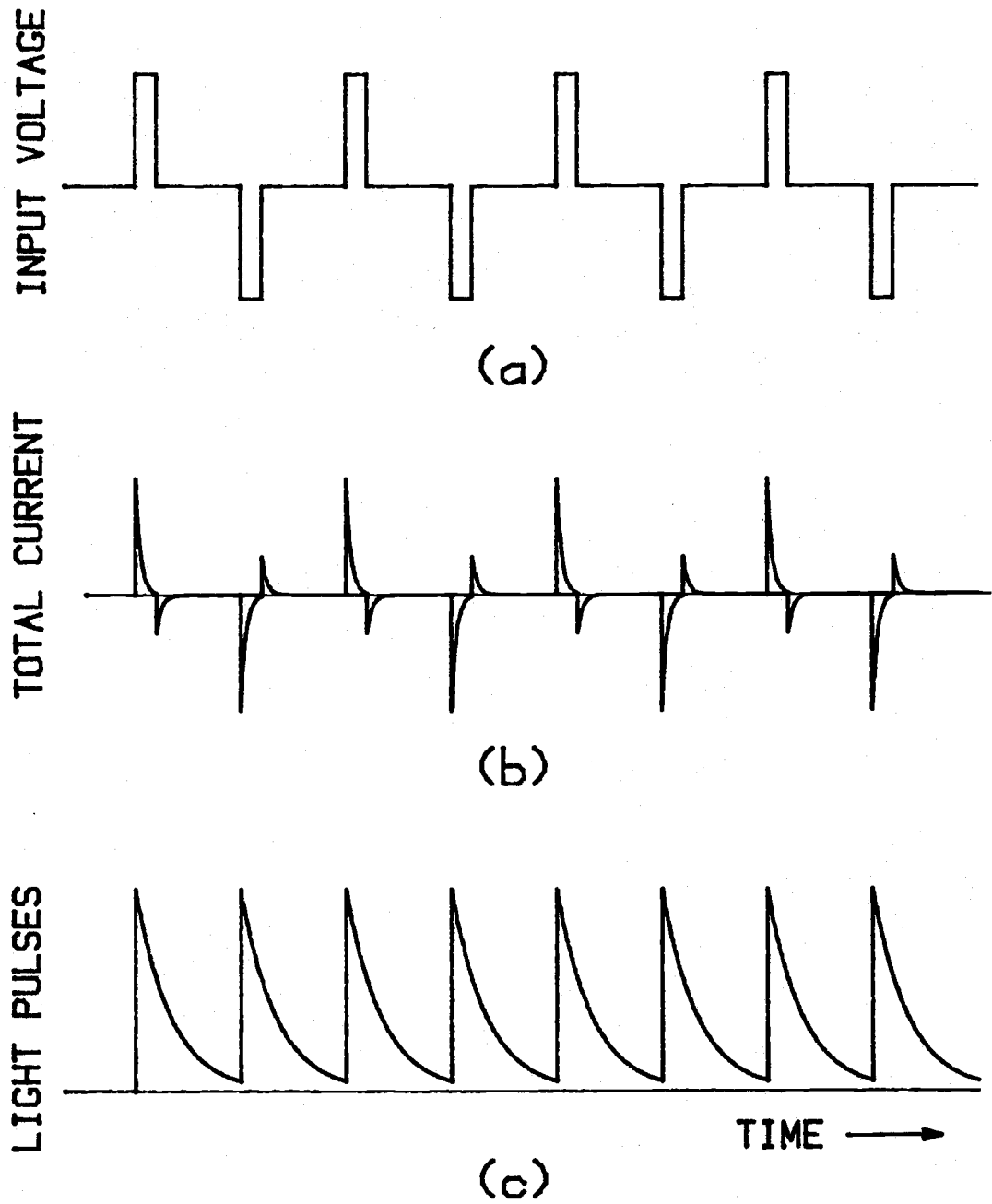


Figure 3.7 The timing diagram of the input driving voltage, the induced total current and the electroluminescence light pulses.



consists of a sequence of light pulses and, depending on the driving voltage frequency and the emission decay time constant, these may or may not overlap each other. At a given temperature, the luminescence decay time is a characteristic quantity of a sample and is determined basically by the  $Mn^{+2}$  concentration.

Due to the persistence of vision of the retina, the average brightness  $B$  as sensed by a human eye, is the time average of the total amount of light intensity received by the eye over a short period, i.e., about one tenth of a second. If the electroluminescence decay of the ACTFEL devices after an excitation voltage follows a simple exponential relationship, i.e.

$$L(t) = L(0)\exp(-t/\tau) \quad (3.10)$$

where  $L(0)$  is the initial amplitude of the light pulse and  $\tau$  is the luminescence decay time, the average brightness will then be given by

$$B = (1/t_0) \int_0^{t_0} L(t) dt \quad (3.11)$$

where  $t_0 \approx 0.1$  second.

Under repetitive driving condition, equation (3.11) will remain unchanged if the average is taken over just one period, provided it is not longer than  $t_0$ , thus

$$\begin{aligned} B &= (1/t_p) \int_0^t L(t) dt \\ &= (1/t_p) L(0) \tau [1 - \exp(-t_p/\tau)] \end{aligned} \quad (3.12)$$

where  $t_p$  is the time between light pulses.

At low frequencies where  $t_p \gg \tau$ , equation (3.12) converges toward  $L(0)/t_p$  and the brightness is linearly proportional to the driving frequency, or  $1/t_p$ . As the frequency becomes very high such that

there is significant overlap between light pulses, frequency saturation phenomenon occurs [24], [29], and the brightness assumes a sublinear dependence on the driving voltage frequency. In figure 3.8, this frequency saturation phenomenon for a sample with a 1.38 mole% manganese concentration is shown.

Some physical processes that may have been responsible for this are discussed in the following:

- (i) It is clear now that the only radiative decay which gives the yellowish luminescence, is due to the electronic transition within a  $\text{Mn}^{+2}$  ion from the lowest lying  ${}^4\text{T}_1$  excited state to the  ${}^6\text{A}_1$  ground state. Transitions between the  ${}^4\text{T}_1$  level and other higher levels do not generate the observed electroluminescence. However, it is possible for electrons within the  ${}^4\text{T}_1$  level, to be excited into still higher lying levels by the impact of hot electrons. This process, which is normally radiationless, does dissipate some of the input energy, and convert it into the form of heat. Moreover, the electron scattering cross section for excitation of the  ${}^4\text{T}_1$  level may have been larger than that for excitation of the  ${}^6\text{A}_1$  ground state, because of the geometric difference between the two. The combined effects of the above leads to the frequency saturation phenomenon.
- (ii) Due to the filamentary conduction phenomenon associated with these ACTFEL devices [30], [31], the ZnS dissipative current is confined to filaments having a very small cross section. The small effective volume of these

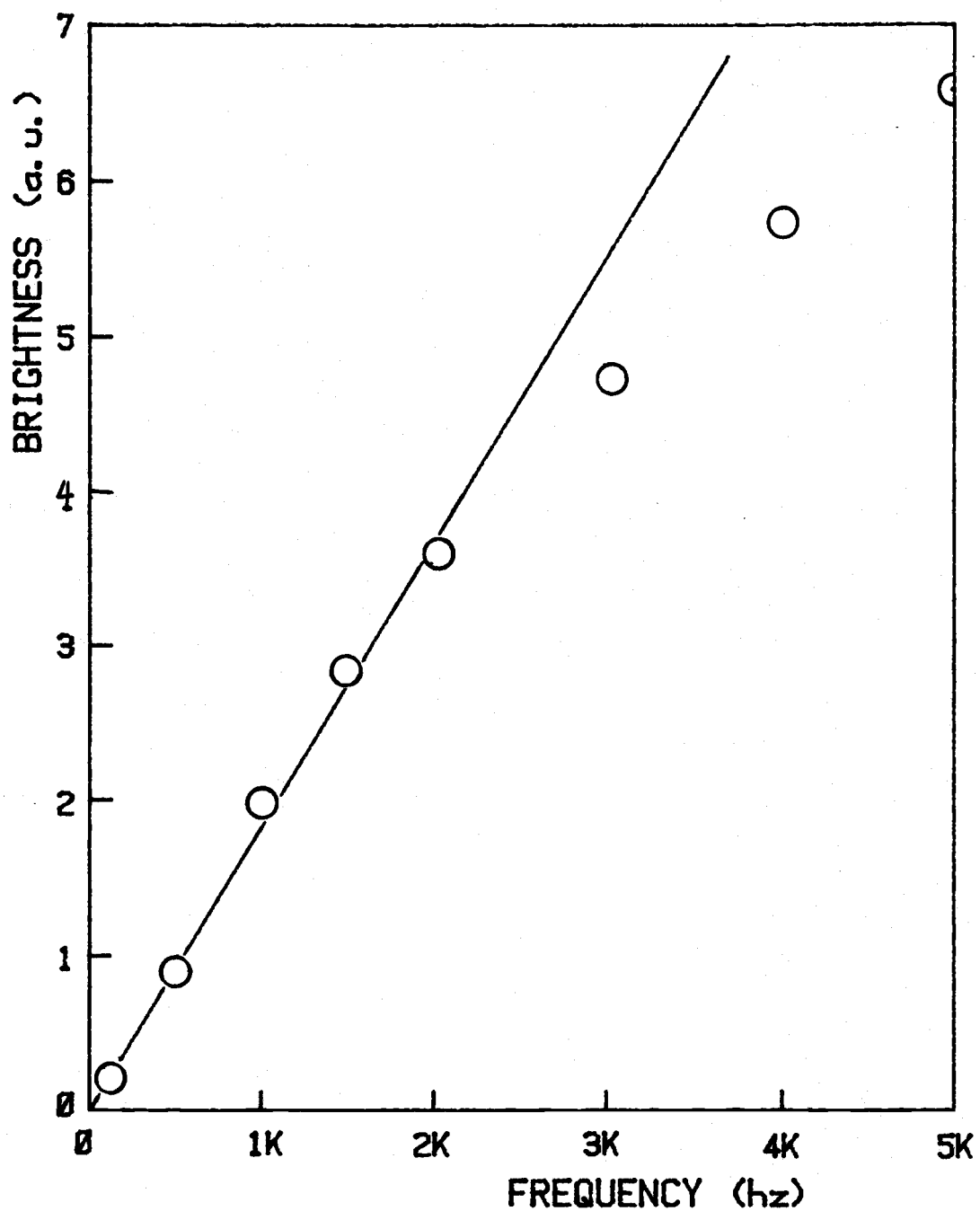


Figure 3.8 Plot of the average brightness versus driving frequency. Notice the sublinear dependence of brightness at high frequencies.

filaments may result in an actual saturation of the available luminescence centers at high driving frequencies.

- (iii) When the hot electrons are flowing within the active layer to excite  $\text{Mn}^{+2}$  ions, they also collide with the ZnS host lattice and generate heat, in addition to the process discussed in paragraph 1 above. Although the glass substrate can serve as a heat sink, due to the finite thermal conductivities of the ZnS film and the glass substrate, the actual ZnS temperature is determined by the heat generation rate, as well as the effective thermal conductivity, i.e.

$$\Delta T = 2fG/\sigma_T \quad (3.13)$$

where  $\Delta T$  is the ZnS film temperature in excess of that of the ambient,  $G$  is the heat generated under each excitation pulse,  $\sigma_T$  is the overall thermal conductivity from the ZnS film to the ambient, and  $f$  is the driving voltage frequency.

It is clear from equation (3.13) that the temperature of the ZnS film increases as the driving frequency increases. The increased ZnS temperature initiates some nonradiative decay channels for the  $\text{Mn}^{+2}$  ions to dissipate their excitation energy and results in a poorer luminescence efficiency. This temperature effect forms the most probable mechanism for the frequency saturation phenomenon and will be discussed in chapter five later.

### 3.4 The Brightness vs. Driving Voltage Curves (B-V curves), And The Hysteresis Behavior

From the device model shown in figure 3.6, it is seen that those back to back zener diodes will cause the dissipative conduction process to exhibit threshold characteristics. Since the electro-luminescent emission is roughly proportional to the dissipative current, it is anticipated that similar threshold behavior will also be observed for the light emission process. In figure 3.9, a plot of the luminescence brightness against the driving voltage amplitude, the B-V curve, for a certain sample is shown. The figure indicates that the average brightness is essentially zero for small driving voltages until point A where the brightness increases sharply with increasing driving voltage amplitude. The voltage corresponding to point A is the threshold voltage, and the region beyond point S where the brightness enhancement slows is called the saturation region. Because of the peculiar shape of the B-V curve, when comparing the luminescent brightness of different samples, it is difficult to determine which driving voltages are to be used. The difficulty comes from, (i) the threshold voltage usually varies from sample to sample, and (ii) the steepness of the B-V curve between A and S also exhibits large variations. Nevertheless, to facilitate later discussion, a saturation brightness is defined to be the brightness of the device when the driving voltage amplitude is 10 percent above its threshold level.

The saturation brightness of an ACTFEL device decreases as its manganese concentration increases and another interesting phenomenon

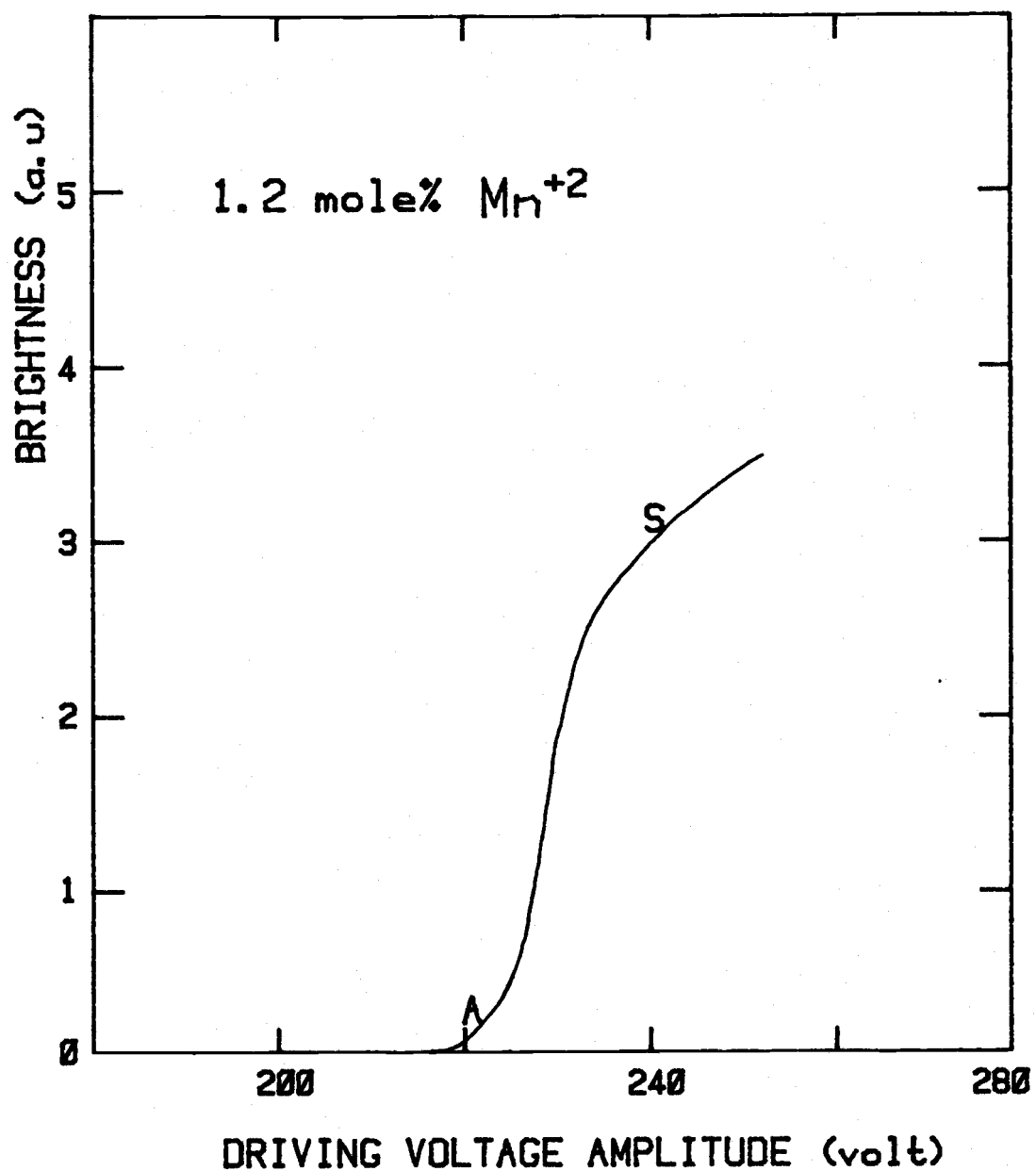


Figure 3.9 The B-V curve of a sample with 0.8mole% Mn doping where A correspond to the threshold level and S is the saturation level.

occurs. This phenomenon is known as the hysteresis behavior [32-34], and is illustrated with the B-V curve of a high  $Mn^{+2}$  doping sample shown in figure 3.10(a). The luminescence will not be turned on until the voltage is increased beyond the threshold level  $V_{TH}$ . Once the light emission has been triggered on, it will remain in the on state with a reduction of the driving voltage, until the extinction level  $V_E$  is approached, further decrease of the driving voltage to below  $V_E$  will switch the device to its off state. By bringing the driving voltage to different levels above  $V_{TH}$ , different stable brightness can be obtained, this effect is illustrated in the figure by the various pathes of the B-V curve and are identified by the arrows. The multi-stable property of the device brightness when sustained within its hysteresis regime, provides an image storage system having virtually unlimited number of grey scales. The physical phenonema responsible for this effect is that of filamentary conduction processes within these ACTFEL devices.

Bistable columnar conduction filaments, having a diameter of  $\leq 0.8 \mu m$  and a B-V curve similar to that as shown in figure 3.10(b), have been observed within the ZnS layer of a hysteretic sample [30], [31]. The threshold and extinction voltages of these filaments are statistically distributed and therefore they can be triggered on and off independent of each other, at different driving voltage amplitudes.

Owing to the small size of each conduction filament and the finite optical resolution power of a human eye, when a sample is sustained within its hysteresis regime, the brightness of the sample

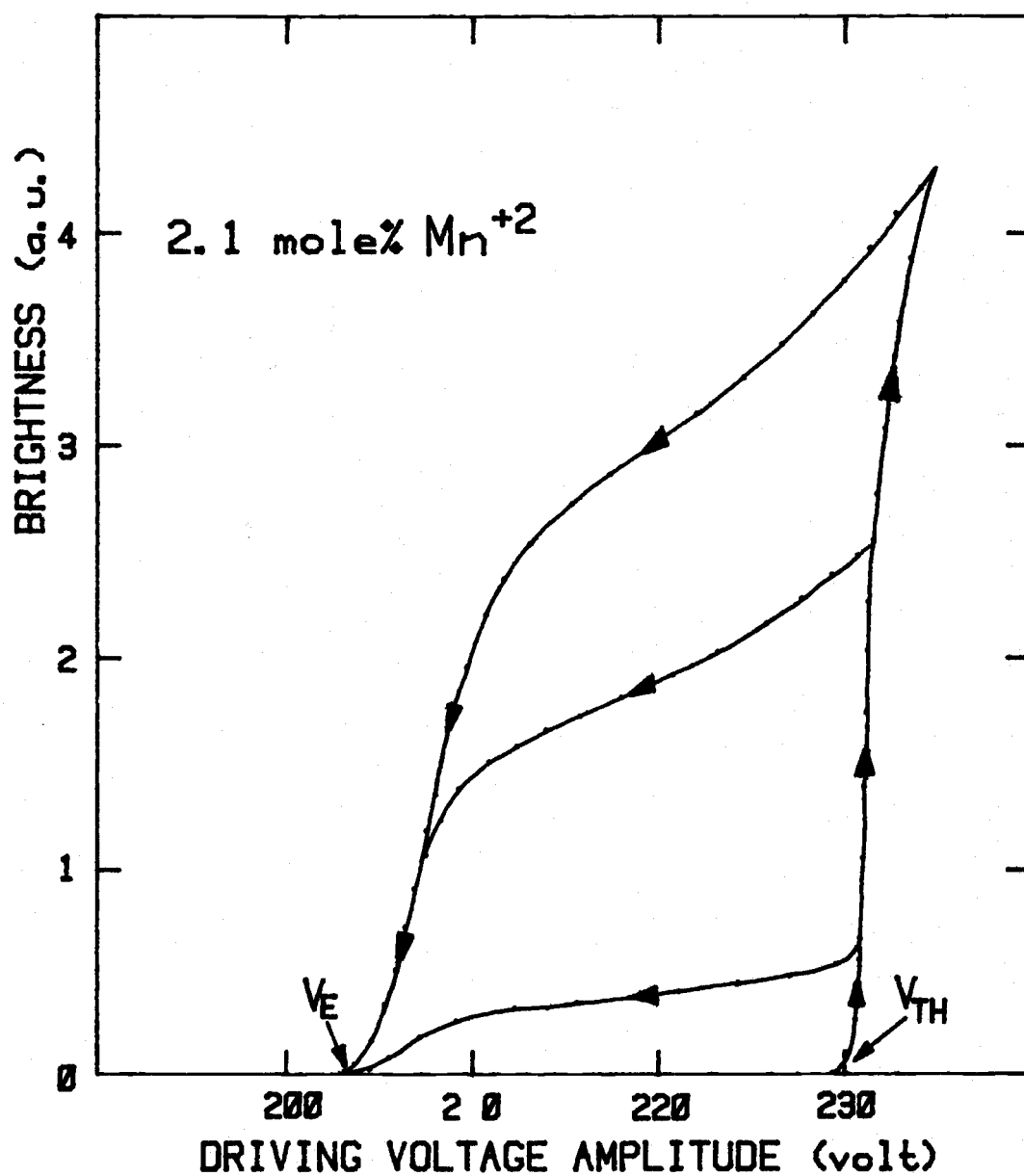


Figure 3.10 The B-V curve of a high  $Mn^{+2}$  doping sample showing the hysteresis behavior. The curves are traced out by slowly sweeping the amplitude of the driving voltage back and forth from below  $V_E$  and various levels above  $V_{TH}$ .



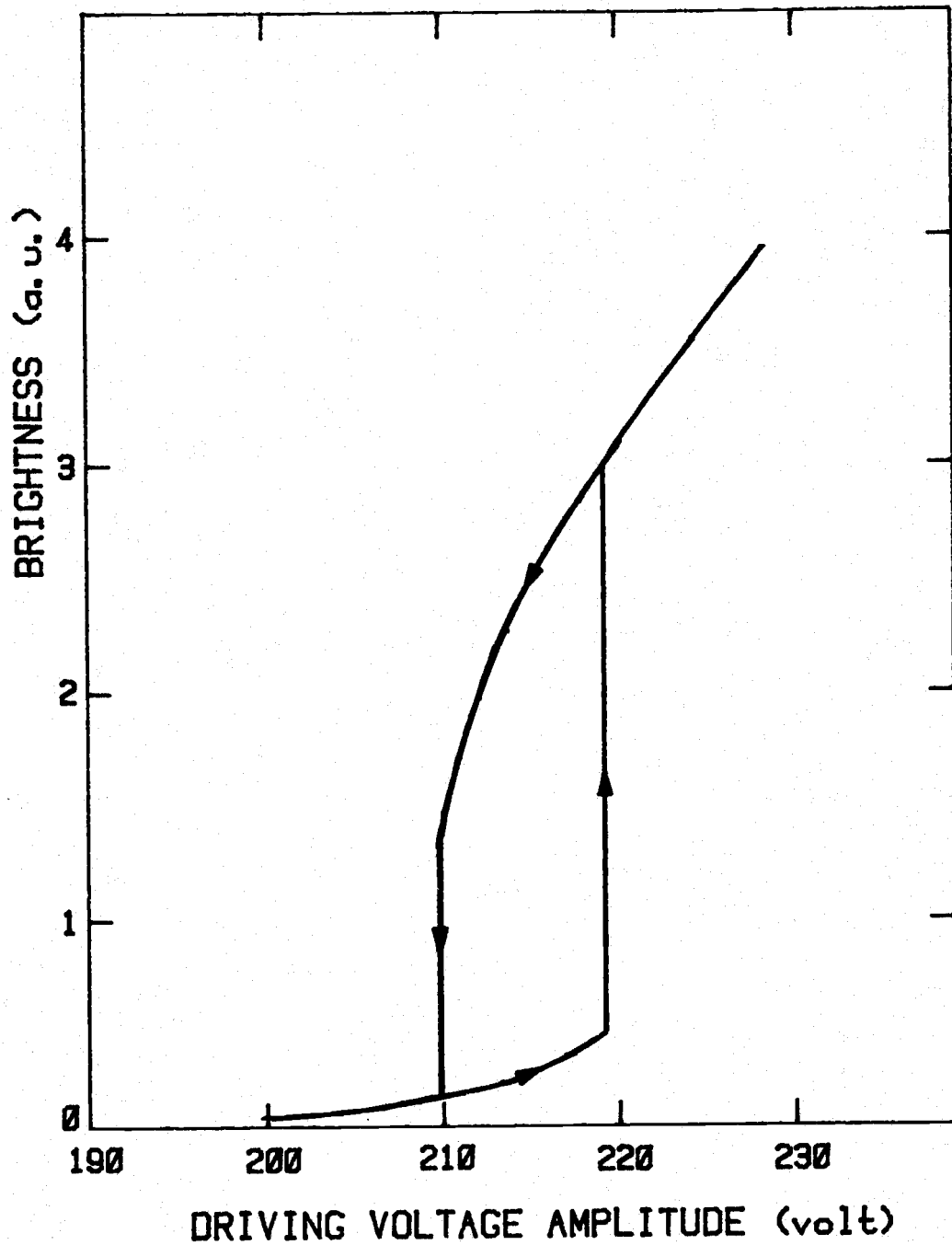


Figure 3.10.(b) The B-V curve of each individual conduction filament associated with the hysteretic ACTFEL devices. [after reference 30]

is "seen" to vary continuously from the highest to the lowest level according to the density of the conduction filaments in their on states, which leads to the observed brightness multi-stability as shown in figure 3.10(a). For each conduction filament, the luminescent brightness in its off state is not zero and is slowly increasing with the driving voltage amplitude. A similar result is seen for the area outside the filaments. This uniform background luminescence is most likely caused by the conduction current generated from the phonon-assisted tunneling processes [36].

Because the filamentary conduction process induces a negative resistance effect, the equivalent circuit for the hysteretic samples is therefore modified to incorporate this phenomenon and is shown in figure 3.10(c).

For the situation with the sample in its on state, whilst the driving voltage is sustained within the hysteretic regime, or the memory regime i.e.,  $V_E < V_S < V_{TH}$ , a "momentary" removal of the sustaining voltage will not affect the device operation after the voltage is re-applied. The term "momentary" here means a few minutes if the sample is exposed under room light, and several hours if it is kept in the dark. The holding time can be increased if the device temperature is lowered. However, if the amplitude of several consecutive sustain pulses is suddenly reduced from  $V_S$  to just below the extinction level  $V_E$ , the sample will then quickly return to the off state even if no other changes of the sustaining voltage are made. The effectiveness of those erasing pulses is strongly dependent upon their amplitude. This is illustrated in figure 3.11 with the plot

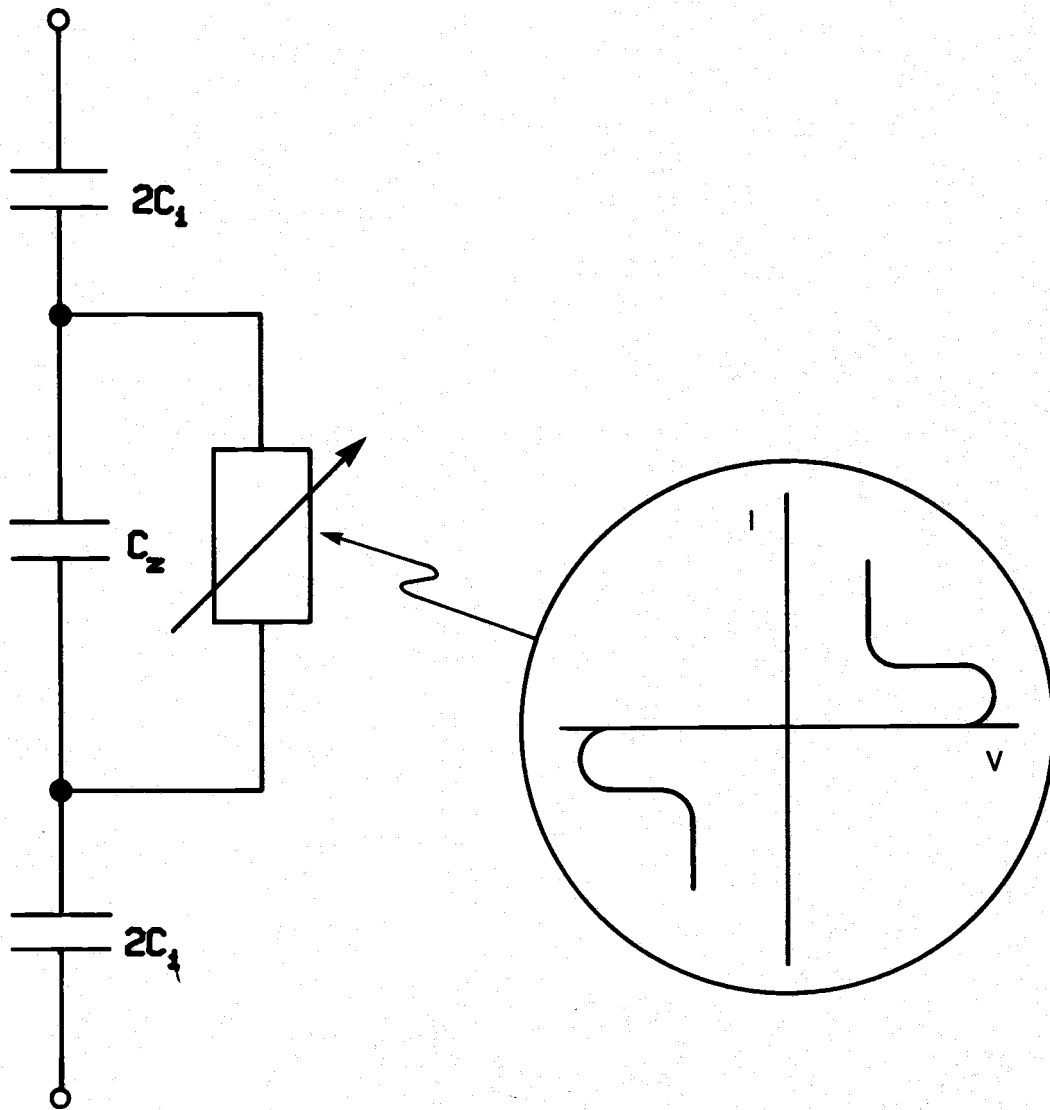


Figure 3.10.(c) The equivalent circuit for the samples having hysteresis characteristics. Notice the negative resistance behavior of the ZnS film.

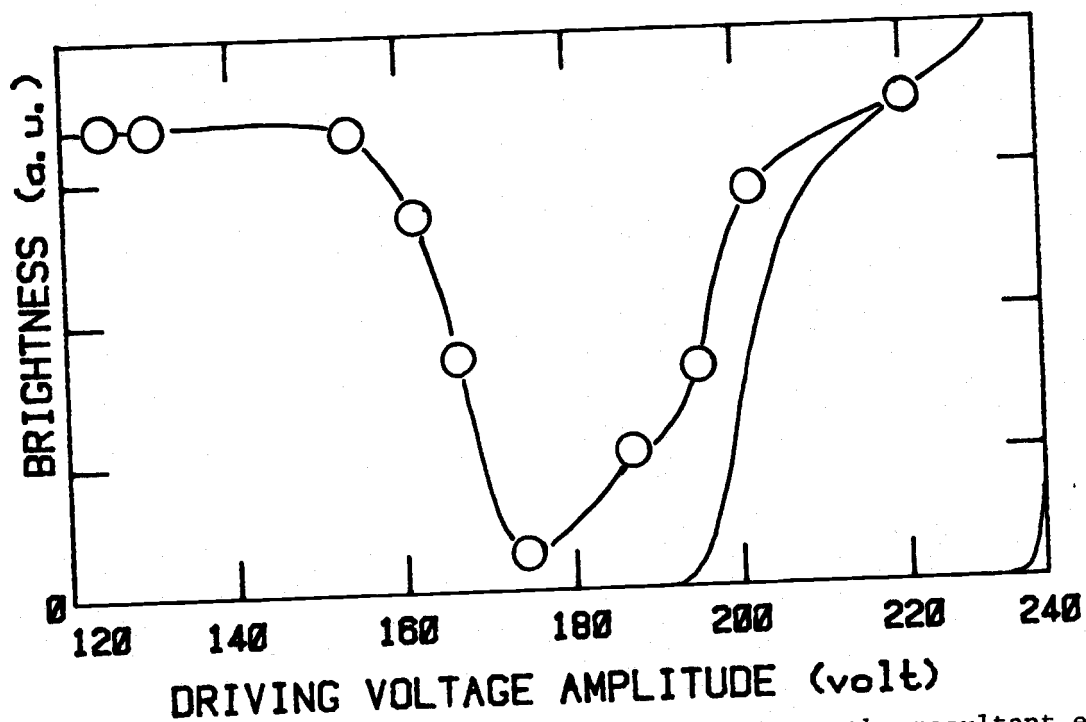


Figure 3.11 Effectiveness of the erasing pulses on the resultant electroluminescence intensity as a function of their amplitudes. The figure also shows the location of the hysteresis loop for comparison. The sustaining voltage was held at  $V_s$ .

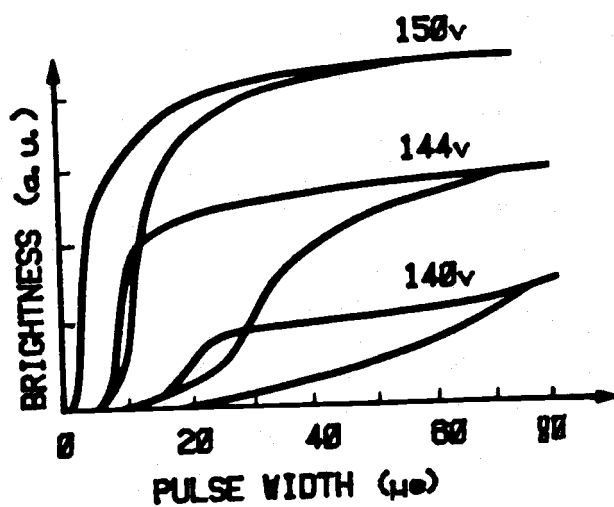


Figure 3.12 The hysteresis of driving pulse width effect.

of the resultant sample brightness after the application of four erasing pulses, as a function of the erasing pulse amplitude. It is seen that the effectiveness of the erasing pulses goes through a maximum and falls off with either increasing or decreasing of the erasing pulse amplitude.

In addition to this memory effect in the driving voltage amplitude, a similar effect is found with changes in the pulse-width of the driving voltage. This new hysteresis in pulse-width effect is very sensitive to the choice of the sustain voltage amplitude. In figure 3.12, the brightness versus driving pulse-width, for three different choices of voltage amplitude, is shown. It is seen that both the hysteresis width and the device on-off contrast ratio changes with variations in the voltage amplitude.

The physical processes responsible for the above phenomena were found in studying the polarization characteristics associated with the ZnS:Mn ACTFEL devices, and they will be discussed in the next section.

### 3.5 The Polarization Phenomenon

If an ACTFEL device in its off state is addressed with a sequence of alternating polarity narrow pulses, whose amplitude is fixed at a level in excess of the threshold voltage, the device will start to emit light pulses, whose intensity increases until a steady state is reached. Depending on the amplitude of the driving voltage, this steady-state may have required hundreds to thousands of driving pulses before it is reached. Another interesting case is that the

amount of light output induced by a driving pulse, is strongly dependent on the polarity of the previous one, the light output is high if the polarity is of the opposite sign, and is low if it is of the same sign. These phenomena are summarized in figure 3.13.

The physical process giving rise to this is known as the polarization effect, which is closely related to the conducted charge within the ZnS layer. In order to have a better understanding of the polarization effect, it is necessary to monitor how the conduction current within the ZnS layer flows when driven by the excitation voltage pulses.

The monitoring of the conducted charge was achieved by using the sensing capacitor technique [8], [9], with a low leakage capacitor connected in series with the electroluminescent device. The capacitance of the sensing capacitor was chosen to be several orders larger than the capacitance of the ACTFEL device, so that almost all of the applied voltages will appear across the device under investigation. This sensing capacitor will then integrate the overall device current, without affecting the amplitude of the driving voltage across it. In figure 3.14 a schematic diagram illustrating this arrangement is shown. For driving voltages below the threshold level, the device current contains only the displacement part and the wave form across the sensing capacitor simply follows that of the driving voltage. When the driving voltage becomes sufficiently large so as to cause the ZnS to break down, electrons will tunnel out from their trapping centers and accelerate along the biasing electric field. These electrons will collide

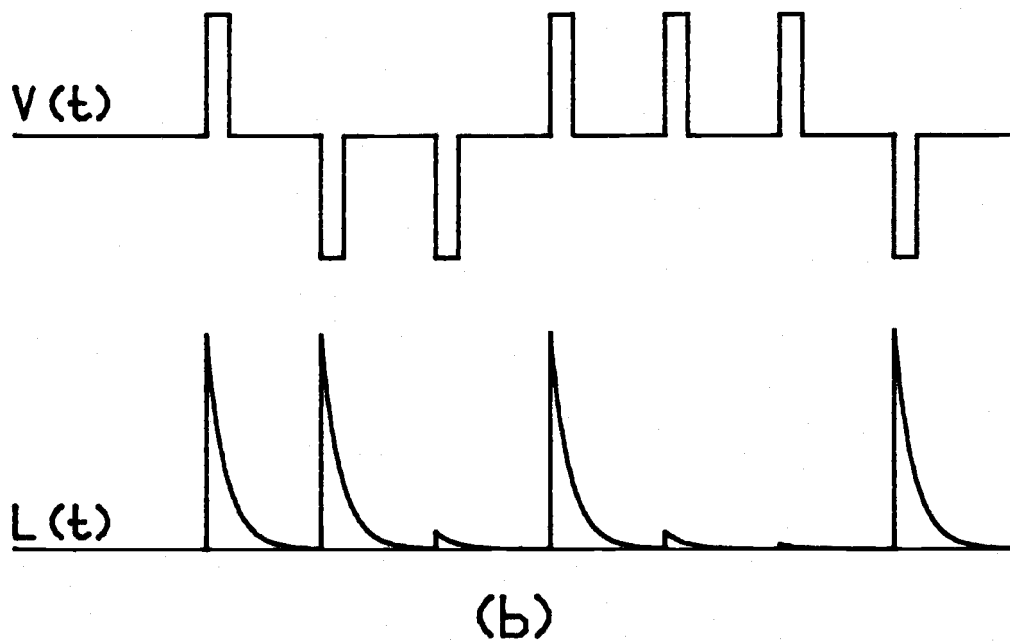
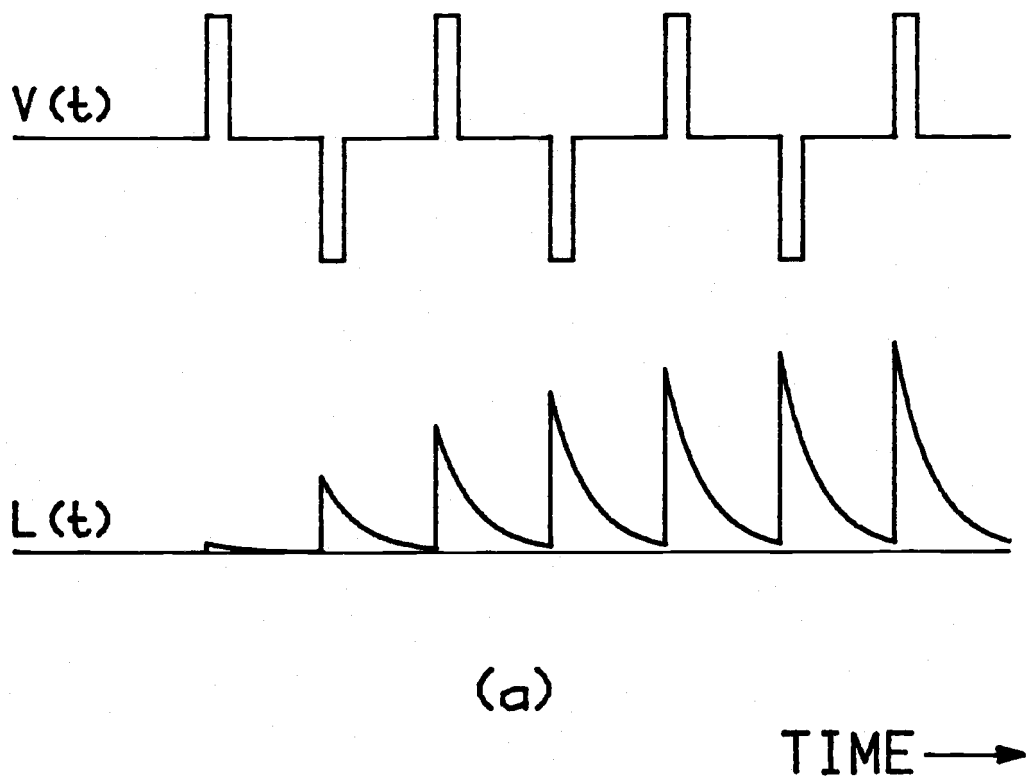


Figure 3.13 (a) The increase of light output under constant driving voltage amplitude. (b) The effect of different polarities of the previous driving pulse on the amplitude of light emitted.

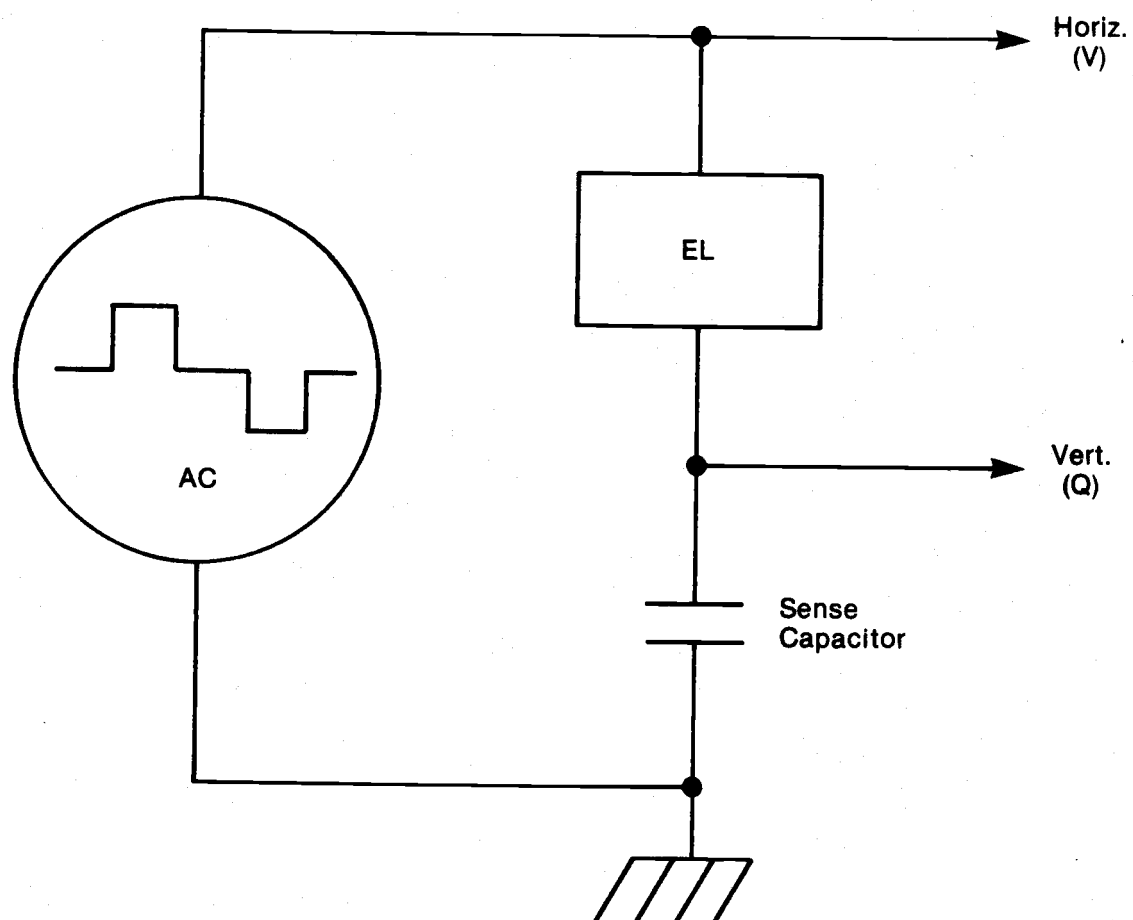


Figure 3.14 The Sawyer and Tower circuit for measuring the polarization effect of the ACTFEL devices.



with the ZnS crystal lattice and the  $Mn^{+2}$  ions to generate electron hole pairs, as well as causing electroluminescence through out their path through the ZnS layer, until they reach the ZnS-insulator interface, which prevents further flow. The electrons are then trapped there at the interface states and build up a polarization field which discourages further flow of the ZnS conduction current. The trapped electrons will remain at their trapping centers until the next driving pulse of the opposite polarity is applied. This trapped conduction charge is reflected as a residual voltage across the sensing capacitor after the driving voltage has returned to zero. This is known as the polarization phenomenon.

Under steady state conductions, the same amount of electrons are traveling back and forth between the ZnS-insulator interfaces. These electrons give rise to a polarization which is denoted by the symbol P. The polarization is measured by taking the difference between residual voltages across the sensing capacitor just before, and just after an excitation pulse, with a boxcar signal averager. The relationship between polarization and the charge measured from the sensing capacitor is derived as follows:

Refer back to figure 3.14 where the schematic diagram of how the polarization was measured is shown. When the polarization charge travels from one interface to the other, it will induce a redistribution of the voltage drop across the ZnS and the insulator layers. Since the conduction of polarization charge occurs mainly on the leading edge of the driving voltage, during the re-distribution of film voltages, the biasing voltage will be at a constant level, i.e.

$$V_i + V_Z + V_C = V_B = \text{constant} \quad (3.14)$$

where  $V_B$  is the driving voltage amplitude,  $V_Z$  is the voltage across the ZnS layer,  $V_i$  is the sum of the voltages across each insulator films, and  $V_C$  is the sensing capacitor voltage.

For the case where  $C_S \gg C_i + C_Z$ , as it is chosen to be so, equation (3.14) reduces to

$$V_i + V_Z = V_B \quad (3.15)$$

thus

$$\Delta V_i + \Delta V_Z = \Delta V_B = 0 \quad (3.16)$$

From the continuity equation, the polarization charge induced voltage re-distribution satisfies

$$C_Z \Delta V_Z = -P/d_Z + \Delta Q_{ZD} \quad (3.17.1)$$

$$C_i \Delta V_i = P/d_Z + \Delta Q_{ZD} = \Delta Q_i \quad (3.17.2)$$

$$C_S \Delta V_C = \Delta Q_i \quad (3.17.3)$$

where  $C_S$  is the capacitance of the sensing capacitor,  $\Delta Q_{ZD}$  is the ZnS displacement current induced by  $P$ , and  $\Delta Q_i$  is the externally observed conducted charge, and  $d_Z$  is the ZnS film thickness.

From equations (17), one has:

$$C_i (P' - \Delta Q_{ZD}) = C_Z (P' + \Delta Q_{ZD}) \quad (3.18.1)$$

$$\Delta Q_{ZD} = P' (C_i - C_Z) / (C_i + C_Z) \quad (3.18.2)$$

$$\begin{aligned} \Delta Q_i &= C_S \Delta V_C = P' + \Delta Q_{ZD} \\ &= 2C_i P' / (C_i + C_Z) \end{aligned} \quad (3.18.3)$$

where  $P' = P/d_Z$

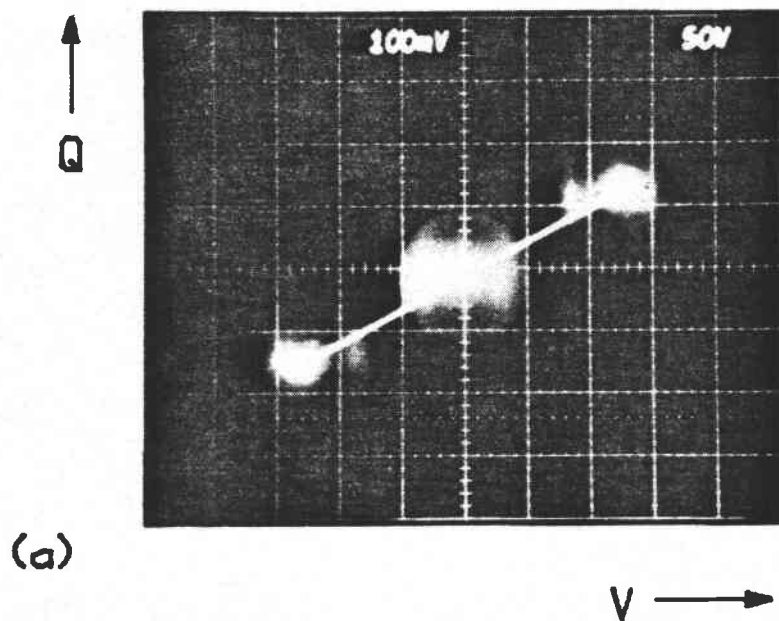
Thus by measuring  $\Delta V_C$ , information about  $P$ , and thus the actual

number of electrons involved, can be derived.

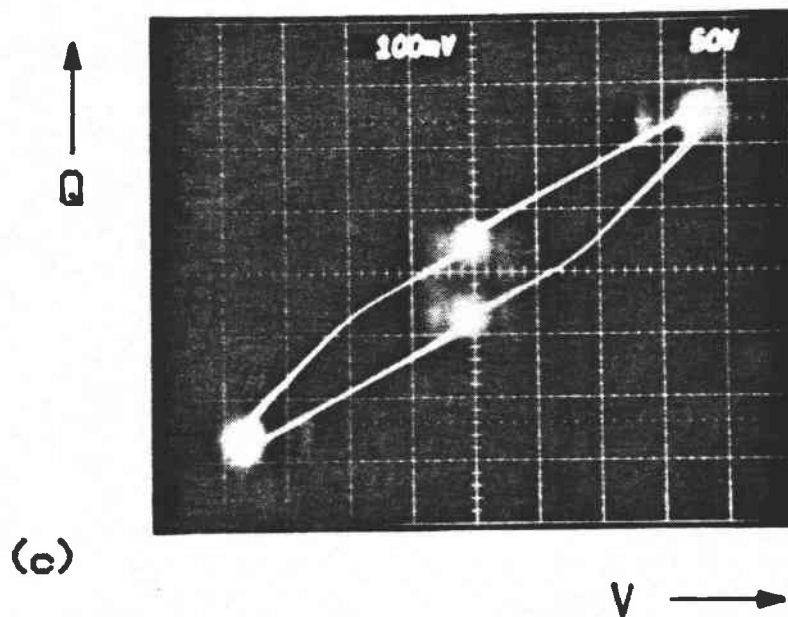
Experimental evidence which best indicates the electron trapping property of the ZnS-insulator interfaces is illustrated with the sensing capacitor charge plotted against concurrent driving voltage amplitude diagrams; or the Q-V diagrams [9] shown in figure 3.15. With the driving voltage below the threshold level  $V_{TH}$ , the trace of the Q-V diagram is a straight line which passes through the origin and has a slope corresponding to the total device capacitance, as is illustrated by diagram 3.15(a). When the voltage is increased to beyond the threshold limit, conduction current within the ZnS starts to flow and the Q-V curve will take the shape shown in figure 3.15(b), and a number of physical quantities can be obtained from it:

- (i) The total device capacitance can be calculated by measuring the slope of the line segment  $\overline{AB}$  as shown in the figure.
- (ii) The slope of line segment  $\overline{BC}$  indicates the total insulator capacitance.
- (iii) The area enclosed in the diagram reveals the power input into the device.
- (iv) The width of the diagram at  $V = 0$  gives  $\Delta Q_i$ , from which the polarization  $P$  can be calculated with equation (3.18).
- (v) The threshold voltage of the device is obtained from the X coordinate of point B.

As long as the driving voltage is not too far above the threshold level, the sections between point D, C and point E, B in figure 3.15(b) will be straight lines, i.e., the length of  $\overline{CB}$  equals  $\Delta Q_i$ . This suggests that after the electrons were trapped at the interface states,



(a)



(c)

Figure 3.15 The Q-V diagrams of a ZnS:Mn ACTFEL DEVICE that exhibits no hysteresis where (a) the driving voltage is below the threshold level, (b) above the threshold level, and (c) far above the threshold level.



none of them were able to escape from their trapping centers and move back toward the ZnS bulk when the driving voltage had fallen to zero, even if the polarization field encourages them to do so. Under high driving levels, the polarization field will become sufficiently large so as to cause electrons residing at the shallower interface states be tunneled out from their trapping centers and move back toward the other interface. This causes the external conduction charge  $\Delta Q_1$  to decrease as the driving voltage is reduced to zero. Therefore, the Q-V diagram will assume the shape shown in figure 3.15(c). When the driving voltage pulse is of the same polarity as the previous one, most of the induced ZnS electric field will be cancelled by the existing polarization field, thus causing little conduction current to flow. On the other hand, if the next pulse is of the opposite sign, the polarization field will be superimposed upon the driving voltage, which results in a very high effective ZnS electric field which will induce a large conduction current and therefore higher luminescence brightness, as is shown in figure 3.13(b). The increase in intensity for the initial light pulses shown in figure 3.13(a), is also a result of the polarization effect. As the sample is first excited from its off state by a sequence of driving voltages whose amplitude is just above the threshold level, the initial pulses will induce little conduction current, since the polarization field is still small. However, once conduction starts, the add-on effect of the polarization field will continue to increase the effective ZnS electric field, causing more conduction current per cycle, until a steady state is reached. This

process will lead to an increase in intensity in the initial light pulses observed in figure 3.13(a).

When studying the polarization characteristics of a hysteretic ACTFEL device, it was found that as the device is sustained in the hysteretic regime, the only difference of electrical parameters between its on and off states, is their polarization status - the on state has a large ZnS polarization while the off state has only a very small one. This is illustrated with the polarization versus driving voltage plot, the P-V curve, shown in figure 3.16. Based on this observation, it is concluded that a hysteretic ACTFEL device, when sustained within the memory regime, can be switched between its on and off states simply by altering its polarization status. This change of status can be achieved via a number of different approaches and some of them will be described in the next section.

### 3.6 Writing and Erasing of a ZnS:Mn ACTFEL Device Having Inherent Memory Effect

The methods for switching on or off an ACTFEL device can be classified into two categories: the electrical procedures and the optical procedures. The idea behind switching on the device, writing, is to create a ZnS polarization field and then take advantage of the electric field enhancement effect as the next driving pulse arrives, which will then trigger the conduction current flow thus causing electroluminescence. Switching off the device electroluminescence, (erasing), the process is just the opposite, i.e., instead of generating a ZnS polarization one wants to annihilate the polarization field and thus remove the field enhancement effect which keeps the device in

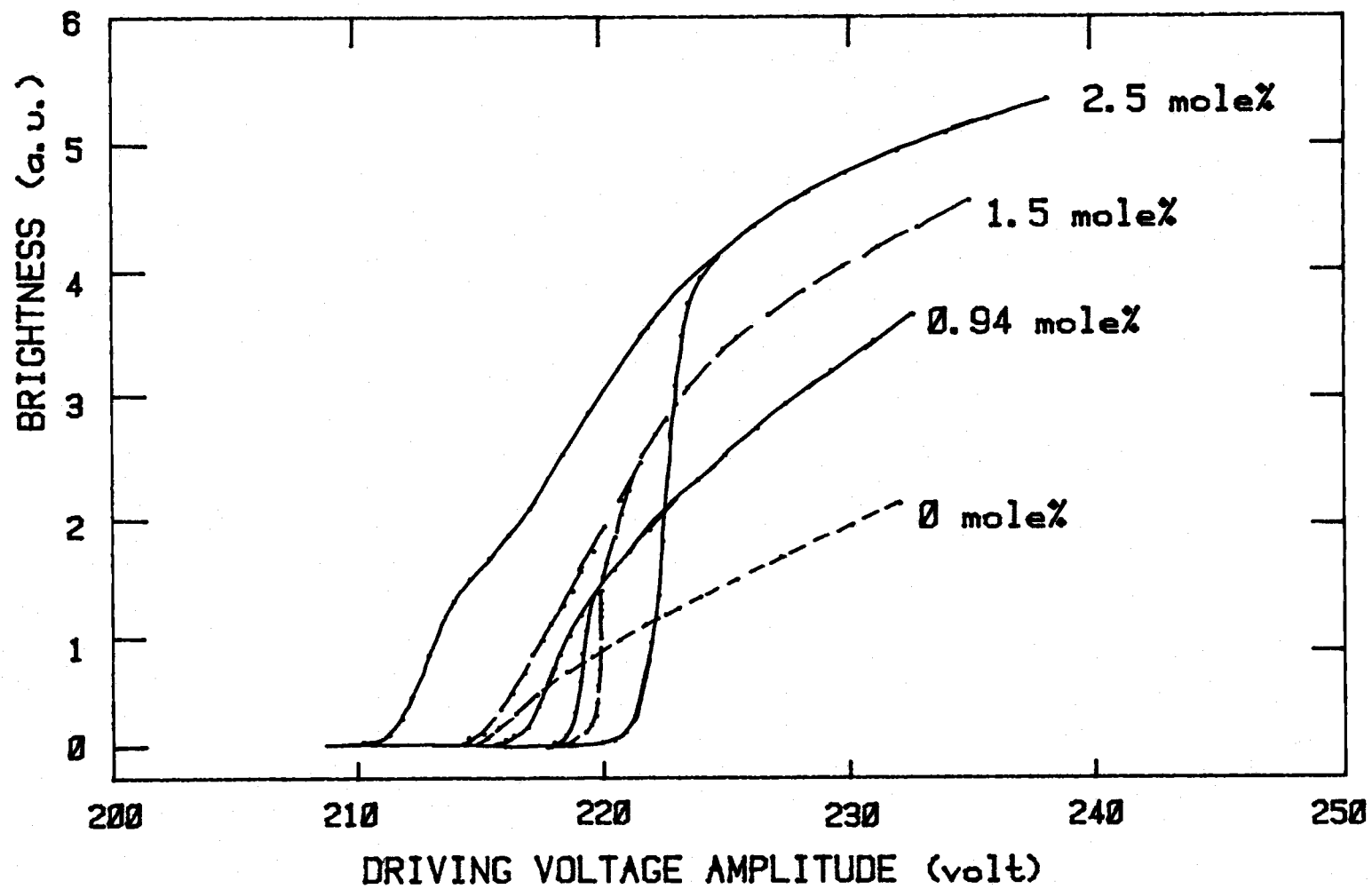


Figure 3.16 The P-V curves for samples with different  $\text{Mn}^{+2}$  doping concentrations.



its on state. The writing method includes the following:

- (i) Sustaining voltage amplitude modulation [32], [35],  
where the amplitude of one or more consecutive sustaining voltage pulses are suddenly raised to above the threshold level, which will induce conduction current flow and create a polarization field.
- (ii) Sustaining voltage pulse width modulation. When several consecutive sustaining voltages have their pulse width increased, the ZnS is then subjected to the electrical field of the sustaining voltage for an increased time which will cause some carriers be tunneled out from their trapping centers, these carriers then form the polarization field. This process is illustrated with the help of figure 3.17 where the B-V curves of a sample under driving voltages having various pulse widths are shown. It is seen that as the pulse width increases, the whole B-V curve shifts toward a lower voltage level. Referring to the figure, suppose that the sustaining voltage is at 140 volt, the pulse width at  $PW_4$ , and the sample in its off state, which correspond to point A in the figure. As a sequence of driving pulses having their pulsewidth increased to  $PW_1$ , the corresponding location of the luminescence brightness will then change to point B. Upon returning the pulse width back to  $PW_4$ , the resultant brightness will now be at the level indicated by point C. The purpose of "writing" is thus achieved.

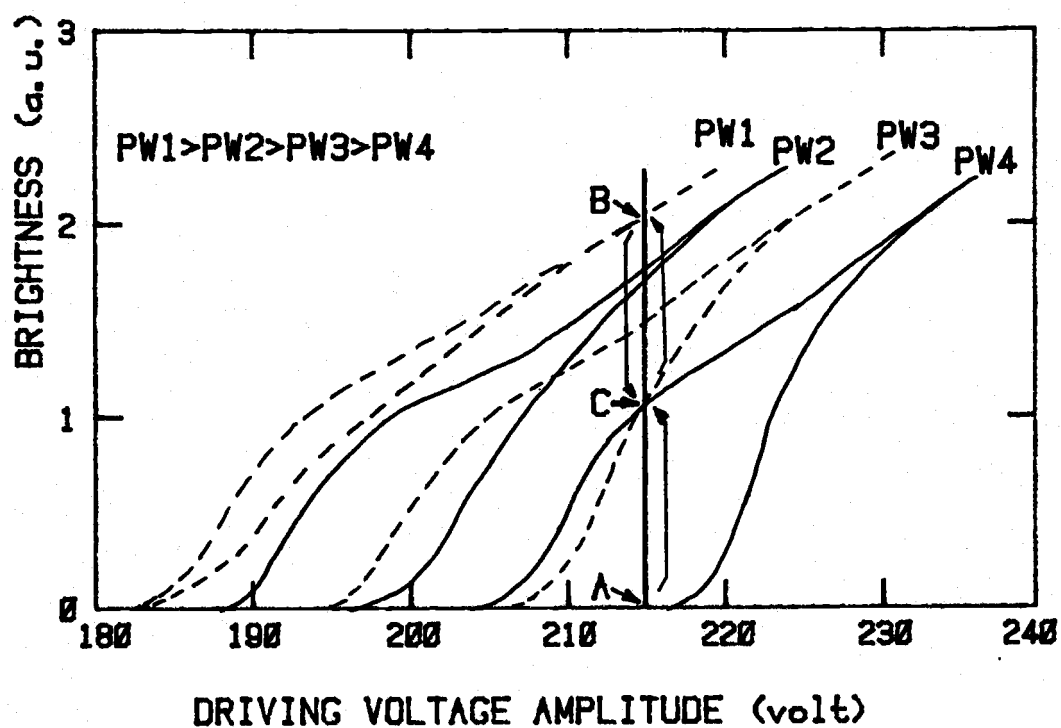


Figure 3.17 The pulse width dependence of the B-V curve and the writing mechanism of the pulse width modulation effect.

- (iii) Synchronizing u.v. light pulses with the Driving Voltages [32 34]. By illuminating the ACTFEL device with an u.v. light source, whose photon energy is greater than approximately 3.5eV, the ZnS layer will be turned into a conductor because of the photo-induced electron-hole pairs. If during this time, a biasing voltage is applied to the device, it will cause conduction current to flow and create a ZnS polarization.

With appropriate modifications, these three procedures can also be used to perform the task of erasing:

- (i) Sustaining voltage amplitude modulation. This is accomplished by reducing the amplitude of several driving pulses to a level just below the extinction voltage  $V_E$ .
- (ii) Sustaining voltage pulse width modulation. This process is accomplished by reducing the pulse width of several consecutive driving voltages. The lower limit of the pulse width is determined by the sustaining pulse width and amplitude.
- (iii) Synchronizing u.v. light pulses out of phase with the driving voltage pulses. It is obvious that if the device is illuminated with u.v. light pulses while the external biasing voltage is at zero volt, the photo-generated carriers within the ZnS layer will move under the polarization field until that field has been fully reduced to zero and hence the erasing process is accomplished.

Another writing and erasing method is to use the

electron beam direct addressing technique. This method is used in the EL CRT application which provided a very high resolution and selectively erasable image storage apparatus [37], [38].

### 3.7 The Aging Effects

Some physical quantities of a ZnS:Mn ACTFEL device are not stable during the initial hours of its operation after the device was made, and they go through certain changes. These quantities include the luminescence threshold voltage, the hysteresis width, the density of the bulk and interface states, and sometimes the steepness of the B-V curve rise at the threshold level [27]. The changes are collectively known as the "aging" process and can roughly be divided into two stages: the short term aging and the long term aging. The long term aging is a very slow process which occurs when the device has been continuously operated for several thousands of hours<sup>\*</sup>, and the most dominant effect is the shifting of the B-V curve toward a lower voltage level over some other thousands of hours. Study of this long term aging effect is beyond the scope of the work of this thesis and will not be discussed here. The short term aging process usually required less than 100 hours to develop under a  $1\text{KH}_2$  driving voltage excitation [39]. After that, the sample is said to have been "burnt in" and all of its physical quantities become quasi-stable. The actual burn in time is a function of both the driving frequency and the driving voltage level. A high driving voltage and

---

\* The actual time required is dependent of the excitation conditions, e.g., the driving voltage amplitude, the driving frequency, and the device temperature.

a high driving frequency will usually accelerate the aging process, therefore it is speculated that the controlling factor of the aging process is the total number of excitation cycles, rather than the total device operation time. The typical effects of short term aging on the B-V curve are shown in figure 3.18. Two apparent changes of the B-V curve are: (i) the increased threshold voltage, and (ii) the increased hysteresis width. The effect of aging on the B-V curve of an ACTFEL device is dependent on the fabrication details of that device, different results have been obtained for samples under some other fabrication processes which indicated that the hysteresis width actually decreases with short term aging [27].

The effects of deep trap states within the ZnS layer have been demonstrated by several investigators [24], [35]. Recently, some thermal and optical measurements on the ACTFEL devices have provided direct evidence for the existence of such deep traps. These measurements also indicated that the aging process, in addition to its effect on the threshold voltage and the hysteresis width, will create more deep trap levels within the ZnS layer [40], [41].

The polarization holding capability of the ZnS film also improves with aging. This is best illustrated with the polarization against time curves, obtained by using the sensing capacitor technique, shown in figure 3.19. As discussed earlier, the residual voltage across the sensing capacitor after the driving voltage has returned to zero, directly reflects the internal polarization status of the device. For a fresh sample, the polarization field that has been established by the previous driving voltage, will leak away after the driving voltage returns to zero as is shown in figure 3.19(b).

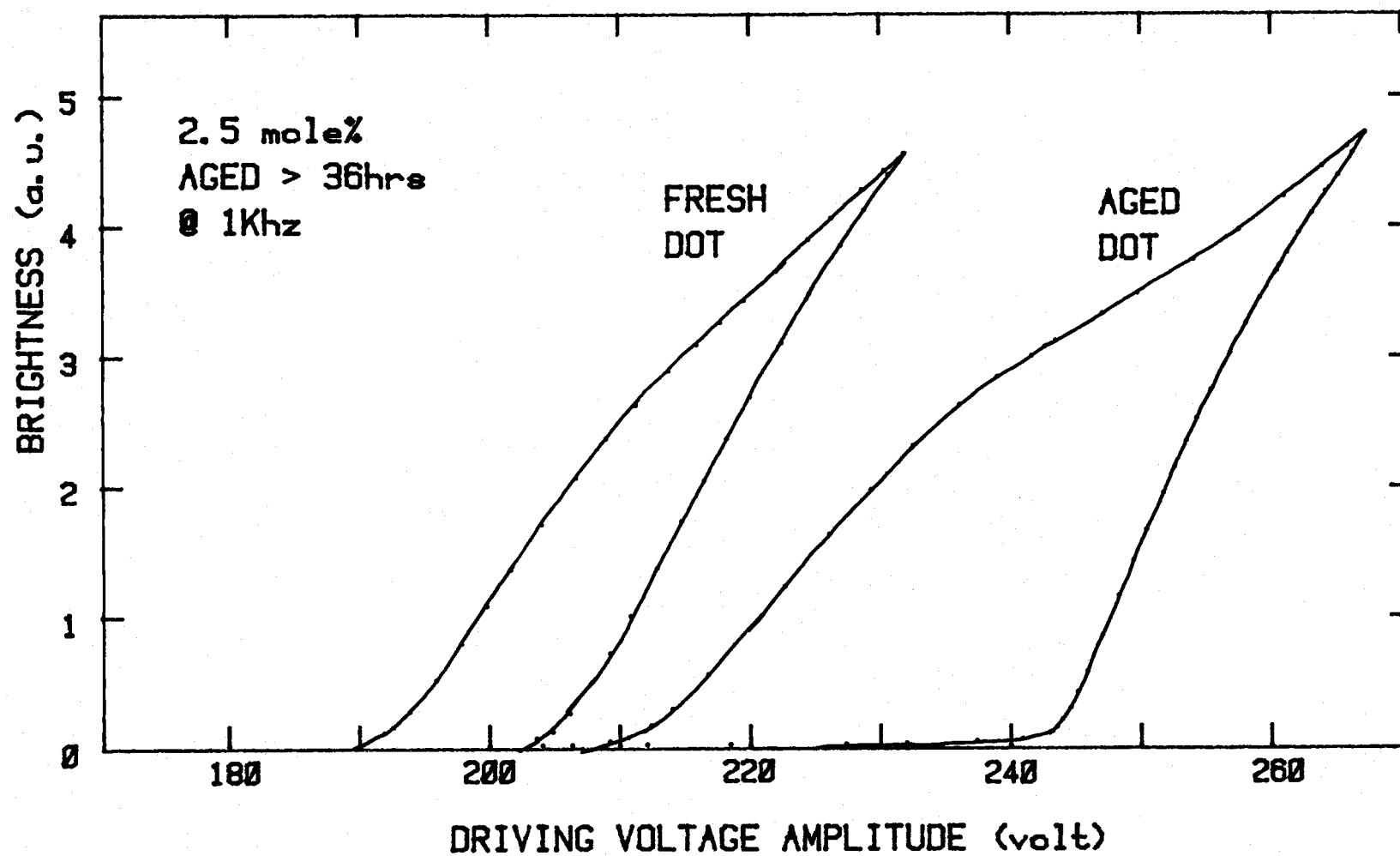


Figure 3.18 The aging effect on the B-V curve.

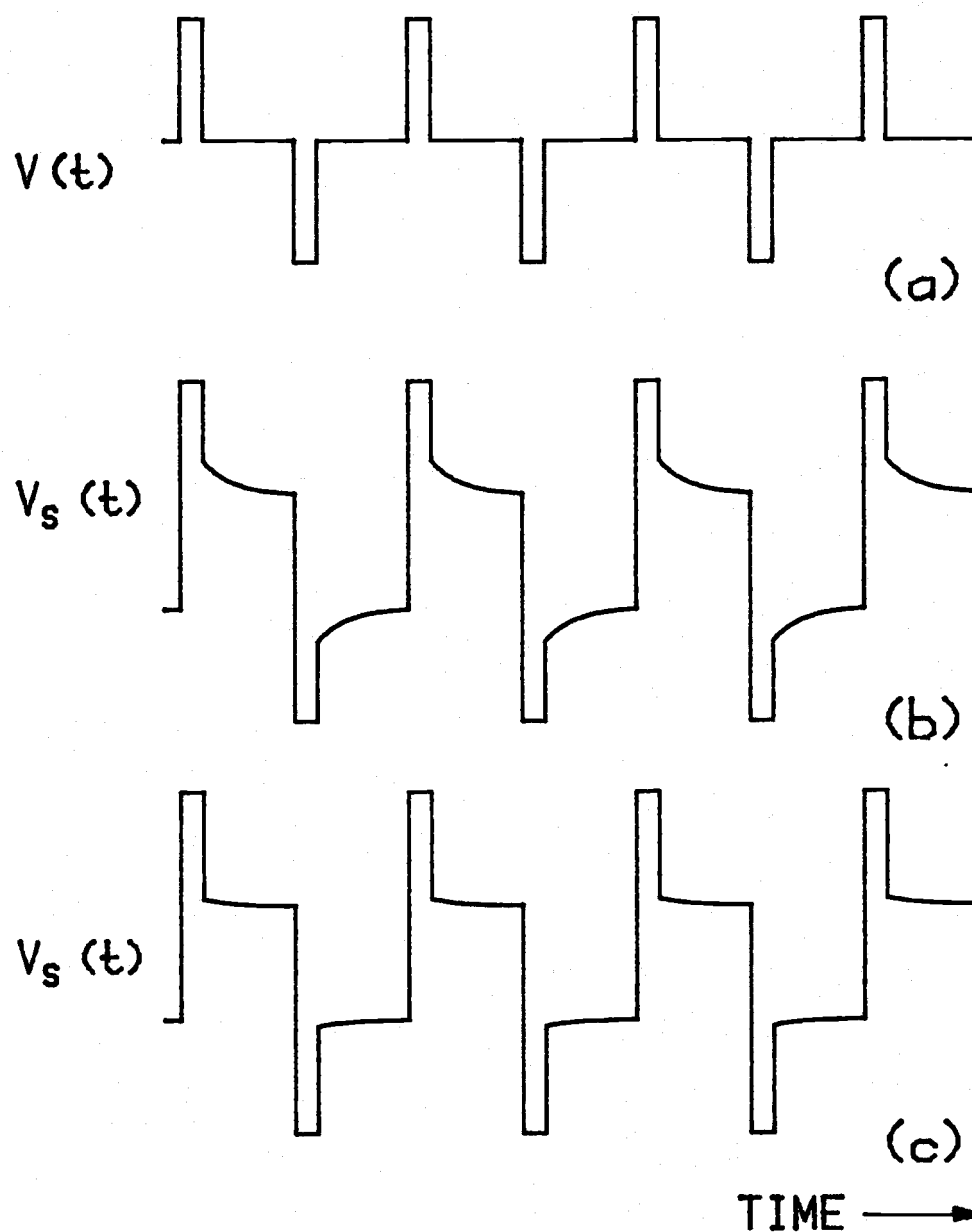


Figure 3.19 The timing diagram of (a) the driving voltage, (b) the sensing capacitor voltage induced by the driving voltage while the sample is newly fabricated, and (c) the same as in case (b) except the sample has been aged at 1kHz for 72 hours.

However, after the burn in process has been properly developed, this leakage phenomenon disappears, as is shown in figure 3.19(c). A plausible explanation is that when the sample is new, the density of both bulk and interface states of the ZnS layer is small, so that when the conduction electrons reach the ZnS-insulator interface, some of them are forced to reside on the shallower interface states. These are not stable under their own induced polarization field. As the aging process develops, more deep interface states are generated and thus most of the conduction electrons are trapped in the deeper states which are of course more stable under the polarization field. Another alternative interpretation of this improvement of the polarization holding capability of the ZnS layer with aging, is that it is due to the generation of more deep hole traps in the bulk during aging. This will provide a more stable, positive space charge distribution within the ZnS film and therefore, a better polarization stability.

### 3.8 A Model for the Electrical Writing and Erasing Process

As has been discussed earlier the writing and erasing processes for a hysteretic ACTFEL device, when sustained within its hysteresis regime, can be achieved simply by changing the polarization status of that device. The polarization is associated with the carrier generation and re-trapping processes within the ZnS film. In order for carrier generation to take place, the effective electric field within the active layer has to be larger than the threshold level  $E_{TH}$ . After that, conduction current will start to flow and the resulting



polarization will be a function of the initial ZnS effective electric field.

Consider the case where the insulators are not leaky. As the device is first subjected to a driving voltage which induces an electric field strength  $E_d$  within the ZnS layer, the resultant polarization  $P$  can be written as

$$P = \alpha E_d \quad (3.19)$$

where  $\alpha$  is the proportional factor which is a function of the initial ZnS effective electric field, it is very small if the electric field strength is less than  $E_{TH}$  and is large if when the electric field strength is larger than  $E_{TH}$ .

Once the polarization is created, it will induce a polarization field  $E_p$  and as the following driving voltage of the opposite polarity arrives, this polarization field strength  $E_p$  will be added onto the electric field strength  $E_d$  induced by the driving voltage alone and results in a larger effective electric field strength i.e.:

$$E = E_d + E_p = E_d + \beta P$$

where  $\beta$  is a proportion constant relating the polarization and its induced polarization field strength, which is a function of the distribution of positive space charges left behind in the ZnS bulky by the conduction electrons. This will be further considered in chapter 8.

For the electrical writing process, the sample starts from a nearly zero polarization level and the difference equations describing the polarization growing processes may be written as

$$P_{n+1} = \alpha(E_w + \beta P_n) \quad (3.21)$$

and

$$P_{n+1} = \alpha_w (E_s + \beta P_n) \quad (3.22)$$

for the driving voltage and the driving pulse width modulations respectively, where  $P_n$  is the polarization level after the  $n$ th modulated driving pulses,  $E_w$  is the electric field strength induced by the voltage modulated writing pulses,  $E_s$  is the sustaining pulse generated electric field strength, and  $\alpha_w$  is the  $\alpha$  factor when the driving pulse width is increased. For a given sustaining voltage,  $\alpha_w$  will be larger than  $\alpha$  due to the increase in the driving pulse width, however, the difference is small. This is to be expected since the conduction current, which is responsible for the polarization generation, flows mainly at the leading edge of the driving voltage, increasing of the driving pulse width will therefore cause but a small change in the final polarization level.

For the first modulated driving pulse, i.e.  $n = 1$ , the preceeding polarization is zero, therefore equations (3.21) and (3.22) become

$$P_1 = \alpha E_w \quad (3.23)$$

and

$$P_1 = \alpha_w E_s \quad (3.24)$$

respectively. It is clear from these equations that using the voltage modulation for writing is more efficient than pulse width modulation. Since while  $E_s$  can be chosen to be large, provided that the insulator doesn't break down, only a small variation in  $\alpha_w$  can be achieved by the driving pulse width modulation process.

After the modulated pulses, the device polarization will assume a steady state value according to the equation

$$P_{m+1} = \alpha(E_s + \beta P_m) \quad (3.25)$$

where  $P_m$  is the polarization level after the reapplication of the  $m$ th sustaining voltage pulse following the modulation processes.

Under steady state,  $P_{m+1} = P_m = P_{ss}$ , then

$$P_{ss} = \alpha E_s / (1 - \alpha\beta) \quad (3.26)$$

Since the device is sustained within its hysteresis regime,

$E_s + \beta P_{ss} > E_{TH}$ . The hysteresis width of the device  $\Delta V_{hys}$ , given by  $V_{TH} - V_E$ , can be calculated by observing that while the driving voltage is at the extinction level, the polarization satisfies

$$E_E + \beta P_E = E_{TH} \quad (3.27)$$

or when substituted in equation (3.26)

$$E_E + \beta \alpha_{TH} E_E / (1 - \alpha_{TH} \beta) = E_{TH} \quad (3.28)$$

where  $E_E$  is the ZnS electric field induced by the driving voltage alone at the extinction level,  $P_E$  is the corresponding polarization level, and  $\alpha_{TH}$  is the  $\alpha$  factor with the effective ZnS electric field strength at just above the threshold level. Rearranging equation (3.28), one has

$$E_E = (1 - \alpha_{TH} \beta) E_{TH} \quad (3.28.1)$$

and the hysteresis width can be calculated as

$$\begin{aligned} \Delta V_{hys} &= (E_{TH} - E_E)(C_i + C_Z)d_Z / C_i \\ &= \alpha_{TH} \beta E_{TH} d_Z (C_i + C_Z) / C_i \end{aligned} \quad (3.29)$$

where  $C_i$  is the total insulator capacitance,  $C_Z$  is the ZnS capacitance and  $d_Z$  is the film thickness.

Based on the model just described, certain predictions concerning

the hysteresis characteristics of the ZnS:Mn ACTFEL devices can be made.

- (i) The hysteresis width of a device will increase with the ZnS film thickness. This is because that since the conduction electrons which induce the polarization effect are traveling back and forth between the two ZnS-insulator interfaces, a thicker ZnS film will therefore lead to a higher ZnS polarization level. According to equation (3.19), the increased polarization level corresponds to a larger  $\alpha$  factor and from equation (3.29), it is seen that this will result in a wider device hysteresis. This has been confirmed by experimental studies [27], [42], where an increase of the hysteresis width, with increasing ZnS thickness, was observed.

- (ii) The ratio of the hysteresis width to the device threshold voltage, is independent of the thickness of the insulator films. This can be seen from equation (3.29) by noticing that the threshold voltage is given by

$$V_{TH} = E_{TH} d_Z (C_i + C_Z) / C_i \quad (3.30)$$

therefore

$$\begin{aligned} \Delta V_{hys} / V_{TH} &= [\alpha_{TH}^\beta E_{TH} d_Z (C_i + C_Z) / C_i] / [E_{TH} d_Z (C_i + C_Z) / C_i] \\ &= \alpha_{TH}^\beta \end{aligned} \quad (3.31)$$

which has no first order dependence on the thickness of the insulator layers.

- (iii) A higher steady state polarization level will lead to a larger hysteresis width. When an ACTFEL device is excited

by a driving voltage whose amplitude is above the threshold level, the steady state polarization level  $P_{ss}$  may be inferred from equation (3.26) as

$$P_{ss} = \alpha E_d / (1 - \alpha\beta) \quad (3.32)$$

where  $E_d$  is the electric field strength induced by the driving voltage alone.

The equation suggests that if the steady state polarization of a sample is larger than that of another, whilst both of them are under the same excitation conditions, the former one will have a larger  $\alpha$  factor than the latter. This larger  $\alpha$  factor will again lead to an increase in hysteresis width as indicated by equation (3.29).

This prediction is again supported by experimental results and is illustrated in figure 3.16 with the P-V plots of several samples, each with a different hysteresis characteristic. The figure also shows the  $Mn^{+2}$  concentration dependence of both the device hysteresis behavior and the threshold voltage level, both appear to increase with increasing  $Mn^{+2}$  concentration.

For erasing, the polarization has to be reduced from its high state to the low state. The difference equations describing this process are then

$$P_{n+1} = \alpha(E_2 + \beta P_n) \quad (3.33)$$

for the voltage modulation and

$$P_{n+1} = \alpha_2(E_s + \beta P_n) \quad (3.34)$$

for the pulse width modulation. Here,  $E_2$  is the electric field strength generated by the erasing voltage along,  $\alpha_2$  is the  $\alpha$  factor corresponding to the narrower erasing pulses and is smaller than  $\alpha$  at any given voltage level.

Equation (3.33) itself is not independent and is subject to the constraint

$$E_2 + \beta P_n \geq E_{TH} \quad (3.35)$$

i.e., the effective electric field will be large enough to trigger the ZnS conduction current. Similarly, equation (3.34) must be accompanied by

$$E_s + \beta P_n \geq E_{TH2} \quad (3.36)$$

where  $E_{TH2}$  is the threshold electric field strength for the narrower erasing pulses and will be larger than  $E_{TH}$ .

The polarization decrease induced by each of the erasing pulses are then

$$P_{n+1} - P_n = \alpha E_2 - (1 - \alpha\beta)P_n \quad (3.37)$$

and

$$P_{n+1} - P_n = \alpha_2 E_s - (1 - \alpha_2\beta)P_n \quad (3.38)$$

for the voltage and pulse width modulation respectively.

In order to make voltage modulation erasing more effective, equation (3.37) suggests that  $E_2$  is to be kept as small as possible, however, due to the constraint of equation (3.35),  $E_2$  can not be too small and thus, a compromise has to be made. The effectiveness in reducing the polarization level for the voltage modulated erasing pulses therefore, has a voltage dependence as shown in figure 3.11.

From equation (3.38) it is seen that in order to increase the erasing ability of the pulse width modulated driving pulses, the proportion factor  $\alpha_2$  must be kept small. Since the  $\alpha$  factor is not very sensitive to variations in the driving voltage pulse width as discussed earlier, it is necessary to invoke a substantial reduction of the driving pulse width in order to obtain a significant decrease of  $\alpha_2$ . This fact, plus the constraint of equation (3.36), indicates that  $\alpha_2$  usually cannot be modulated too far away from the sustaining value. Thus pulse width modulation is not as effective as voltage modulation in erasing an ACTFEL device.

In summary, the proportionality factor  $\alpha$ , which relates the effective ZnS electric field strength to its resultant polarization level, plays an important role in determining the hysteretic characteristics of an ACTFEL device. The apparent hysteresis width  $\Delta V_{\text{hys}}$  is determined from equation (3.29) by this  $\alpha$  factor, the ZnS threshold electric field strength, and the thickness of the film. The additional constraint of equations (3.35) and (3.36) indicate that, when using either of the two electrical modulation methods, it is usually more difficult to erase a sample than to "write" on it.

## TIME-RESOLVED ELECTROLUMINESCENT SPECTRA

4.1 Experimental Techniques

The apparatus for the time-resolved electroluminescent spectra measurement is shown in Figure 4.1. The ACTFEL device is excited by 500 Hz alternating-polarity narrow pulses with a 10  $\mu$ s pulse width and a 200 nS rise time. The light pulses emitted by the sample are focused, with the aid of a f/1 quartz lens onto the entrance slit of a Jarrell-Ash 82-410 monochromator. An u-v extended 1P28 photolumultiplier, with a 50  $\Omega$  termination resistor to ensure a good frequency response, attached to the exit slit, provides the electrical signal corresponding to the light pulses emitted at various wavelengths. This signal is then fed into the PAR 162 boxcar signal averager and a TEK 7603 oscilloscope. With the gate signal from the boxcar also displayed on the oscilloscope in the chopped mode, the pre-amplifiers of the boxcar are then adjusted to sample the light pulse signals at any chosen delay time.

After a sequence of signal averaging and processing, the d.c. output from the boxcar, which corresponds to the light intensity at that chosen delay time, is fed into the y input of a TEK 7313 storage oscilloscope and an HP 7004A x-y recorder. A time-resolved spectrum is obtained by scanning the monochromator through the desired wavelength of the spectrum and feeding the analog signal, corresponding to the wavelength, to the x-axis of the two recording devices. The light intensity versus time curve may then be plotted in a similar



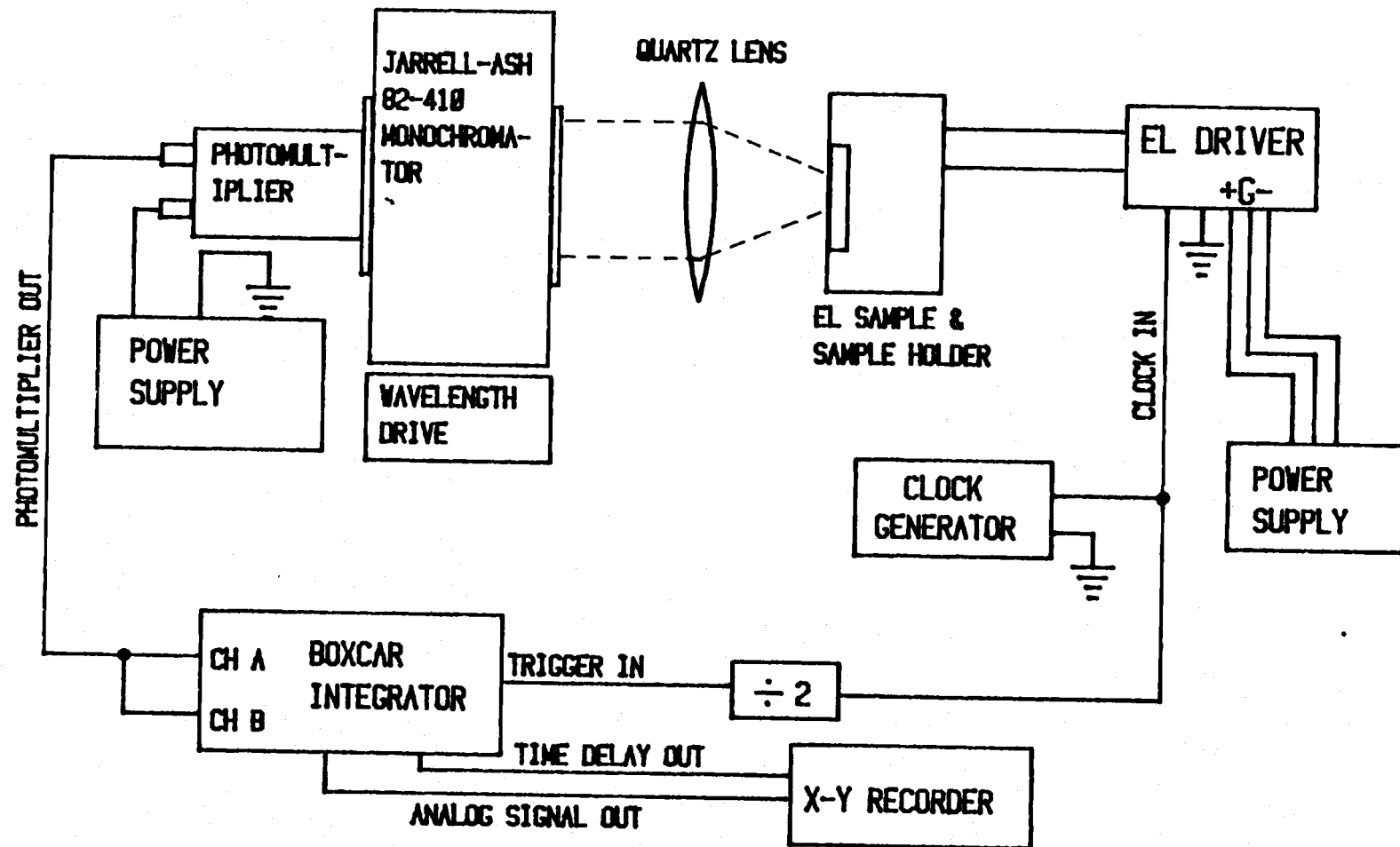


Figure 4.1 Measurement system for investigations of time resolved spectra.

manner, with the analog voltage corresponding to the relevant time delay fed into the x-input, whilst the sampling window scans through the chosen delay range. The data obtained in this experiment, has not been corrected to the frequency response of the monochromator and the photomultiplier. However, the corrections will not have any significant effect on the appearance of the shape of the data.

#### 4.2 Time Resolved Spectra

The time resolved spectra of photoluminescence and electroluminescence of ZnS:Mn ACTFEL devices have been reported by Tanaka et al. [23]. Their results, indicating a broad-band self-activated emission in photoluminescence which was absent in the electroluminescence, were based on measurements in the microsecond region. A closer examination of the electroluminescence spectra reveals that a blue broad-band emission, with a decay time of several hundred nanoseconds, occurs immediately after the leading edge of the excitation. In figure 4.2, the photomultiplier response versus time for the whole electroluminescent emission is given, whilst in figure 4.3 the same response is plotted with the addition of a low-pass (<500 nm) filter. Since the main  $5860 \text{ \AA Mn}^{+2}$  peak is now filtered out, the fast blue emission becomes clearly recognizable.

The time-resolved spectra for a ZnS sample, with no  $\text{Mn}^{+2}$  doping, is shown in figure 4.4 at various sampling delay times. The peak emission occurs at around  $4300 \text{ \AA}$  and the multi-layer interference effects, characteristic of the thin-film sandwich structure, are manifested in the periodic structure evident in the spectra. This

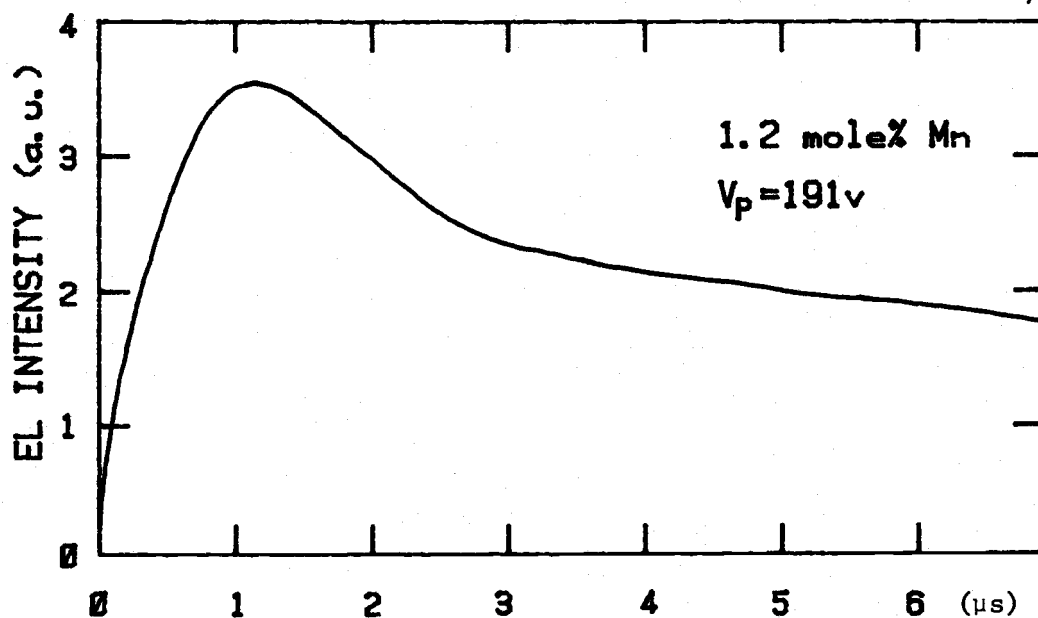


Figure 4.2 The full EL intensity versus time.

TIME (micro second) →

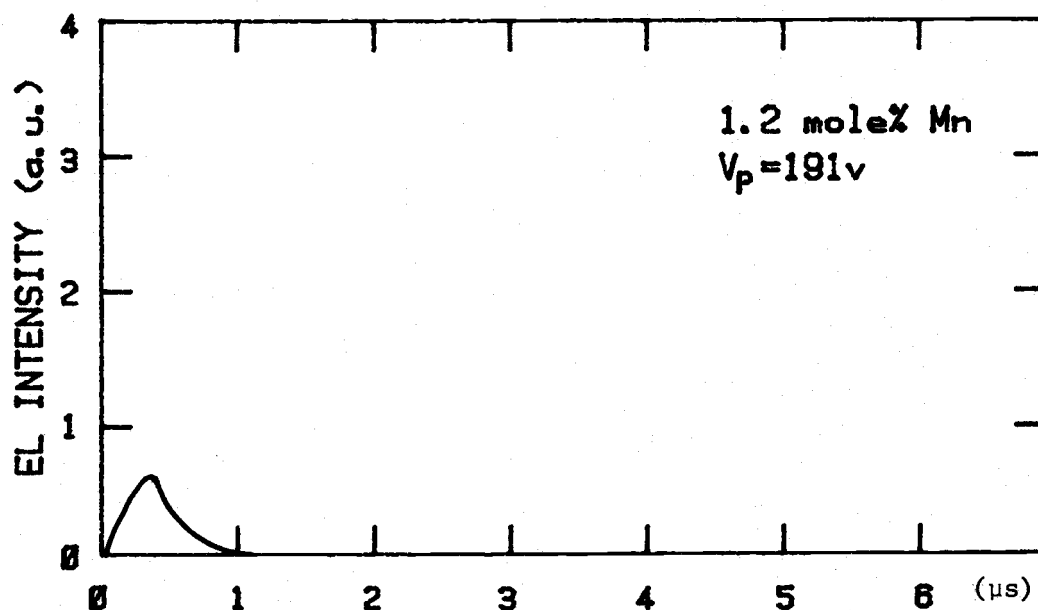


Figure 4.3 Low pass filtered EL emission  $\lambda < 500$  nm which eliminated the  $\text{Mn}^{+2}$  contribution and revealed the faster decaying shorter wavelength component. The vertical sensitivity is slightly reduced to a 10% pass band attenuation of the filter.

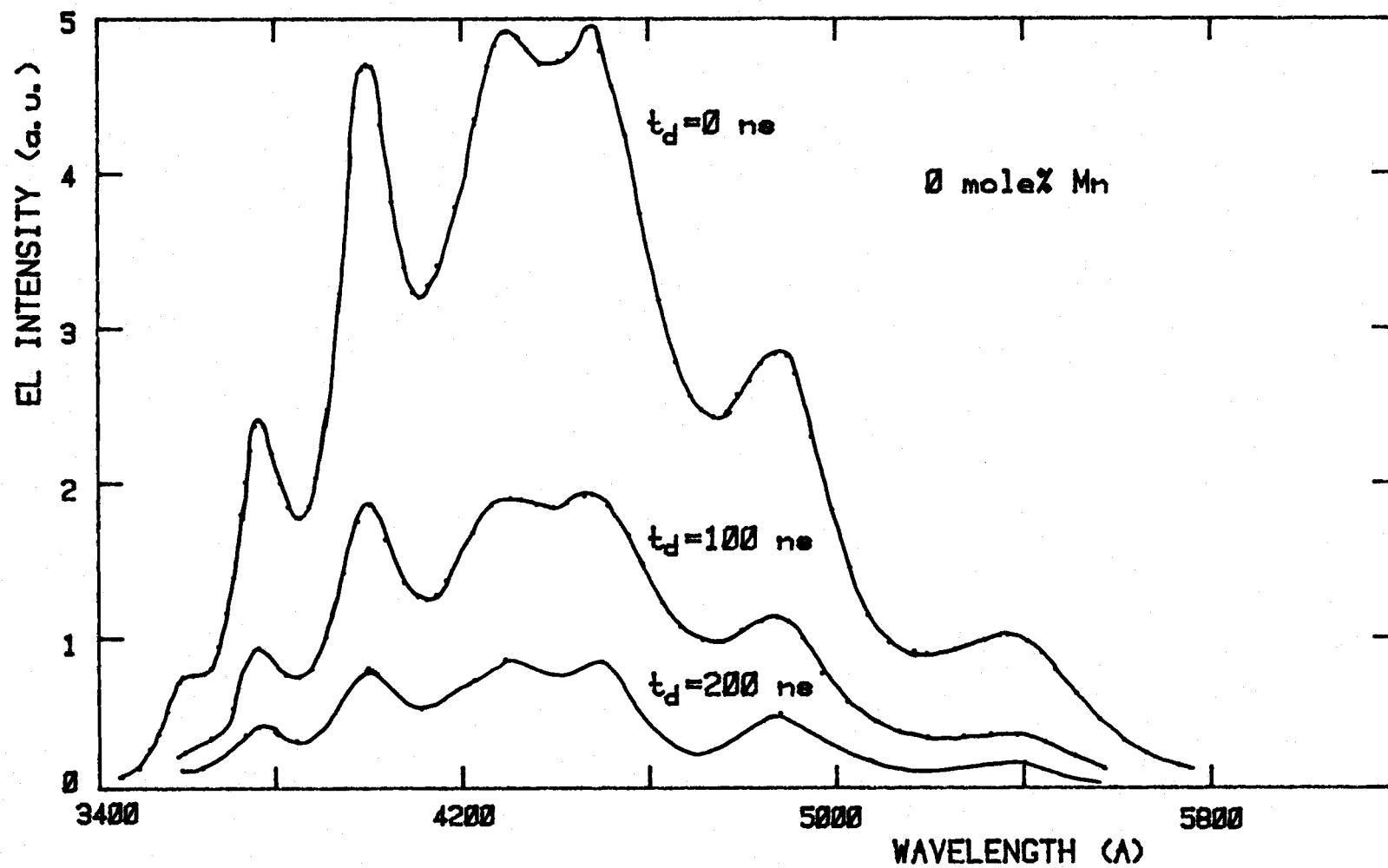


Figure 4.4 Spectra of a ZnS sample, with no Mn doping, at various delay times ( $t_d$ ) after the excitation. The whole spectra decays monotonically to zero.

broad sub-band gap emission is probably due to donor-acceptor (D-A) recombination. As time elapses the whole spectrum decays monotonically. In figure 4.5 the time-resolved electroluminescent spectra is shown for a ZnS:Mn sample with 0.99 mole %  $\text{Mn}^{+2}$  doping. Two salient features are that in the presence of the  $\text{Mn}^{+2}$  ions, the blue emission intensity has decreased and a broad emission band with a peak at  $5680 \text{ \AA}$ , corresponding to the main  $\text{Mn}^{+2}$  peak has appeared. In addition the time resolved spectra indicates that whilst the blue emission is decaying monotonically as in the previous sample, the yellow  $\text{Mn}^{+2}$  emission is enhanced over the first few tenths of a microsecond. A linear plot of light output against time for various wavelengths, figure 4.6, shows that the yellow  $\text{Mn}^{+2}$  peak increases at a rate approximately proportional to the amplitude of the blue emission.

The spectra of figure 4.7 is for a heavy doped  $\text{Mn}^{+2}$  sample at  $t = 0$ . Comparing this spectra with the correspondent  $t = 0$  curves in figures 4.4 and 4.5, there is considerable relative increase in the  $\text{Mn}^{+2}$  peak at  $5680 \text{ \AA}$  and a corresponding decrease in the blue emission.

### 4.3 Discussion

The origin of the broad sub-band-gap blue emission, from  $3400 \text{ \AA}$  to  $5300 \text{ \AA}$ , observed in the electroluminescence spectra of the ZnS:Mn ACTFEL devices is still a subject of much discussion. Skolnick [43] suggests that this broad emission band is most likely due to radiative inter-band transitions between higher conduction bands of the ZnS lattice. Others believe that it is due to donor-acceptor pair recombination processes [44]. A third argument, which is essentially

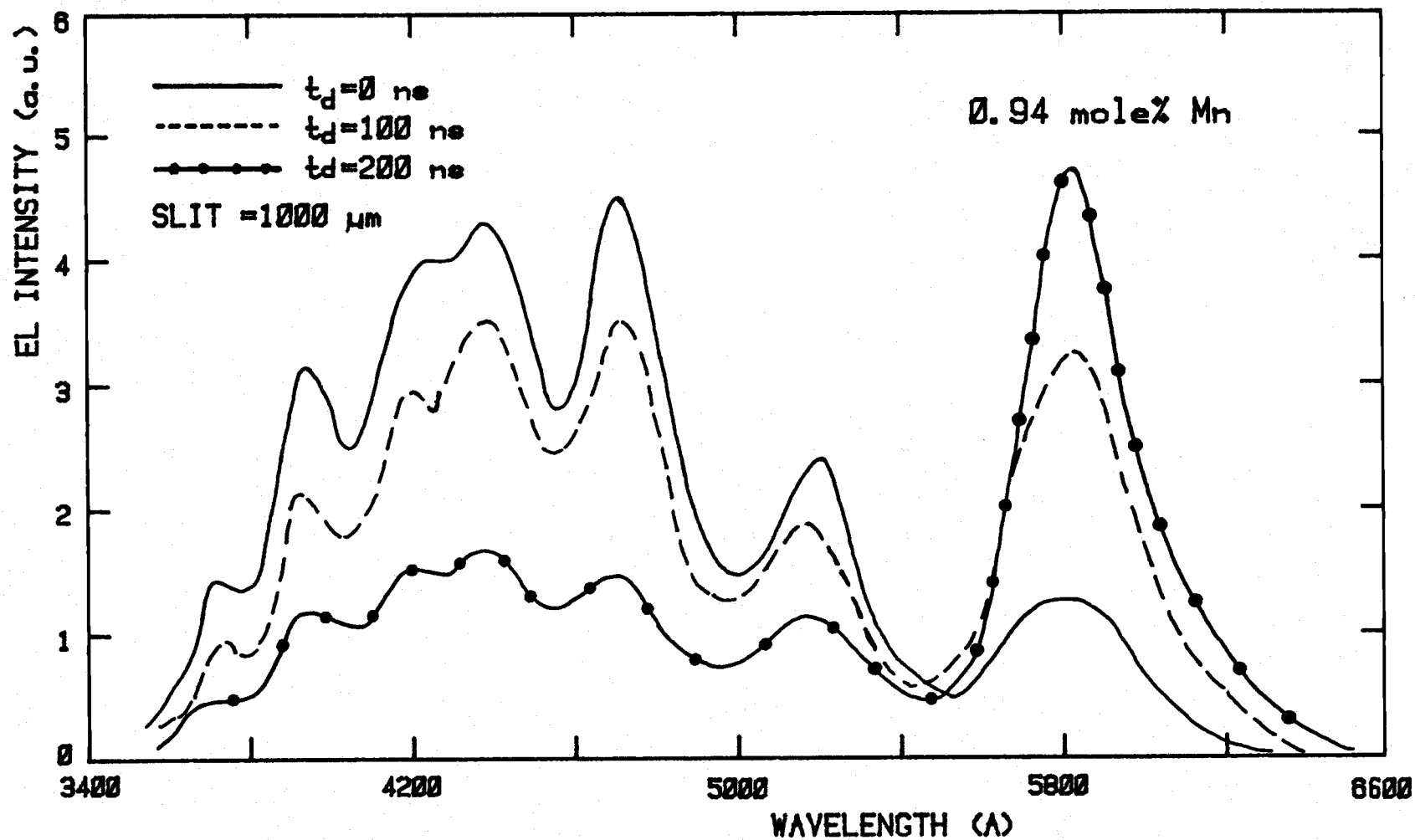


Figure 4.5 The time resolved spectra for a ZnS:Mn sample with non-hysteretic doping. The figure shows the growth of  $\text{Mn}^{+2}$  peak while the broad band emission is decaying.

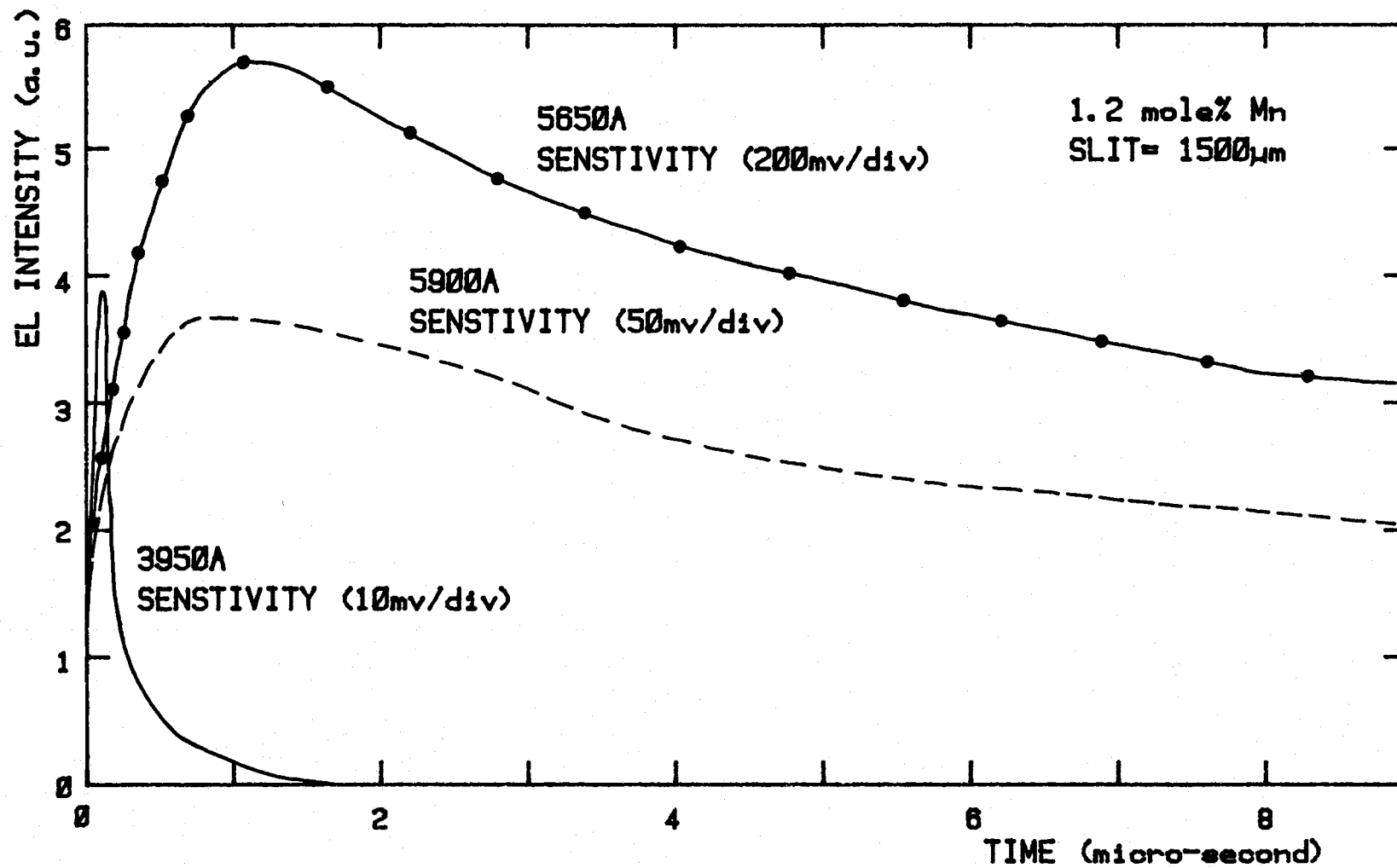


Figure 4.6 The linear plot of light intensity versus time for various wavelengths. The sensitivity for different wavelengths have been changed so that all three curves can be shown together. The rate of increase in  $Mn^{+2}$  emission intensity appears to be proportional to the broad band amplitude.

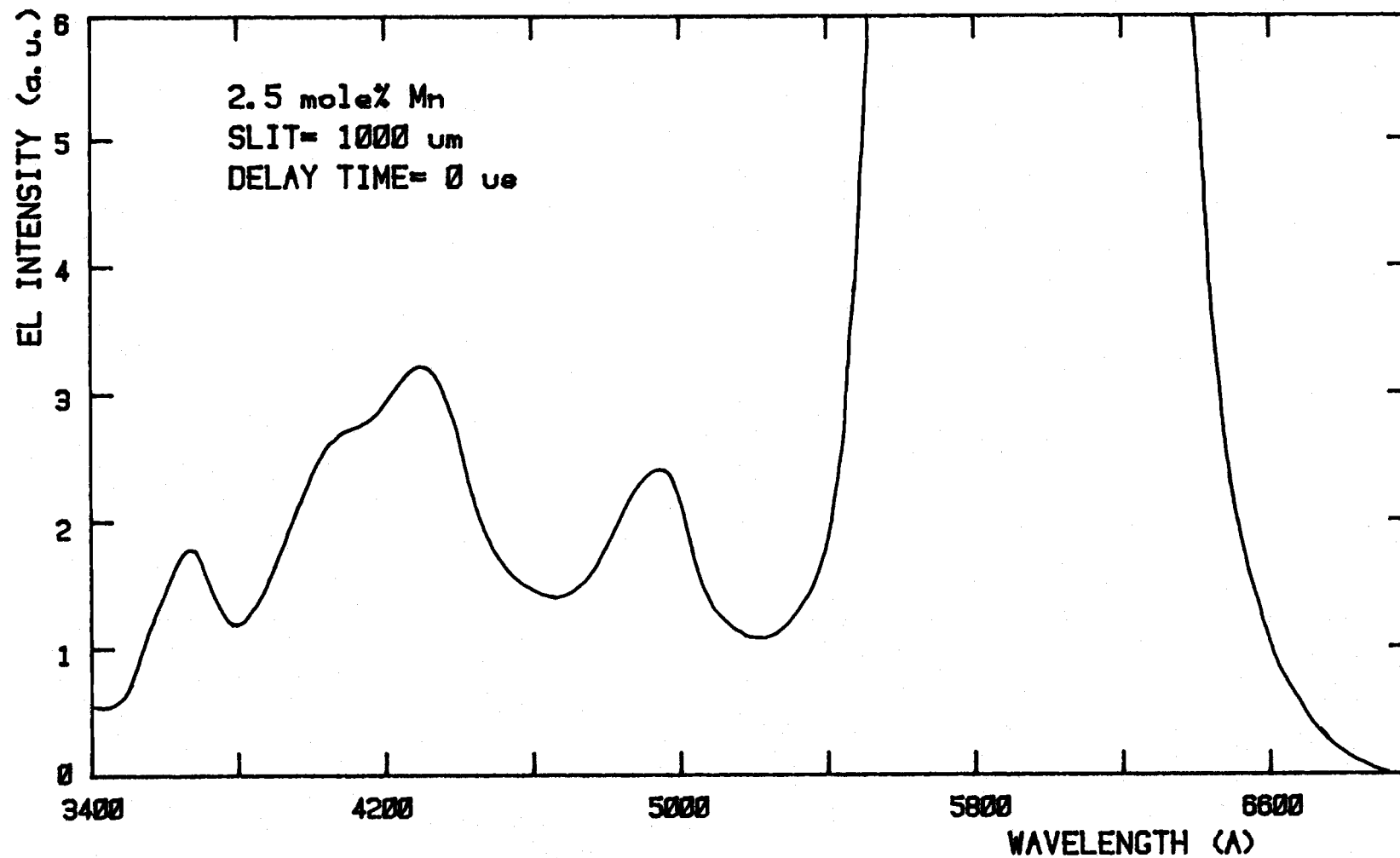


Figure 4.7 EL emission spectra for a heavily doped hysteretical sample at  $t = 0$ . The figure indicates that the  $\text{Mn}^{+2}$  emission increased significantly whilst the broad band emission was reduced in comparison with spectra from other doping level samples.



the same as the donor-acceptor pair philosophy, is that this broad emission band is due to electronic de-excitation of the self-activated centers within the ZnS film [24]. A self-activated center within the ZnS consists of a zinc vacancy  $[V]_{Zn}^{-2}$  and a substitutional Cl impurity ion residing on one of the four sulfur sites surrounding the zinc vacancy [45]. From studies of the polarization characteristics of the self-activated complexes, written as  $(V_{Zn} - Cl_S)^-$ , Koda and Shionoya [46] have suggested that this complex has the geometrical structure shown in figure 4.8. The broad blue-band self-activated luminescent transition occurs between a donor like upper level, due to the Cl atom at a S site, and the acceptor like ground level associated with the zinc vacancy [47]. Those self-activated centers also show up in the ZnS photo-conductivity effects and will be discussed in chapter seven later.

In order for the mobile electrons to excite those donor-acceptor like self-activated centers, the electrons need to acquire at least a minimum amount of kinetic energy, which means that a high electric field and a decent scatter free distance are needed. From the data presented in figures 4.4, 4.5, and 4.7, it is clear that the intensity of the blue emission band is reduced as the device  $Mn^{+2}$  concentration increases. These data were obtained with all of the samples excited at their saturation level rather than normalizing them to have the same yellowish  $Mn^{+2}$  emission intensity. If one chooses the latter to be the standard, different conclusions may have been drawn [48], since in that case, the samples with a high  $Mn^{+2}$  concentration will have to be excited harder than those

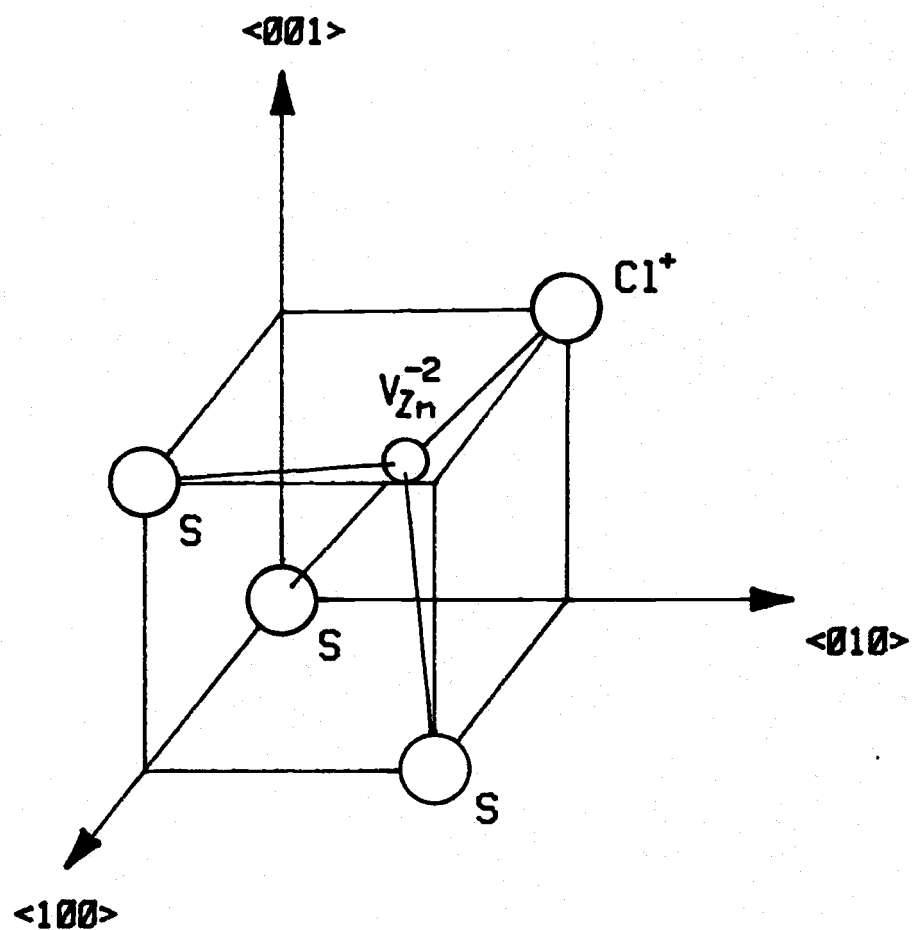


Figure 4.8 Model of the chlorine associated self-activated luminescent complex ( $V_{Zn}^{-2}-Cl^+$ ) within the ZnS cubic lattice (after Koda and Shionoya, [25]).

intermediately doped ones, because of the poorer  $\text{Mn}^{+2}$  luminescence efficiency of the high  $\text{Mn}^{+2}$  doping samples [24], [49], [50].

Two plausible interpretations for the  $\text{Mn}^{+2}$  concentration quenching effect of the blue band emission are as follows:

- (i)  $\text{Mn}^{+2}$  ions when incorporated into the ZnS will go preferentially onto the  $[\text{V}]_{\text{Zn}}$  site, therefore reducing the density of the blue-emitting self-activated centers [24].
- (ii) The mean free path that an electron can travel, is reduced by doping the ZnS film with  $\text{Mn}^{+2}$  ions. This may have resulted from the changes in the stoichiometry of the ZnS lattice due to difference in physical dimensions between the  $\text{Mn}^{+2}$  and the  $\text{Zn}^{+2}$  ions. In later sections, where the residual field induced charge and the photoconductivity measurements are discussed, it will be shown that the density of deep levels within the ZnS layer is associated with its  $\text{Mn}^{+2}$  doping concentration which increases as the  $\text{Mn}^{+2}$  doping increases. Those deep levels may further hinder the motion of conduction electrons.

## THE TEMPERATURE EFFECTS

### 5.1 Introduction

In order to clarify some of the physical processes responsible for the EL characteristics, systematic observations of the optical and electrical behavior as a function of temperature have been made. These measurements include the brightness, threshold voltage, radiation decay time, Mn excitation efficiency, hysteresis characteristics and the amount of ZnS dissipative current. The study indicated that the temperature effects on the optical properties of the device was most pronounced for samples with high Mn concentration, in excess of 1 mole percent. Conversely, the electrical characteristics were found to be more sensitive to temperature changes for low doped samples.

### 5.2 Experimental

The sample fabrication details have been described in the opening section of chapter II. As was discussed in section 3.4, the Mn doping is of particular significance in the determination of device characteristics [1]. Samples containing manganese of more than one mole percent show both hysteresis and concentration quenching of the electroluminescence. To investigate the effects of Mn doping, measurements were made on representative samples with 0.2, 1.3, 2.14 and 2.7 mole percent Mn respectively. This range of Mn concentration includes both hysteretic and nonhysteretic devices [4].

The driving voltage used was alternating polarity pulses with a pulsewidth of 10  $\mu$ S and a rise time of 200 nS. The devices were mounted on the temperature controlled dewar system which enabled a temperature range from 90K to 500K to be used. The output from the photomultiplier used to detect the electroluminescent light pulses was terminated in a 50  $\Omega$  resistor to ensure a good frequency response ( $>40$ MHZ). Final recording of the pulse signal was done with a boxcar signal averager. The polarization induced by conduction current within the ZnS layer when the sample was on, was measured with the sensing capacitor technique described earlier in chapter 3. Figure 5.1 shows the block diagram of the measurement set up.

### 5.3 Results and Analysis

#### 5.3.1 Effects on Electroluminescent Brightness

The brightness was found to be a monotonic decreasing function of temperature. The brightness versus peak driving voltage curves, the B-V curves, for devices with differing  $\text{Mn}^{+2}$  doping concentrations are shown in figure 5.2(a), (b) and (c). It is noticed that the thermal effect on the saturation brightness of these devices is more pronounced for samples with a higher  $\text{Mn}^{+2}$  doping concentration. The highest  $\text{Mn}^{+2}$  doping sample investigated, 2.7 mole percent, showed that its brightness increased by a factor of more than three when the device temperature decreased from 296K to 100K. For the 0.2 and 1.3 mole percent doping, however, the increase was less than 30 percent over the same temperature range.

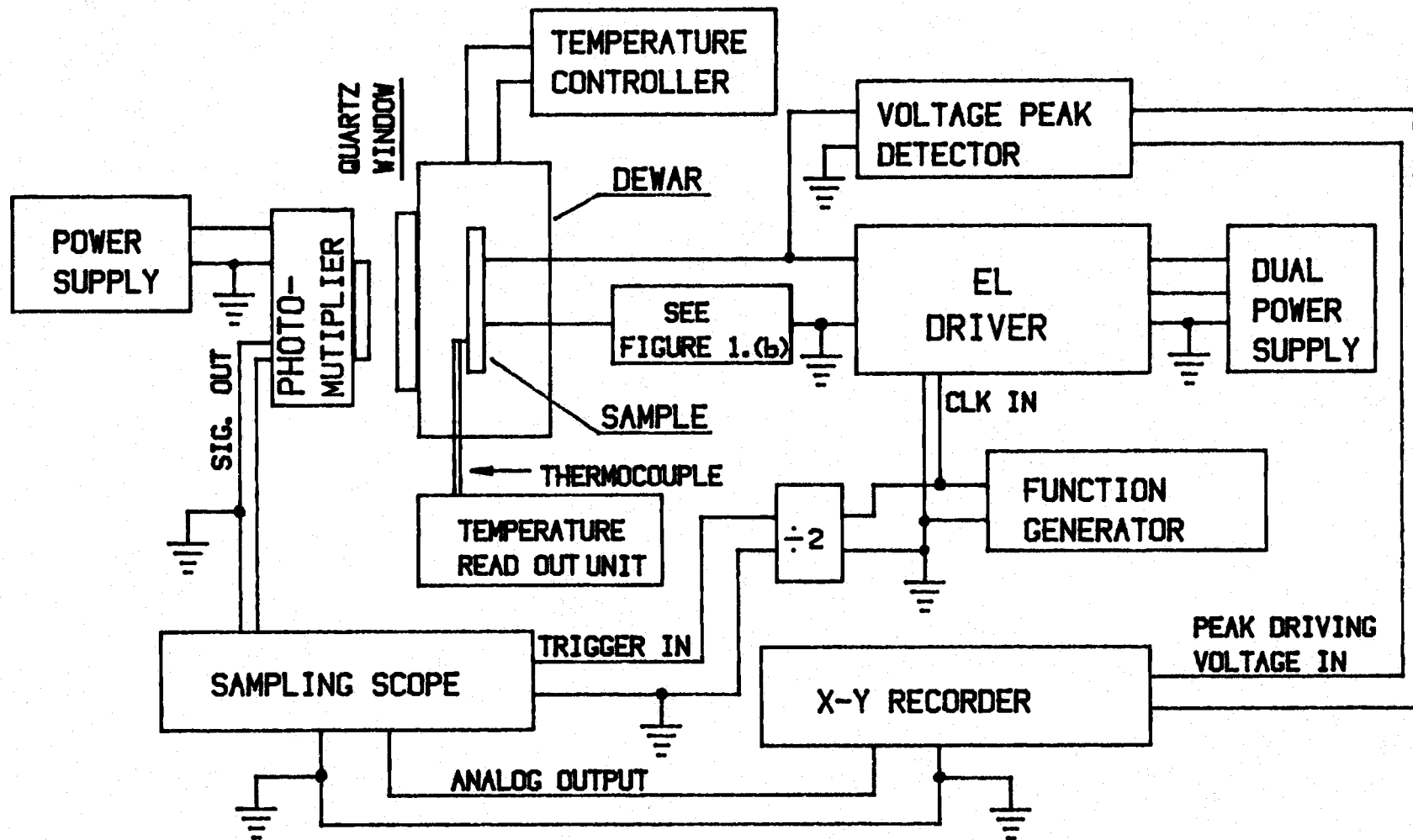


Figure 5.1(a) The measurement system for investigating temperature effect.

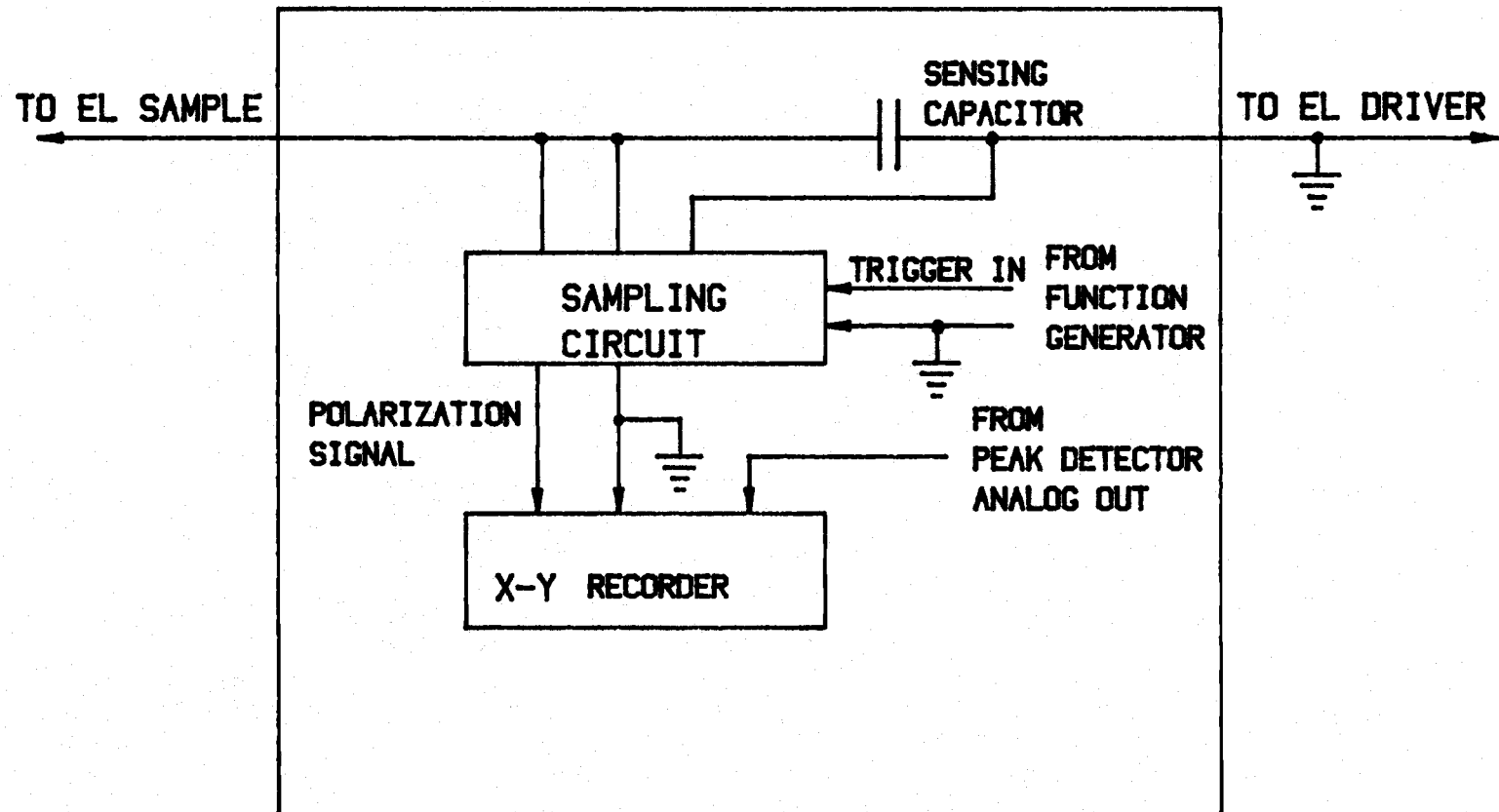
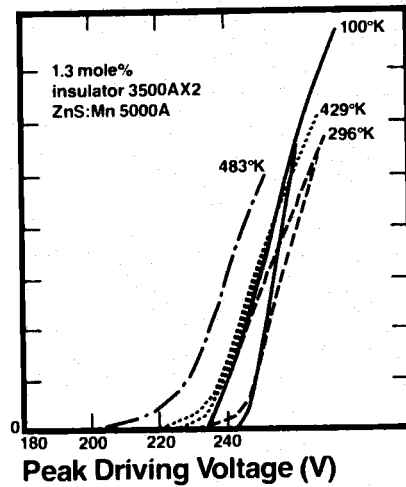
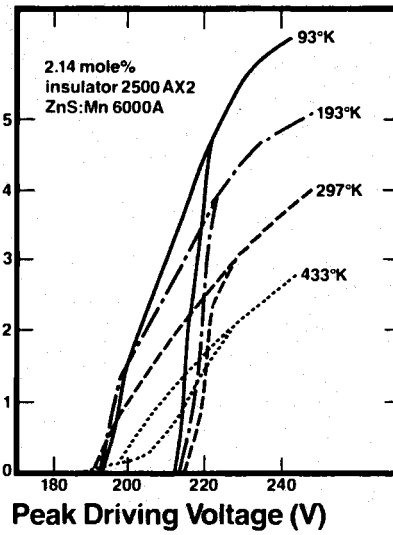


Figure 5.1(b) Modification of figure 5.1(a) for the polarization measurement. For the brightness measurement, a short circuit is substituted for the equipments within the square frame.

(A) Average Brightness (Arbitrary Units)



(B) Brightness (Arbitrary Units)



(C) Brightness (Arbitrary Units)

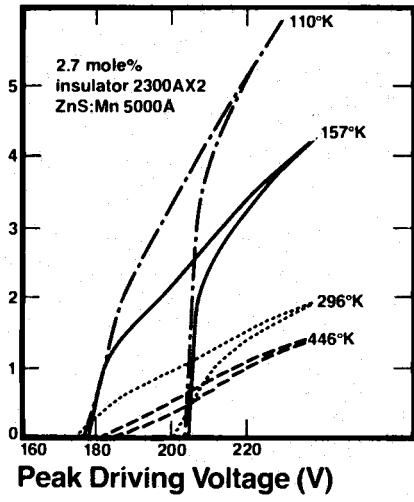


Figure 5.2 (A), (B), and (C). Average brightness versus peak driving voltage at various temperatures. The samples are distinguished mainly by differences in Mn concentration. The more heavily doped samples show more sensitivity.



### 5.3.2 Effects on Polarization

The temperature dependence of the polarization (P) versus peak driving voltage curves, the P-V curves, for the above three samples are shown in figure 5.3(a), (b) and (c). Unlike the previous B-V curves, only minor variations in the polarization characteristics were observed as the temperature was lowered from room temperature to 100K. Since the polarization is directly related to the number of conduction electrons, as has been discussed earlier, the small changes of the polarization level rules out the possibility that the brightness enhancement at low temperatures is due to more conduction electrons traveling back and forth between two ZnS-insulator interfaces and thereby exciting more  $\text{Mn}^{+2}$  ions. This conclusion is illustrated by simultaneous comparison of the temperature dependence of the saturation brightness and its corresponding polarization. The saturation brightness, in the absence of a standard definition, was arbitrarily chosen to be the brightness where the driving voltage is 10 percent above the threshold level. In figure 5.4(a) and (b), this saturation brightness and its corresponding polarization for several samples were plotted as a function of temperature. This data has been normalized to the value at 100K. The relative temperature sensitivity of the brightness and of the polarization for each sample can be easily compared from these normalized plots. It is apparent that the variation in brightness can not be due to changes in the number of conducted electrons. Figure 5.4(a) also indicated that the temperature effect on device brightness is more pronounced for samples having a higher  $\text{Mn}^{+2}$  doping level.

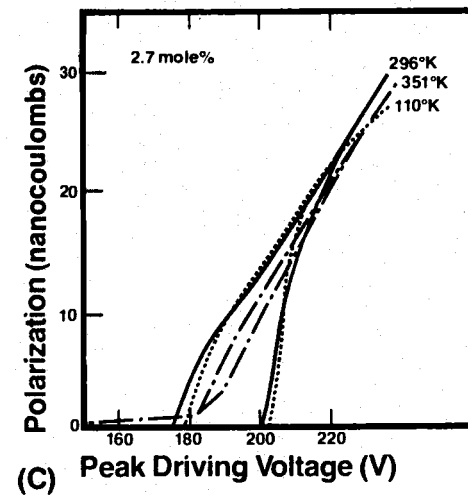
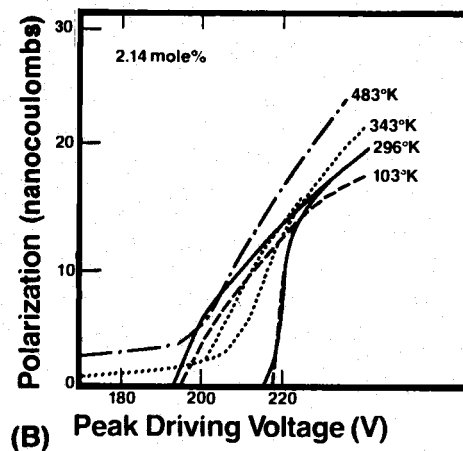
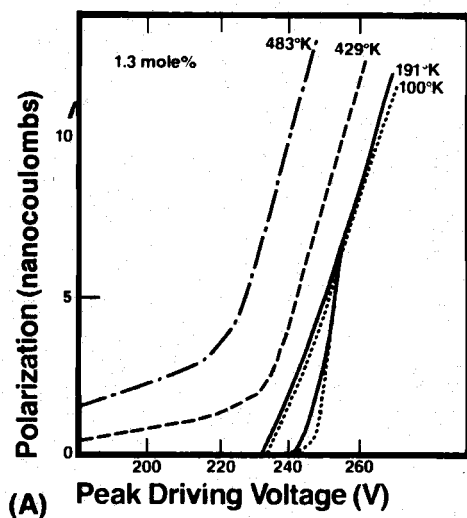


Figure 5.3 (A),(B), and (C). Polarization versus peak driving voltage at various temperatures. Note that at 300°K and below, the polarization is insensitive to temperature for all samples. This behavior is in contrast to the behavior of the brightness voltage curves shown in Figure 2. Above 300°K a 'leakage current' component appears even below the threshold level.

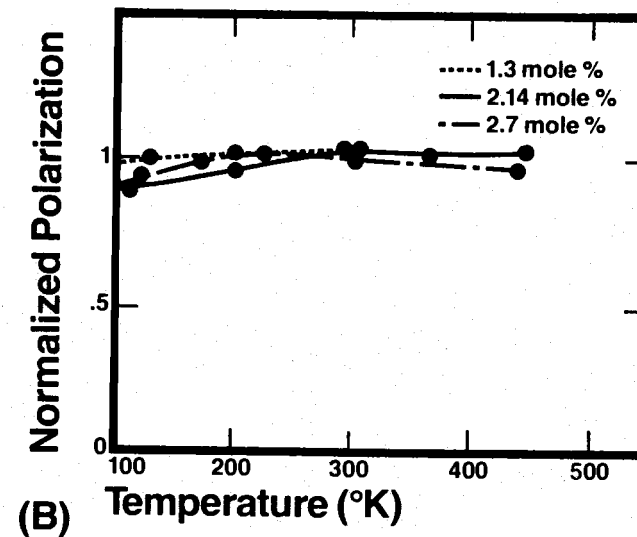
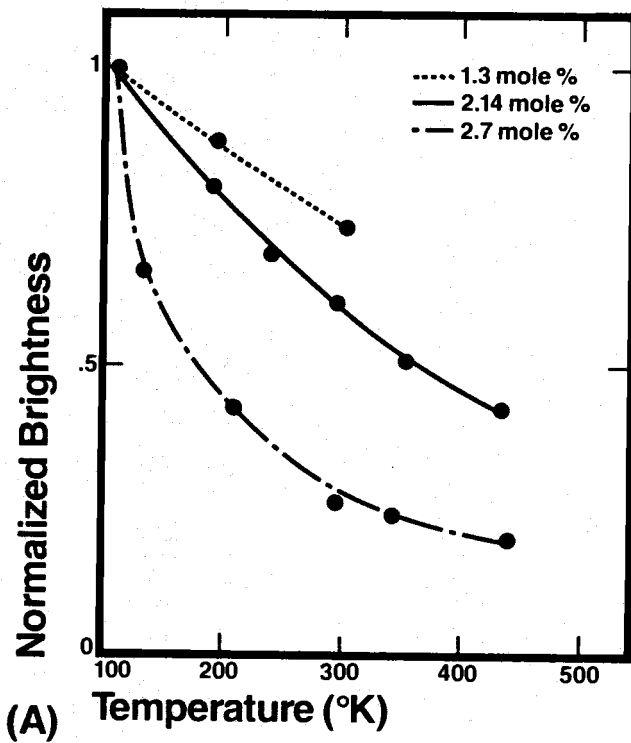


Figure 5.4 (A) and (B). Normalized brightness (A) and polarization (B) as a function of temperature. Note the relative insensitivity of the polarization as compared with the brightness as the temperature is varied. The samples with the highest Mn concentration show the widest variation in brightness.

From figure 5.4(b), it is seen that when the device temperature is in excess of 390K, depending on the  $\text{Mn}^{+2}$  concentration, some conducted charge (leakage current) flows even when the excitation voltage is below the threshold level. The origin of this leakage current is most likely due to phonon assisted tunneling [36] of electrons into the conduction band from certain trapping centers.

In figure 5.5, this leakage current induced polarization is plotted as a function of device temperature for three Mn-doping levels. This data was obtained by holding the excitation voltage at a level just below the extinction voltage and varying the temperature. The extinction voltage is the voltage below which the normal electroluminescence of the sample will be turned off from its on state. The data are normalized to the saturation polarization, i.e., when the driving voltage is 10 percent above the threshold level, at room temperature. It is seen that the on-set of this leakage current occurs at a higher temperature for samples with a higher  $\text{Mn}^{+2}$  concentration. This may be attributed to the observation that the density of deep levels within the ZnS layer increases as more  $\text{Mn}^{+2}$  ions are incorporated into it, those deep levels will likely to cause fewer shallow states to be filled with electrons and therefore result in the situation shown in figure 5.5. A weak electroluminescence was observed to be associated with this leakage current.

### 5.5.3 Variations of Radiation Decay Time with Temperature

The electroluminescent radiation decay of  $\text{Mn}^{+2}$  doped ZnS ACTFEL devices is a complicated process and does not follow the simple

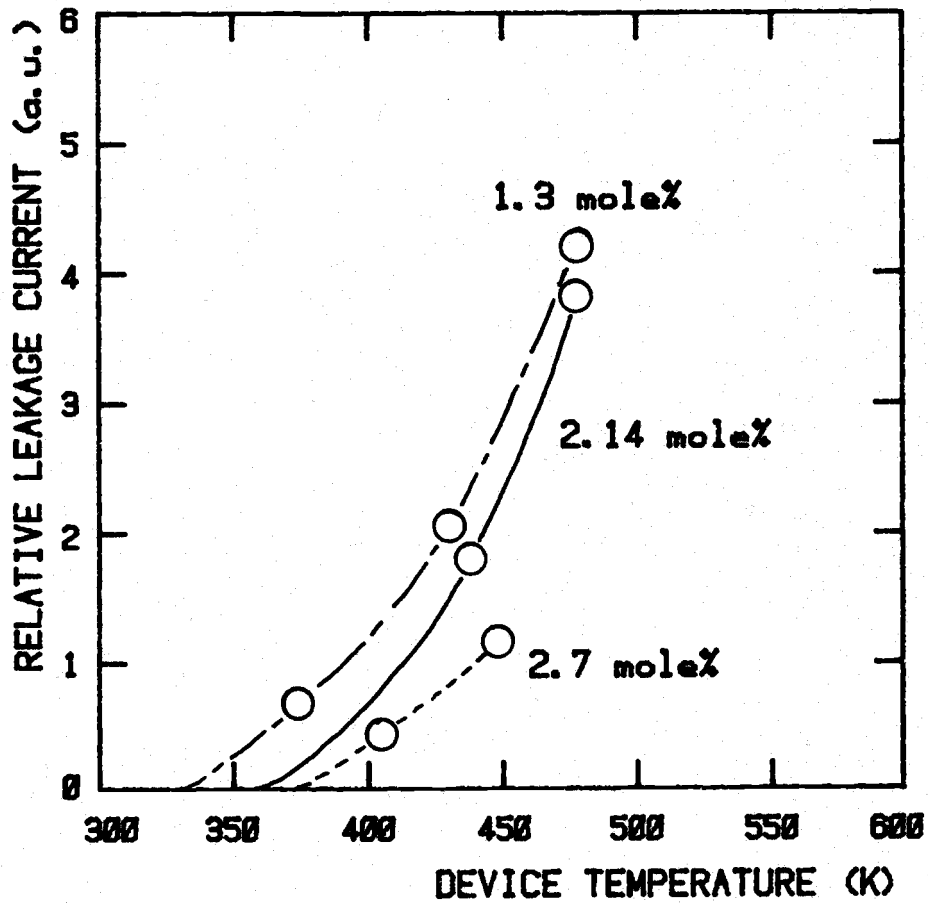


Figure 5.5 Relative "leakage current" as a function of temperature. Note that the more lightly doped samples show the most leakage current.

exponential relationship that is characteristic of a fixed time-constant single-decay phenomenon. In figure 5.6(a), (b), and (c), the normalized light intensity is plotted logarithmically against time for three samples at various temperatures. Note that there is a considerable deviation from the single exponential curve in the initial decay below 100  $\mu$ s. This fast decaying curved section of each plot is characteristic of a multiple exponential process in the initial stage of the light pulse. This nonexponential behavior is most pronounced for the more heavily doped samples, which also show a larger variation in decay time with temperature. After the initial rapid decay, a simple exponential is fairly closely followed and this is referred to as the slowest component. The origin of this multiple exponential process is most likely due to environmental differences between various groups of  $Mn^{+2}$  ions in the ZnS layer.

If  $i(t)$  represents the photons emitted from the  $i$ th group of  $Mn^{+2}$  ions in a similar environment, then the observed electroluminescent emission can be described by

$$L(t) = \sum_i L_i(t) = \sum_i \frac{N_i(t)}{\tau_{ir}} = \sum_i \frac{N_i(0)}{\tau_{ir}} \exp(-t/\tau_i) \quad (5.1)$$

where  $N_i(0)$  is the number of excited  $Mn^{+2}$  ions in the  $i$ th group at  $t = 0$ ,  $\tau_i$  is the observed radiation decay time for the  $i$ th group of  $Mn^{+2}$  ions and is given by

$$\frac{1}{\tau_i} = \frac{1}{\tau_{ir}} + \frac{1}{\tau_{inr}} \quad (5.2)$$

where  $\tau_{ir}$  is the internal radiative decay time, and  $\tau_{inr}$  is the internal non-radiative decay time. Generally  $\tau_{ir}$  is independent

of temperature and  $\tau_{\text{inr}}$  is not.

The major nonradiative decay process for an excited  $\text{Mn}^{+2}$  ion is most likely due to resonant energy transfer to "killer" centers in the ZnS lattice [49]. These centers may be associated with impurity atoms (e.g., Fe, Co, and  $\text{N}_i$  which are known to be efficient killers) [45], or the centers may be associated with defects in the ZnS lattice (e.g., vacancies, dislocations, or grain boundaries). Other possibilities also exist.  $\text{Mn}^{+2}$  ions located near killer centers will be more likely to decay by this mode, which will result in a shorter  $\tau_{\text{inr}}$  for these sites. This process is expected to show a weak dependence on temperature.

At high  $\text{Mn}^{+2}$  concentrations, these nonradiative processes can become more efficient due to the rapid migration of excitation energy from site to site by resonance transfer between  $\text{Mn}^{+2}$  atoms. The rapid migration is a result of the decreasing average distance between  $\text{Mn}^{+2}$  ions, since the dominant resonance transfer mechanism, the electric dipole-dipole interaction, decreases at a rate proportional to  $(R)^{-6}$  where  $R$  is the distance between interacting atoms [54]. Due to the Stoke Shift between the ground state and the excited state of a  $\text{Mn}^{+2}$  ion, this process is thermally assisted and is expected to be more pronounced at high temperatures. The process is best envisioned as a random walk or diffusion process, with the killer centers acting as sinks for the excitation energy. This "concentration quenching" of Mn luminescence will, therefore, be strongly dependent on temperature and also on the site at which the initial excitation occurs.

Figure 5.7 summarizes all of the possible decay channels. The effect

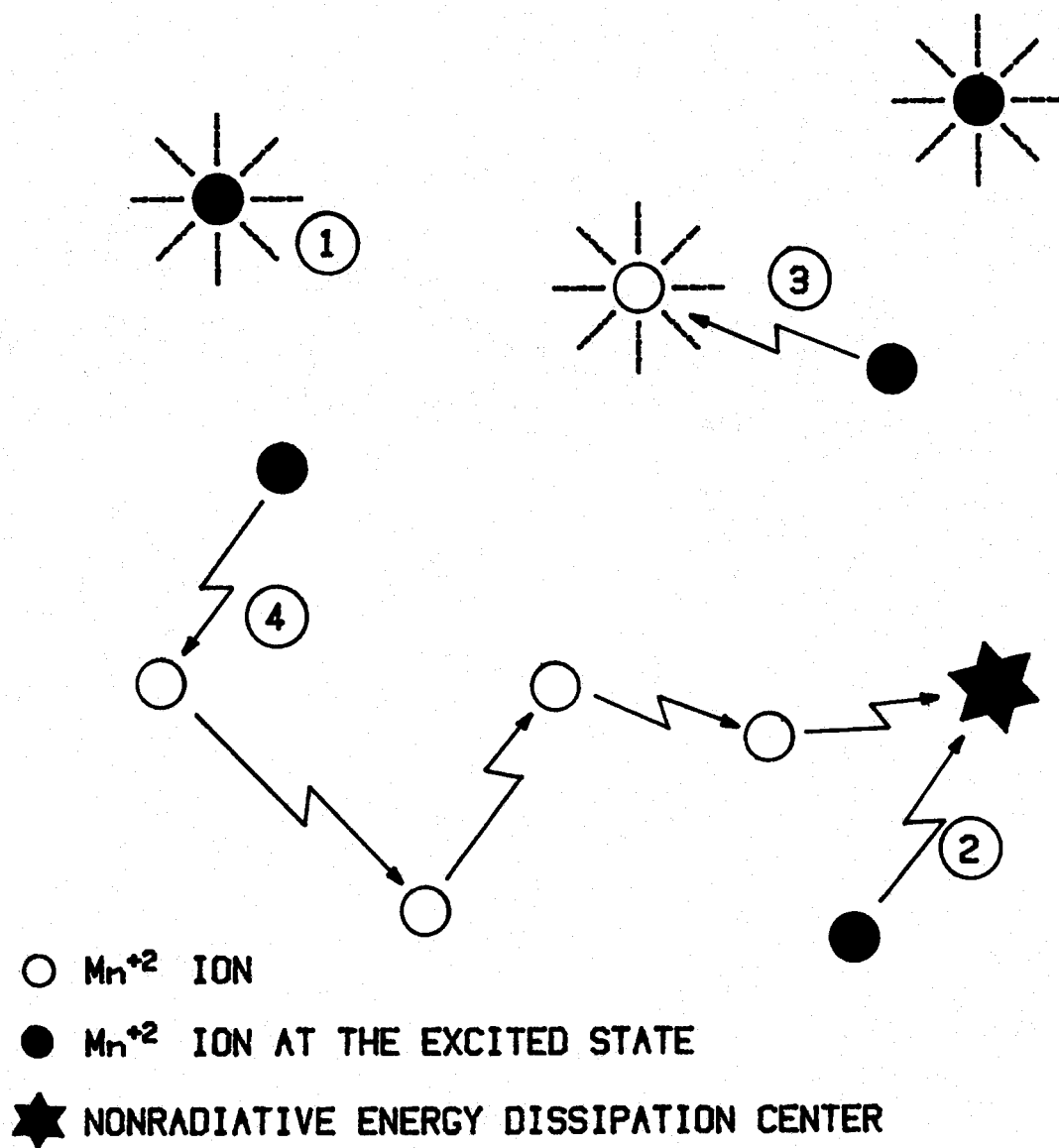


Figure 5.6 Possible channels for a  $Mn^{+2}$  ion to dissipate its excitation energy.



of concentration dependence of non-radiative decay processes is also seen in the photoacoustic measurement of ZnS:Mn phosphors [51].

In addition to these site-selective variations in the non-radiative decay time  $\tau_{\text{inr}}$ , there are also variations in the radiative decay times  $\tau_{\text{inr}}$  due to variations in the local environment for the  $\text{Mn}^{+2}$  ions. For example, the existence of  $\text{Mn}^{+2}\text{-Mn}^{+2}$  pairs in cubic ZnS lattice had been verified via optical spectra analysis by McClure [14] and it is known that the radiative decay time for the pairs is many times faster than that of a Mn at an isolated site [24], [52]. McClure [14] has suggested that the shortening of  $\text{Mn}^{+2}\text{-Mn}^{+2}$  pair decay time is because of the availability of a new transition mechanism for the pairs which is not effective for the single ions, i.e., the relaxed selection rule, which forbid the  ${}^4\text{T}_1$  to  ${}^6\text{A}_1$  transition in a single  $\text{Mn}^{+2}$  ion, due to the exchange interaction between the  $\text{Mn}^{+2}$  pairs. Another reason for  $\text{Mn}^{+2}$  ions to have different  $\tau_{\text{ir}}$  is due to their locations on non-equivalent lattice sites. Busse et. al. [53] have used site selected laser spectroscopy to analyze the polymorphic properties of ZnS:Mn crystals. Their data showed that the luminescence decay times for  $\text{Mn}^{+2}$  ions at different sites have very different values, for example, the decay time for  $\text{Mn}^{+2}$  on a cubic site is 1.77 millisecond while that on a hexagonal site is only 1.15 millisecond. Since this thin film material is known to have a high density of defects, it is therefore expected that such site-to-site variations will occur.

From the above considerations, one expects that the  $\text{Mn}^{+2}$  decay in the ZnS:Mn ACTFEL devices will show a slower exponential component

due to the decay of relatively isolated ions and a faster initial component due to the decay of additional non-isolated ions. A faster decay time for samples with a higher Mn concentration is also expected because of the migration of excitation from  $\text{Mn}^{+2}$  to  $\text{Mn}^{+2}$  and subsequent dissipation at energy sinks. This latter component will also show a strong temperature dependence.

These expectations are indeed born out by experimental results as shown in figure 5.7(a), (b), and (c). The very lightly doped sample, shown in figure 5.7(c), shows negligible temperature dependence of the decay time, yet a small non-exponential initial decay is observed, indicating that although the concentration and temperature dependent nonradiative decay channel was hampered by the large interionic distances, the site selective variations in decay time still exist. The data for the more heavily doped samples shown in figure 5.7(a) and (b), however, show the stronger temperature dependence associated with concentration quenching. The data also indicated a progressive decrease of electroluminescent radiation decay time as the  $\text{Mn}^{+2}$  concentration increases.

#### 5.3.4 Excitation Efficiency of $\text{Mn}^{+2}$ Ions

The linear plot of electroluminescent light output against time for various device temperatures is shown in figure 5.8. The data shown is for the sample having a  $\text{Mn}^{+2}$  concentration of 2.7 mole %. Similar data was also obtained for other doping levels. The driving voltage for figure 5.8 was held constant throughout the measurement with its amplitude at the saturation level, see figure 3.9.

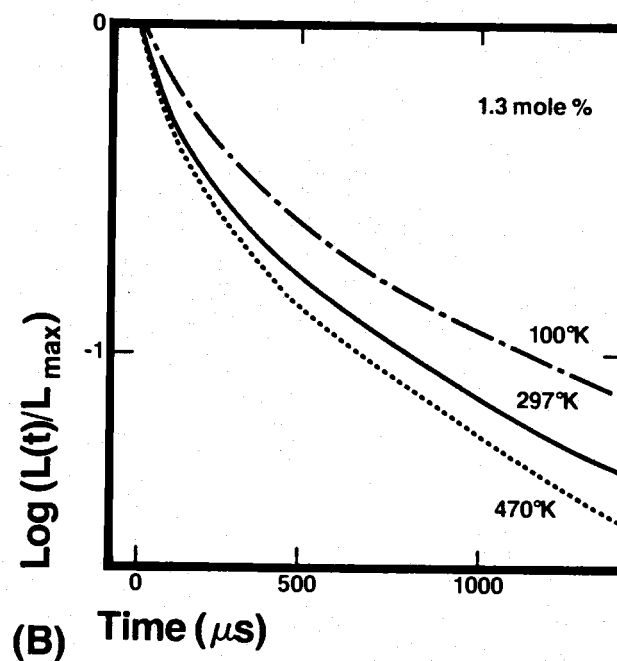
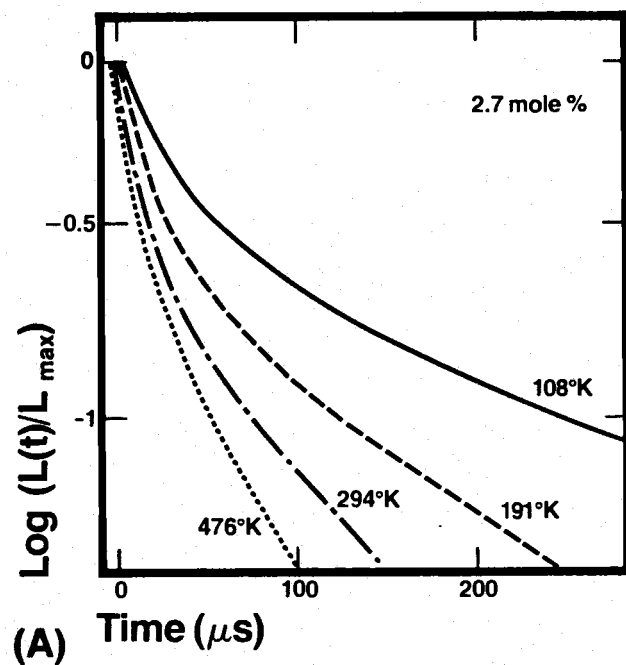


Figure 5.7 (A), (B), and (C). Normalized plots of light output versus time following the voltage pulse. The larger decay times at low temperature are probably due to the "freezing out" of thermally induced nonradiative processes. This effect is discussed in the text.

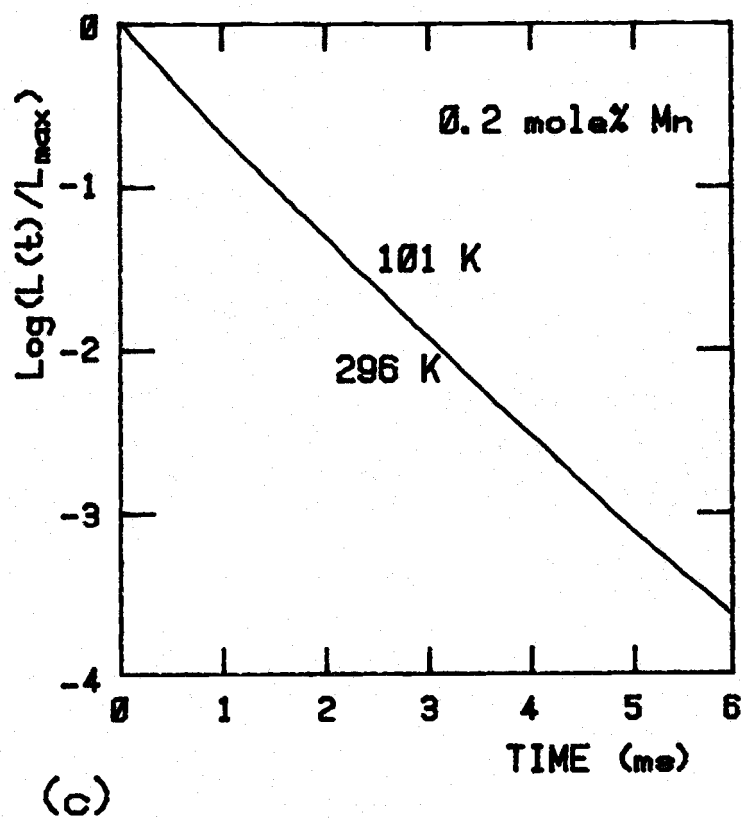


Figure 5.7 (C) See the previous page for figure caption.

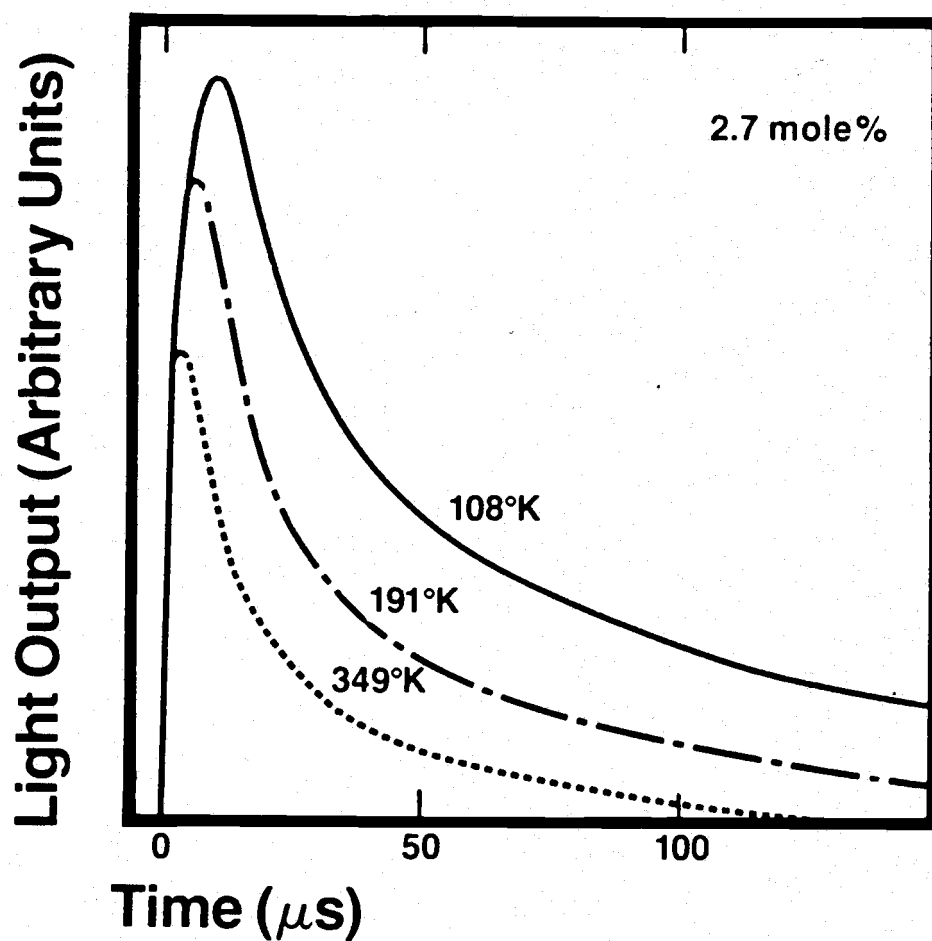


Figure 5.8 Light output versus time, with temperature as a parameter. The vertical axis is linear. Note the increase in decay time and also the increase of the initial peak light output as the temperature is decreased. The driving voltage was held constant for the measurement.

In addition to increased radiation decay time at low temperatures, there is a significant increase in the initial light output. From the earlier discussion, the initial light output is given by

$$I(t)/t = 0 \quad N_i(0)/\tau_{ir} \quad (5.3)$$

Since the internal radiative decay time  $\tau_{ir}$  of an excited atom of ion is usually independent of temperature, a higher initial peak of the light pulse implies that more  $Mn^{+2}$  ions were excited at time  $t = 0$ . This enhancement of the initial light output cannot be attributed to an increase in power delivered to the device, because

- (i) the driving voltage was held constant,
- (ii) the device electroluminescence threshold voltage didn't change significantly below room temperatures, and
- (iii) the amount of conducted charge, reflected in the polarization phenomena of chapter 3, at low temperatures is essentially constant.

Since hot electron impact excitation is still an important process for electroluminescence in the ZnS:Mn ACTFEL devices, regardless of which of the controversial mechanisms is the dominant excitation process, a minimum threshold kinetic energy is required in order for an electron to excite electroluminescence. At elevated temperatures, phonon scattering slows down electrons, and as the temperature increases, fewer electrons reach the minimum energy requirement. For lower temperatures, phonon scattering is reduced and electrons are then able to travel a longer scatter-free distance under the biasing field, which results in increased kinetic energy. Hence, more electrons exceed the minimum excitation energy requirement.

Essentially, this means that the hot-electron energy distribution at lower temperatures is more favorable for the impact excitation process. Figure 5.9 outlines the essence of the above phenomena.

The average brightness of a ZnS:Mn ACTFEL device increases as the device temperature is lowered as is shown in figure 5.4(a). The brightness is proportional to the time integral of  $L(t)$ , light intensity, versus time. Therefore, for a certain class of  $Mn^{+2}$  ions, the light emitted is proportional to

$$L_i(t) = (N_i(0)/\tau_{ir}) \exp(-t/\tau_i) \quad (5.4)$$

and the brightness is proportional to  $N_i(0)(\tau_i)/(\tau_{ir})$ .

Since the internal radiative decay time  $\tau_{ir}$  is usually independent of temperature, thus the increased brightness is due to the increase of  $N_i(0) \tau_i$ . It has been shown that actually both  $N_i(0)$  and  $\tau_i$  increase at low temperatures. The brightness enhancement at low temperatures therefore resulted from the combined effects of,

- (i) freezing out of the nonradiative decay channels due to the lack of phonons available to help overcome the energy barrier for these processes, and
- (ii) improvement of the  $Mn^{+2}$  ions excitation efficiency as the hot-electron energy distribution shifts toward a higher level.

### 5.3.5 Hysteresis Variation with Temperature

The temperature dependence of device hysteresis for three different  $Mn^{+2}$  concentrations is shown in figure 5.10. The hysteresis width changes very little until the device temperature is raised to a

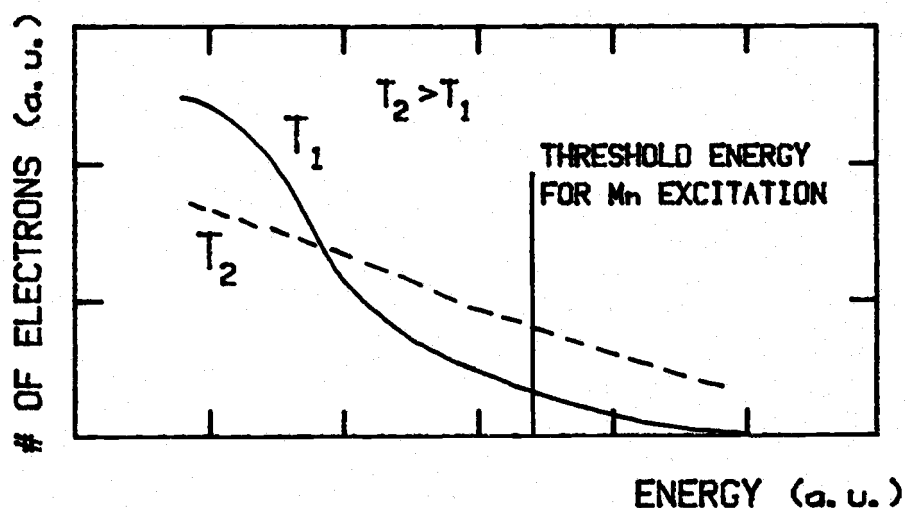


Figure 5.9 Hot electron energy distribution at two different device temperatures.

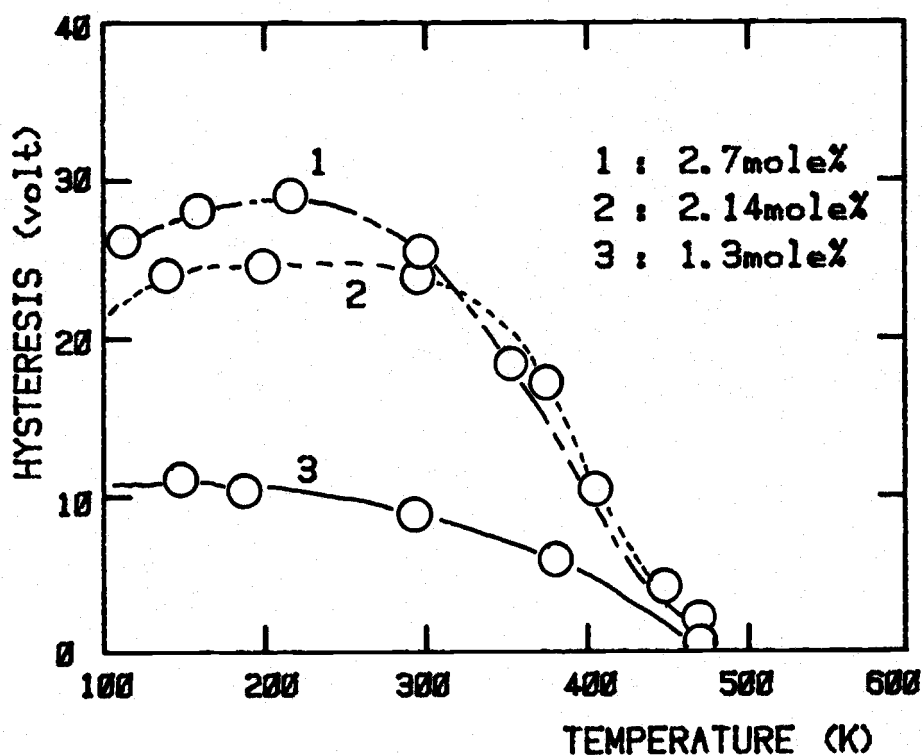


Figure 5.10 Hysteresis width versus temperature for the three samples. Hysteresis was not observed above 500°K for any of the samples.



level where leakage effects are evident. Above this temperature, the hysteresis width decreases.

As previously reported, the hysteresis width below 350K is determined mainly by the Mn concentration [4]. Above this temperature, the hysteresis width decreases. No hysteresis was observed above 500K in any of the samples. This reduced hysteresis width coincides with the onset of leakage current. The disappearance of hysteresis at about 500K regardless of film thickness or Mn concentration, suggests that certain physical processes, either intrinsic to the ZnS host material or associated with the insulators, are responsible. Studies of the residual field induced charge measurement indicates that both processes could have been responsible.

At low temperatures, the turn-on edge of the B-V hysteresis loop becomes steeper, and at sufficiently low temperatures, it becomes essentially vertical. This phenomena may be attributed to thermal coupling between adjacent conduction filaments [30] without quenching of the original ones.

#### 5.4 Summary

In summary, the study of temperature effects on ZnS:Mn ACTFEL devices leads to the following conclusions:

- (i) Tunneling is the dominant process for initial carrier generation in these devices, because the electrical characteristics are largely independent of temperature. Therefore, the Frenkel Poole effect, or other thermally induced effects, are not important for device operation below 390K.

- (ii) Phonon-Assisted nonradiative decay is related to  $\text{Mn}^{+2}$  concentration. The increase in radiative decay time  $\tau_i$  indicates that some phonon-assisted non-radiative decay channels are frozen out at low temperatures. This effect is especially pronounced for heavily doped samples. These non-radiative decay processes are probably due to phonon-assisted resonant-energy transfer between  $\text{Mn}^{+2}$  centers. This effect is known from studies of concentration quenching in other systems [49].
- (iii) The increase in initial light output and the unchanged amount of conducted charges implies an improved  $\text{Mn}^{+2}$  excitation efficiency at low temperatures. The fundamental assumption that supports this conclusion is that the internal radiative decay time does not decrease at low temperatures. Since the transition involved in electroluminescence occurs within the  $3d^5$  configuration of the  $\text{Mn}^{+2}$  ion, this assumption is probably correct.
- (iv) Disappearance of hysteresis above 500K, regardless of film thickness and the  $\text{Mn}^{+2}$  doping level, implies that some physical processes either intrinsic to the ZnS host material or associated with insulator properties are responsible.

## THERMALLY RELEASED AND RESIDUAL FIELD INDUCED CHARGE MEASUREMENT

6.1 Introduction

Accurate electrical measurement in characterizing the deep level distribution in insulating materials is difficult. The most widely used technique for this purpose has been the thermally stimulated current (TSC) measurement [55], [56]. However direct application of this method to study the trap distribution within thin insulating films, is further complicated by the small total number of trap states due to the small volumes involved. Two new experimental techniques, which are based on the theoretical analysis of the deep level transient spectroscopy experiment (DLTS) [57], [58], were developed to resolve specifically the difficulties encountered in the TSC measurement. These new techniques, called the windowed thermally released charge (WTRC) measurement and the residual field induced charge (RFIC) measurement, take advantage of readily available single board microcomputer systems to perform automatically the complicated iterative data taking procedures. The WTRC measurement was directed to detail the trap structure of the insulator layers, whilst the RFIC measurement was intended to acquire a general survey of deep levels within the ZnS:Mn active film of the ACTFEL devices.

The experimental results indicate that there are deep traps within both the ZnS and the insulator films, the trap concentration of the ZnS films was found to be a function of both the  $\text{Mn}^{+2}$  doping

level and the aging of the sample. The detailed experimental procedures and data analysis follow.

## 6.2 The Thermally Released Charge Measurement

The sample used in this experiment has a special structure which consisted all of the standard features of an ACTFEL device except with the ZnS layer removed. The cross-sectional view of the special sample is shown in figure 6.1, where a double layer of  $\text{Al}_2\text{O}_3/\text{Y}_2\text{O}_3$  was chosen as the insulator materials. Because of the similarity, and approximately the same energy band gap of about 9eV [59], [60], of these oxide insulators, there are only small discontinuities between the conduction bands and the valence bands at the interfaces. Therefore, the insulator film can be thought of as if it were made of a single layer of mixed material without losing the generality for later discussions. Based on this assumption, the energy band diagram along with some possible trap distributions of the sample when under an external biasing voltage is shown in figure 6.2.

The schematic diagram of the system is illustrated in figure 6.3, and the measurement procedures as well as the underlying physical reasons are now discussed.

With the biasing voltage at zero, the sample was first illuminated with a Xenon light source to populate some of the trap states within the insulator film. The traps that were filled by this process are most likely to be electron traps. This is because of the extremely wide band gap of the insulators, it is not possible for the Xenon

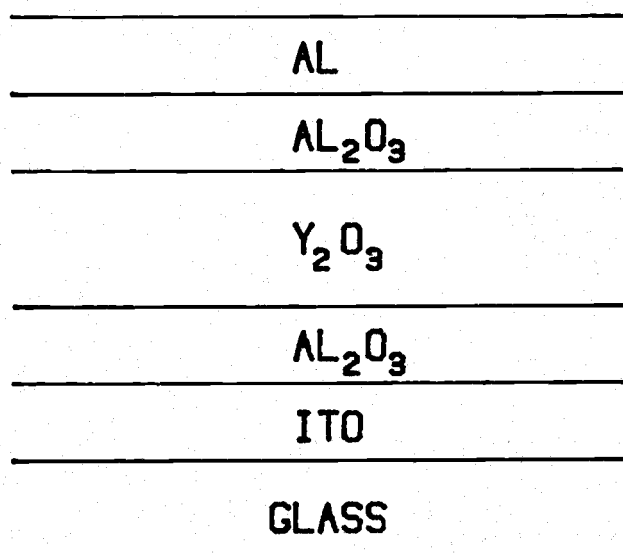


Figure 6.1 The crosssectional view of the special sample used to study the insulator trap states.

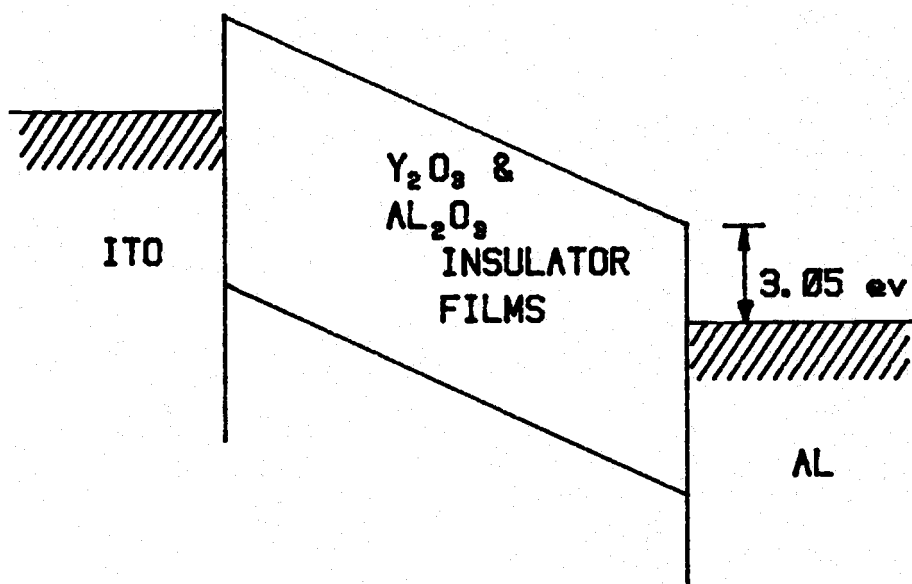


Figure 6.2 The band diagram of the special sample when first subjected to an external biasing voltage.

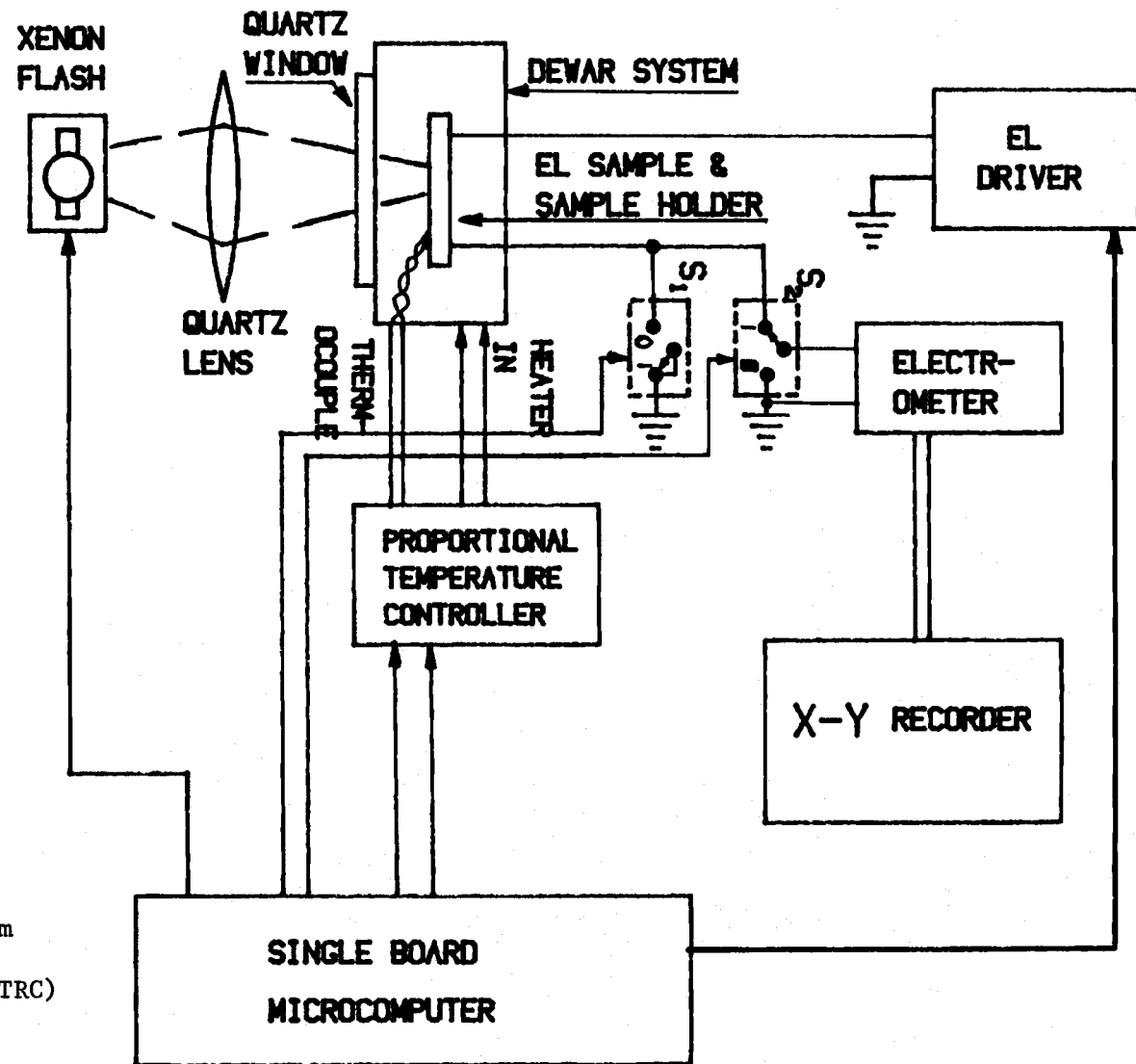


Figure 6.3 The system diagram of the thermally released charge (TRC) measurement.

light to create electron-hole pairs within the insulator film, therefore the trap filling process was probably accomplished by photoemission of free electrons from the two electrodes into the conduction band of the insulator layer, and a resultant trapping by the deep levels. The photon energy required to excite an electron from the Al electrode into the  $\text{Al}_2\text{O}_3$  layer is only a little more than 3eV [61], [62], which easily passes through the device and reaches the Al- $\text{Al}_2\text{O}_3$  interface.

Following the filling process, the trap levels began to approach thermal equilibrium with the conduction band of the insulators. The trapped electrons are released into the conduction band at an emission rate given by [63]

$$e_n = \sigma_n V_T N_C \exp[-(E_C - E_T)/kT] \quad (6.1)$$

Where  $E_C$  and  $E_T$  are the energy levels of the conduction band and the trap states respectively,  $\sigma_n$  is the electron capture cross section,  $V_T$  is the thermal velocity and  $N_C$  is the density of states of the conduction band. Both  $V_T$  and  $N_C$  here are temperature dependent, namely  $V_T \propto T^{1/2}$  and  $N_C \propto T^{3/2}$ , therefore the trap energy level as measured from the conduction band minimum,  $E_T - E_C$ , can be obtained from the slope of the Arrhenium plot, i.e., the  $e_n/T^2$  versus  $1/T$  plot where  $T$  is the device temperature in degree Kelvin. To measure the amount of the thermally released electrons, a low d.c. biasing voltage, was applied to the device immediately after the trap filling process to collect the thermally emitted electrons. This voltage is deliberately kept below that which would cause tunneling. In the external circuit, a transient current occurs which is given by

$$I(t) \propto [N_T(0) - N_T(\infty)] e_n \exp(-e_n t) \quad (6.2)$$

where  $N_T(0)$  is the initial total number of filled trap levels, and  $N_T(\infty)$  is the filled trap levels at thermal equilibrium.

The windowed thermally released charge signal (WTRC signal) was then obtained by integrating all the outcoming electrons from time  $t_1$  to  $t_2$  after the application of the biasing voltage, i.e.

$$\begin{aligned} \text{WTRC} &= \int_{t_1}^{t_2} I(t) dt \\ &= \xi [N_T(0) - N_T(\infty)] [\exp(-e_n t_1) - \exp(-e_n t_2)] \end{aligned} \quad (6.3)$$

where  $\xi$  is a proportion constant. The above measurement procedures were repeated as the device temperature was slowly heated. The measurements were controlled by a single-board microcomputer. To summarize the procedures, figure 6.4 shows the timing diagram of all the control units shown in the system diagram, figure 6.3.

The physical meaning of this WTRC signal is illustrated in figure 6.5 as the cross hatched areas under each transient current curve which corresponds to various device temperatures. It is seen that for a fixed choice of  $t_1$  and  $t_2$ , this WTRC signal will go through a local maximum at a certain temperature. Following the DLTS analysis, when this local maximum occurs, the corresponding trap emission rate  $e_n(T_{\max})$  can be obtained by differentiating equation (6.3) with respect to temperature and setting this equal to zero, i.e.

$$\left. \frac{\partial(\text{WTRC})}{\partial T} \right|_{T_{\max}} = 0 = e_n(T_{\max}) = \text{Ln}(t_2/t_1)/(t_2 - t_1) \quad (6.4)$$

This equation is the necessary condition for a local maximum to occur. Because the emission rate is strongly temperature dependent, it is possible for equation (6.4) to be satisfied by certain trap



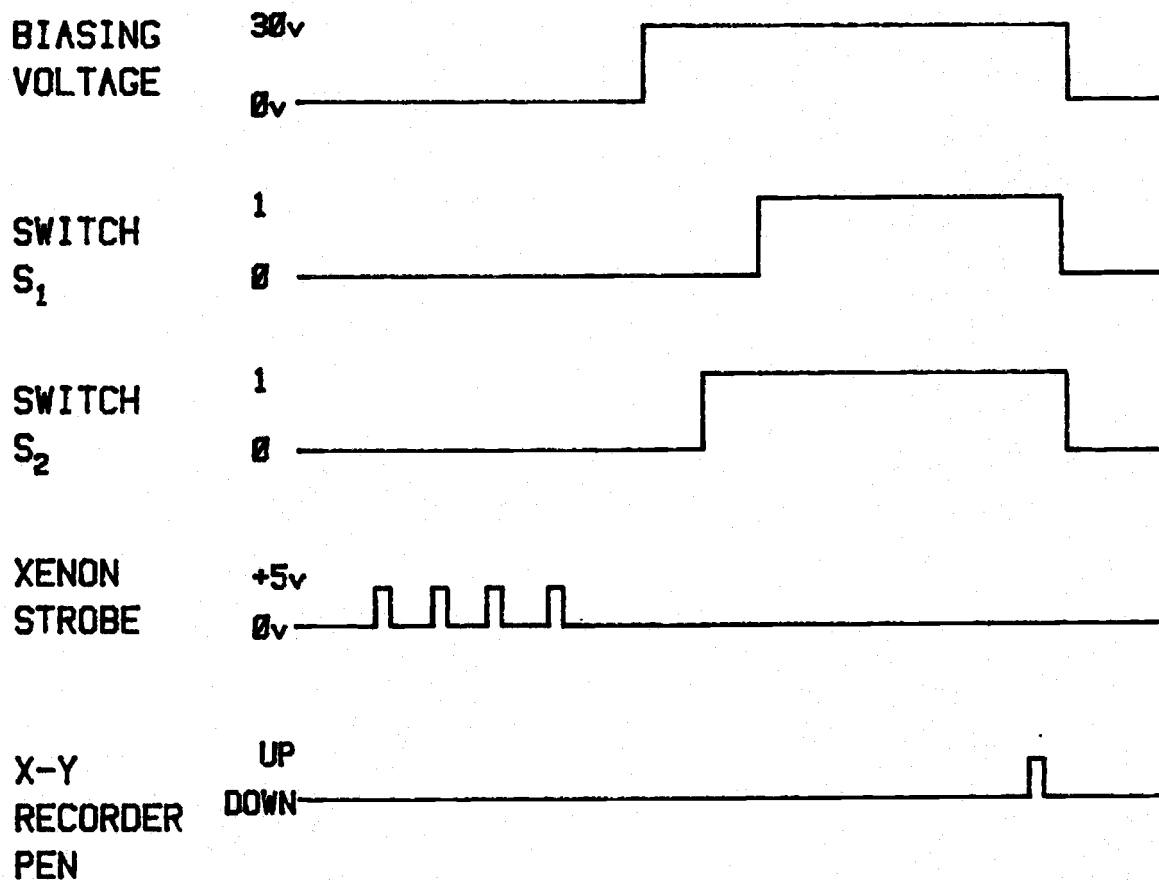


Figure 6.4 The timing diagram of the control signals for the WTRC measurement. Refer to figure 6.3 for the function of switch  $S_1$  and  $S_2$ .

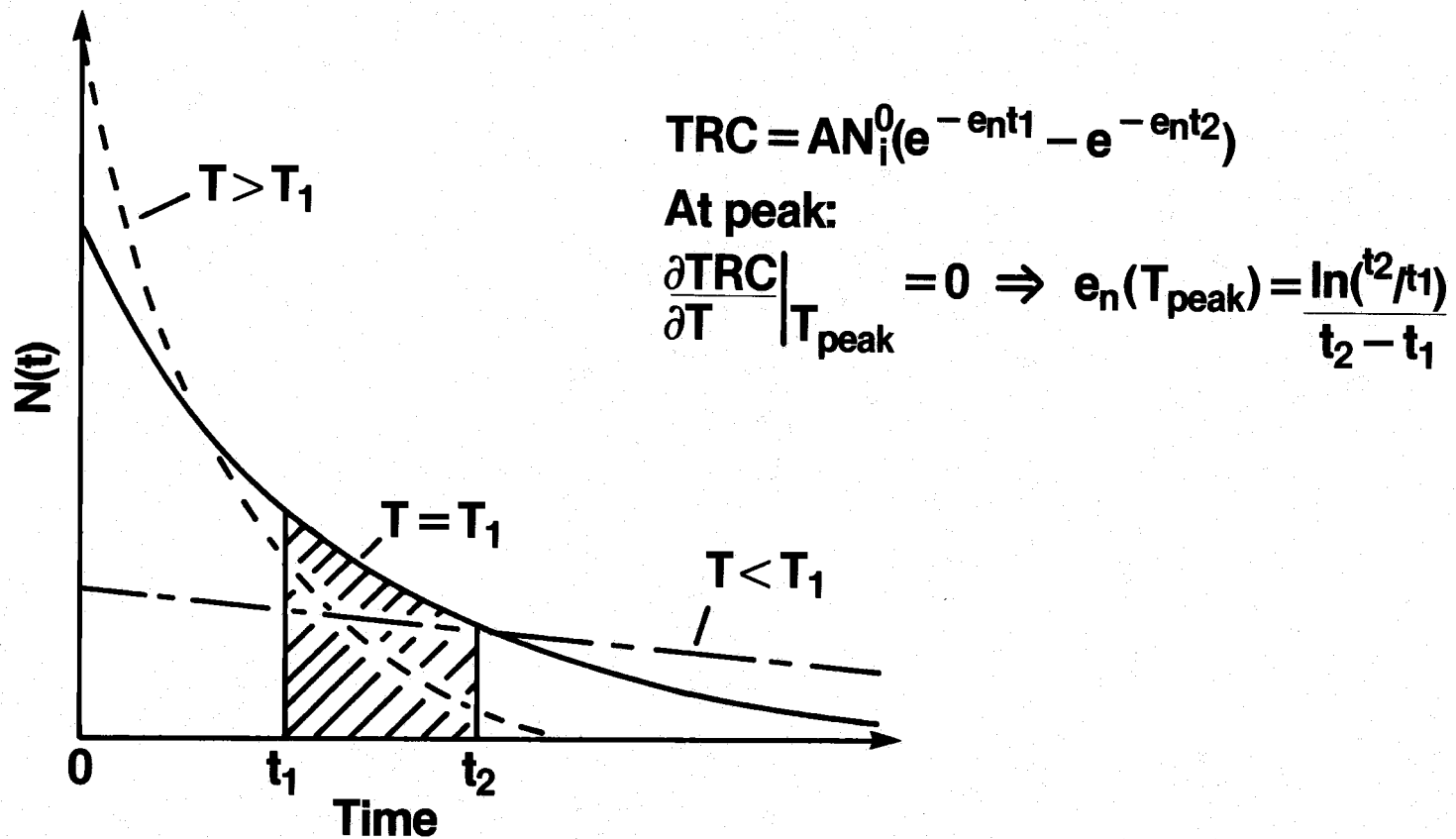


Figure 6.5 The transient current at various device temperatures. The WTRC signal is related to the area enclosed by  $t_1$ ,  $t_2$ , and the corresponding transient current curve as is illustrated above by the cross-hatched area for temperature  $T_1$ .

levels at different temperatures, via different choices of  $t_1$  and  $t_2$ . One therefore can locate points on the Arrhenius plot from a number of temperature scans under different integration time  $t_1$  and  $t_2$ , and obtain information about the trap energy level.

The experimental result of the WTRC signal for the special sample is shown in figure 6.6. The curves here correspond to different setting of  $t_1$  and  $t_2$ . On each curve, there appears to be a local maximum at a very low device temperature, therefore only its falling tail was registered. As the temperature increases, a central local maximum emerged at around 300K which was followed by a diverging trend as the temperature increases above 400K. Due to the temperature and timing ranges involved, only the trap levels corresponding to the central maximum are fully analyzed here. However, the onset of the diverging trend of the WTRC signal above 400K, appears to be coincident with the increased rate of the reduction of device hysteresis width at elevated temperatures, which was discussed in chapter 5. As for the peak which occurs at a very low temperature, other measurement revealed that it was induced by a group of trap levels other than those causing the center maximum, however their density is very small which should have only a minor effect on the device performance.

The Arrhenius plot for the central local maximum, for the above experimental data, is shown in figure 6.7. The slope of this plot indicates that the corresponding trap states, have an apparent energy level of about 0.79 eV below the bottom of the conduction band of the insulators. After appropriate adjustments to correct for the biasing voltage induced Frenkel-Poole barrier height lowering effect

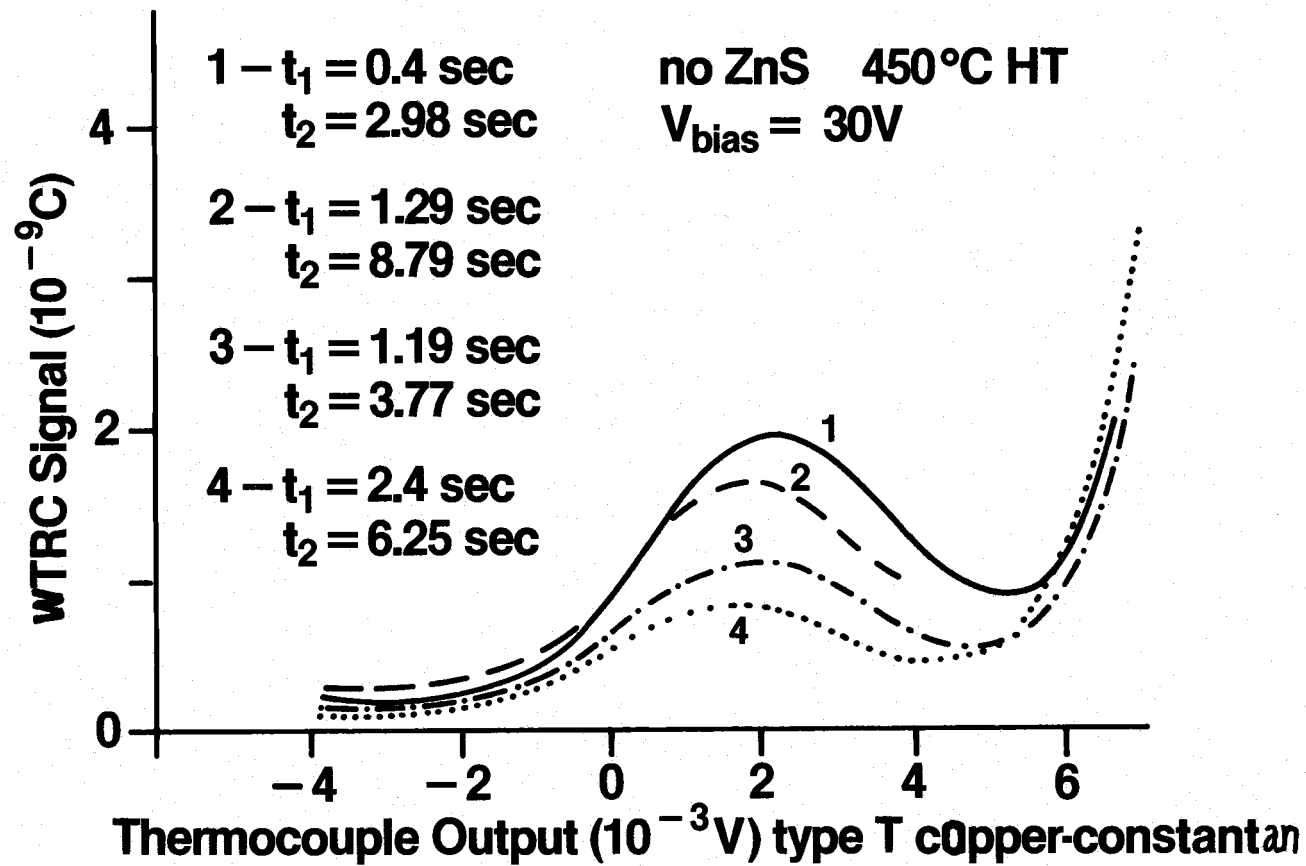


Figure 6.6 The WTRC signal plotted against device temperature. Each curve corresponds to a different choice of the integration interval  $t_1$  and  $t_2$ .

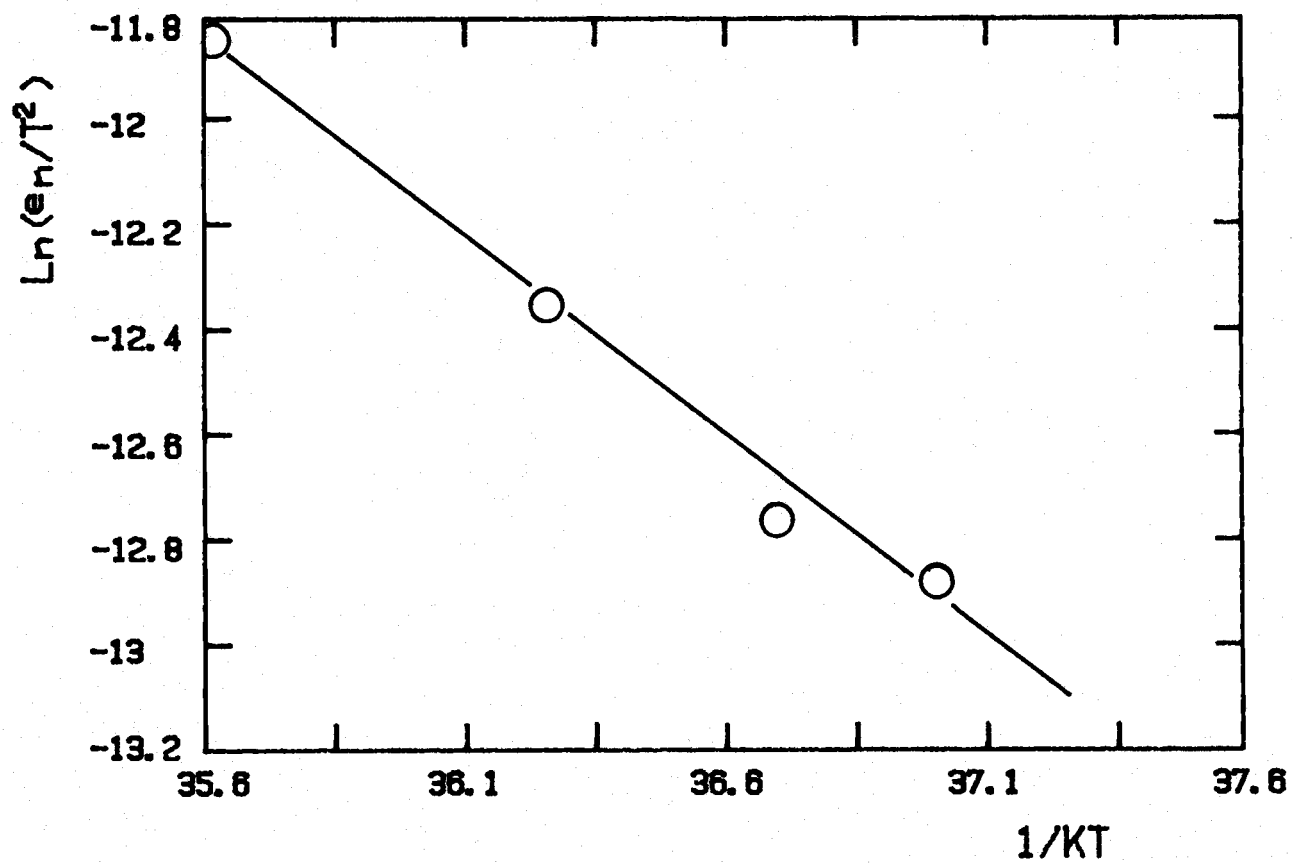


Figure 6.7 The Arrhenius plot of the WTRC data shown in figure 6.6. The slope corresponds to a trap level of 0.79 eV below the conduction band edge.

[64], figure 6.8, the actual trap depth with zero biasing electric field, was found to be about 0.9 eV.

Since the half widths of the WTRC curves in figure 6.6 are quite broad when compared to the similar DLTS type signal for trap levels in semi-insulating single crystal materials [65], one therefore speculates that instead of having a sharply defined energy level as for the single crystal case, these insulator trap states here have their energy spectra spread over a certain finite energy range. This assumption seems to be reasonable, because the best quality thin films that can be obtained by electron-beam evaporation are polycrystalline. These are known to exhibit high defects and thus a lot of space inhomogeneities are expected.

Another mechanism which, if exists, can cause confusion of the WTRC signals is known as the mobile ion effect. Ionic instability in insulating films under high temperatures are known to exist [66] and are a source of many problems in integrated circuits. However, analysis of the special sample by the high temperature triangular voltage sweep method [67] failed to indicate any sign of mobile ions within the sample.

### 6.3 The Residual Field Induced Charge Measurement (RFIC)

This experiment was designed to survey the trap states associated with the ZnS layer within the ACTFEL devices. The measuring system is the same as for the WTRC measurement except for changes in the detailed procedures, which are illustrated with the timing diagram of figure 6.9, where the vertical axis indicates the overall charge

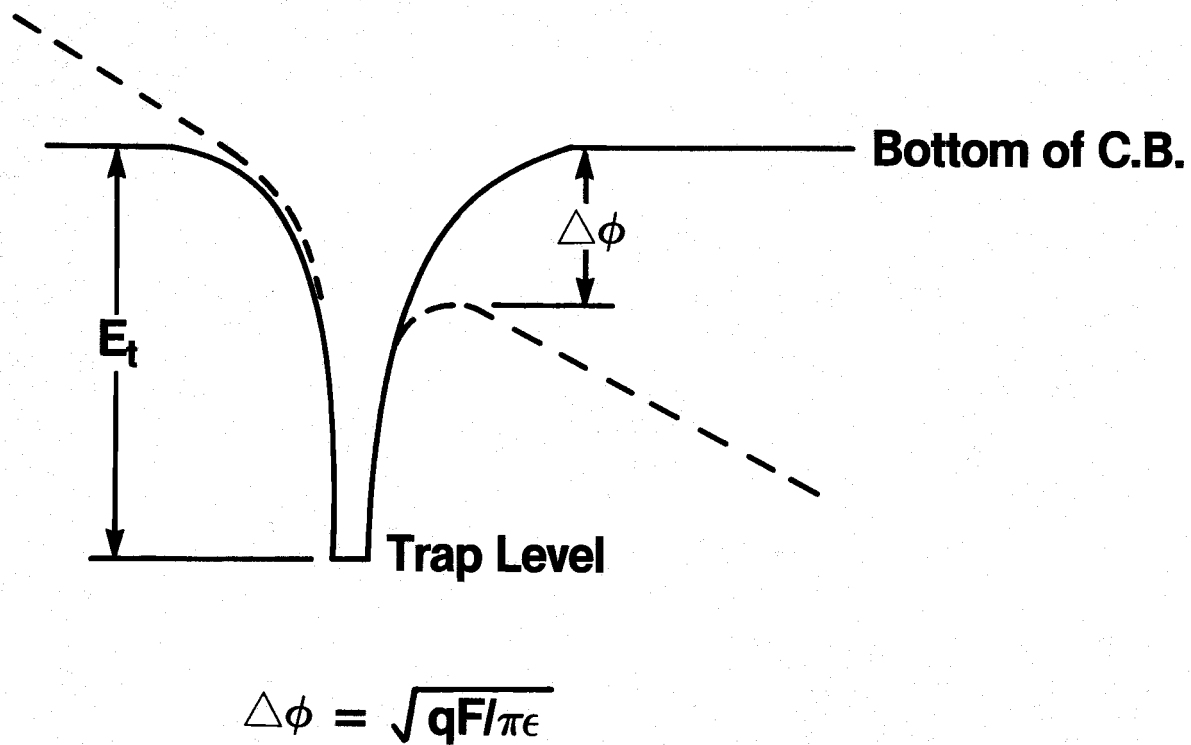


Figure 6.8 The Frenkel-Poole effect. The solid line corresponds to the potential well under no biasing electric field and the dotted line corresponds to the potential well while an external biasing electric field is applied.

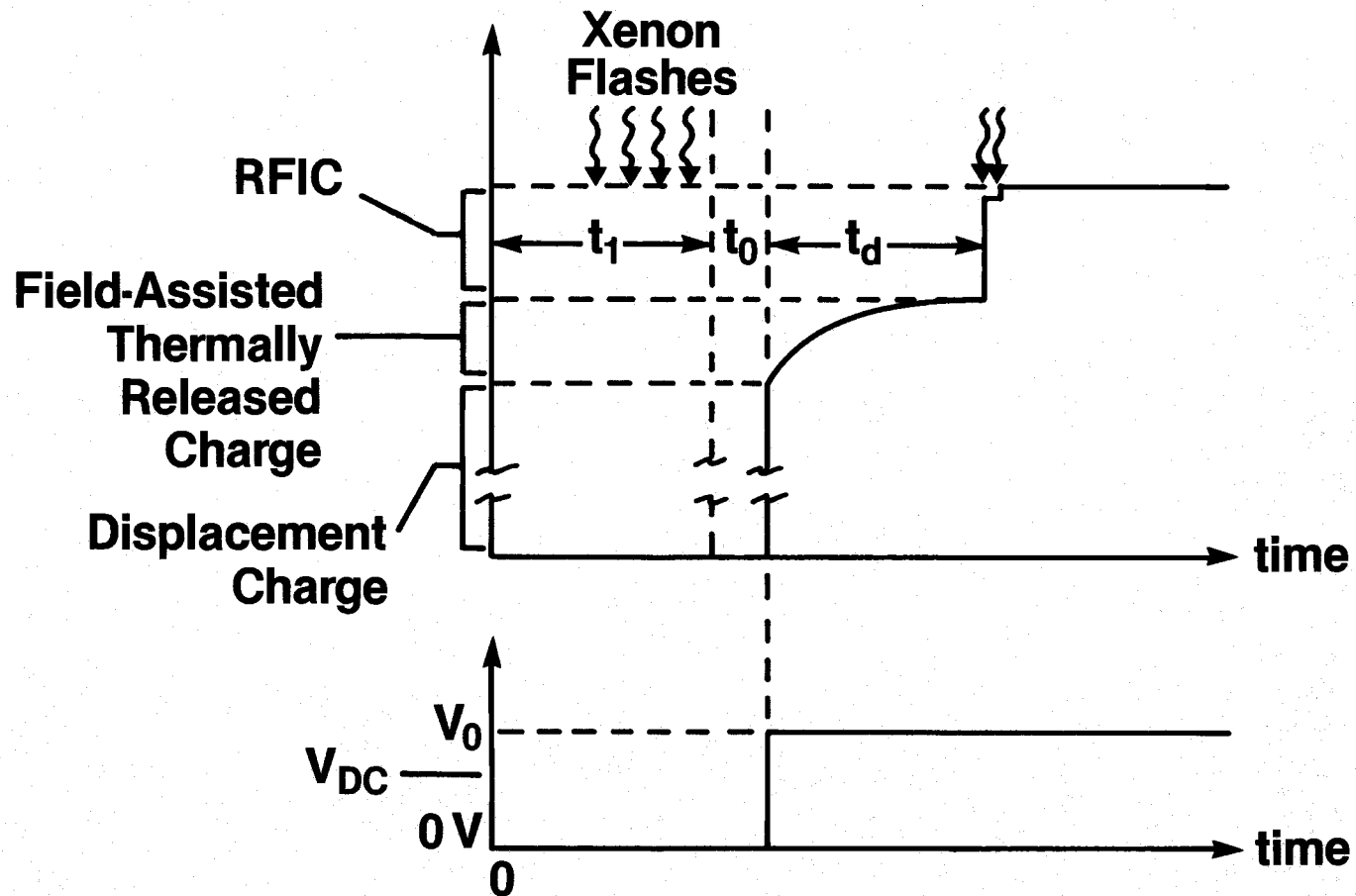


Figure 6.9 The timing diagram of the biasing voltage and the total amount of charge that had flown during the residual field induced charge (RFIC) measurement. Refer to the text for detailed descriptions.



flow within the ACTFEL sample at various steps. The first procedure was to illuminate the sample with a sequence of Xenon flashes whilst the biasing voltage was held at zero volt. The high energy photons which generated electron-hole pairs within the ZnS layer, completely neutralized the residual polarization field of the ZnS and populated some of the trapping centers. After the photo-excitation process, a short delay time  $t_0$  of a few tenth of a second followed in order to stabilize the excitation process. The low d.c. biasing voltage chosen again to cause no tunneling, was then applied which induced some displacement current as shown in the figure. The sample was maintained in this state for several seconds until time  $t_d$ . During this period, those trap states within the ZnS having their carrier emission rate at the corresponding temperature higher than or comparable to  $1/t_d$ , will likely emit the trapped carriers into either the conduction band or the valence band of the ZnS, depending upon which type of traps are involved. Those emitted carriers then drift along the biasing field until they either get retrapped by some other deep levels, or reach the ZnS-insulator interface. No matter which route taken, the result was that a ZnS polarization field had been built up which reduced the effective electric field strength inside the ZnS layer. The amount of this field reduction reflects the total number of trapping centers within the ZnS that have been depopulated. At the end of  $t_d$ , another pair of intense Xenon flashes were applied to the sample. This again turns the ZnS into a conductor which allows additional conduction charge to flow in order to collapse the residual electric field strength to zero. This Xenon

induced additional charge flow is the RFIC signal, which is of course proportional to the strength of the ZnS residual electric field strength at the end of  $t_d$ . This RFIC signal was repeatedly measured with the automated measuring system whilst the sample was slowly heated.

A clearer mathematical model for this RFIC signal is discussed with the help of a simplified schematic diagram shown in figure 6.10. In this figure, the resistance  $R_1$  across the ZnS capacitor symbolizes the conductivity modulation by charge carriers emitted from their trapping centers, and the additional switch S parallel to it represents the situation when the Xenon light shorts out the ZnS film. The maximum RFIC signal that can be obtained is when, during the time period  $t_d$ , none of the trap levels has released its trapped carrier, i.e.,  $R = \infty$ , therefore the signal is given by

$$\text{RFIC}_{\max} = C_i V_B - C_t V_B \quad (6.5)$$

where  $C_i$  is the total insulator capacitance,  $C_t$  is the overall device capacitance, and  $V_B$  is the low d.c. biasing voltage. The device capacitance  $C_t$  is, of course, given by

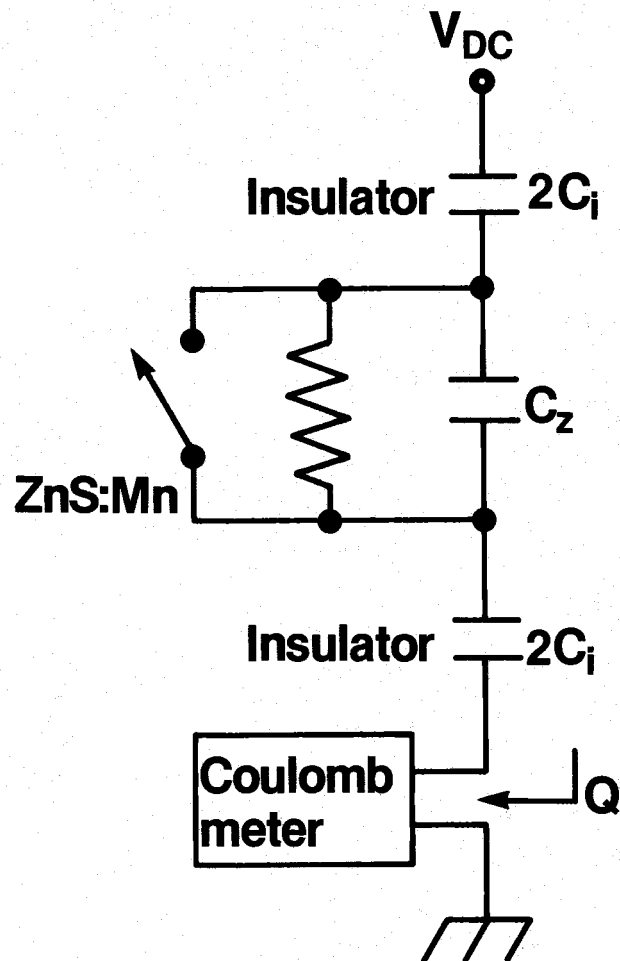
$$C_t^{-1} = C_i^{-1} + C_z^{-1} \quad (6.6)$$

and  $C_z$  is the capacitance of the ZnS film.

At moderate device temperatures, some trap states will be depopulated, i.e.  $R \neq \infty$ , the RFIC signal is then

$$\text{RFIC}(T) = \text{RFIC}_{\max} - \alpha N_T(0) [1 - \exp(-e_T(T)t_d)] \quad (6.7)$$

where  $\alpha$  is a constant which takes into account the electronic charge, the relative capacitances between the ZnS and the insulator layers, as well as on the average distance each released carrier can travel



$$Q_{\max} = C_i V_{DC}$$

$$RFIC_{\max} = Q_{\max} - C_{\text{tot}} V_{DC}$$

$$RFIC = RFIC_{\max} - \alpha N_i (1 - e^{-e n_i t_1})$$

Figure 6.10 The schematic diagram for the RFIC measurement.

before being retrapped.  $N_T(0)$  is the total number of occupied ZnS traps at time equal to zero, and  $e_T$  is the emission rate of the corresponding traps.

As was shown in equation (6.1), the trap emission rate is a monotonic increasing function of device temperature, therefore the second term of equation (6.7) also increases with device temperature monotonically.

The RFIC(T) curve should fall as the temperature increases. This argument is strictly true only if the insulators are not leaky. However, from the previous WTRC study, it was found that there are also deep traps within the insulator films, whose emission rate becomes quite large above 330K. When the insulator traps get depopulated, they will reduce the net electric field strength of the insulators as in the ZnS case. Since the biasing voltage is at a constant level, this will result in a higher field strength across the ZnS layer as shown in figure 6.11. The RFIC signal directly measures the residual ZnS field strength at the end of  $t_d$ , it is therefore possible to have the RFIC signal increase as the device temperature increases. A more accurate expression for the RFIC signal is thus

$$\text{RFIC}(T) = \text{RFIC}_{\text{max}} - \alpha N_T(0)[1 - \exp(-e_T(T)t_d)] + \beta N_I(0)[1 - \exp(-e_I(T)t_d)] \quad (6.8)$$

where  $\beta$  is a proportion constant which represents on the average, how much additional RFIC signal will be induced by each depopulated trap level within the insulator films.  $N_I(0)$  is the total number of filled insulator traps at  $t = 0$ , and  $e_I(T)$  is the emission rate of the

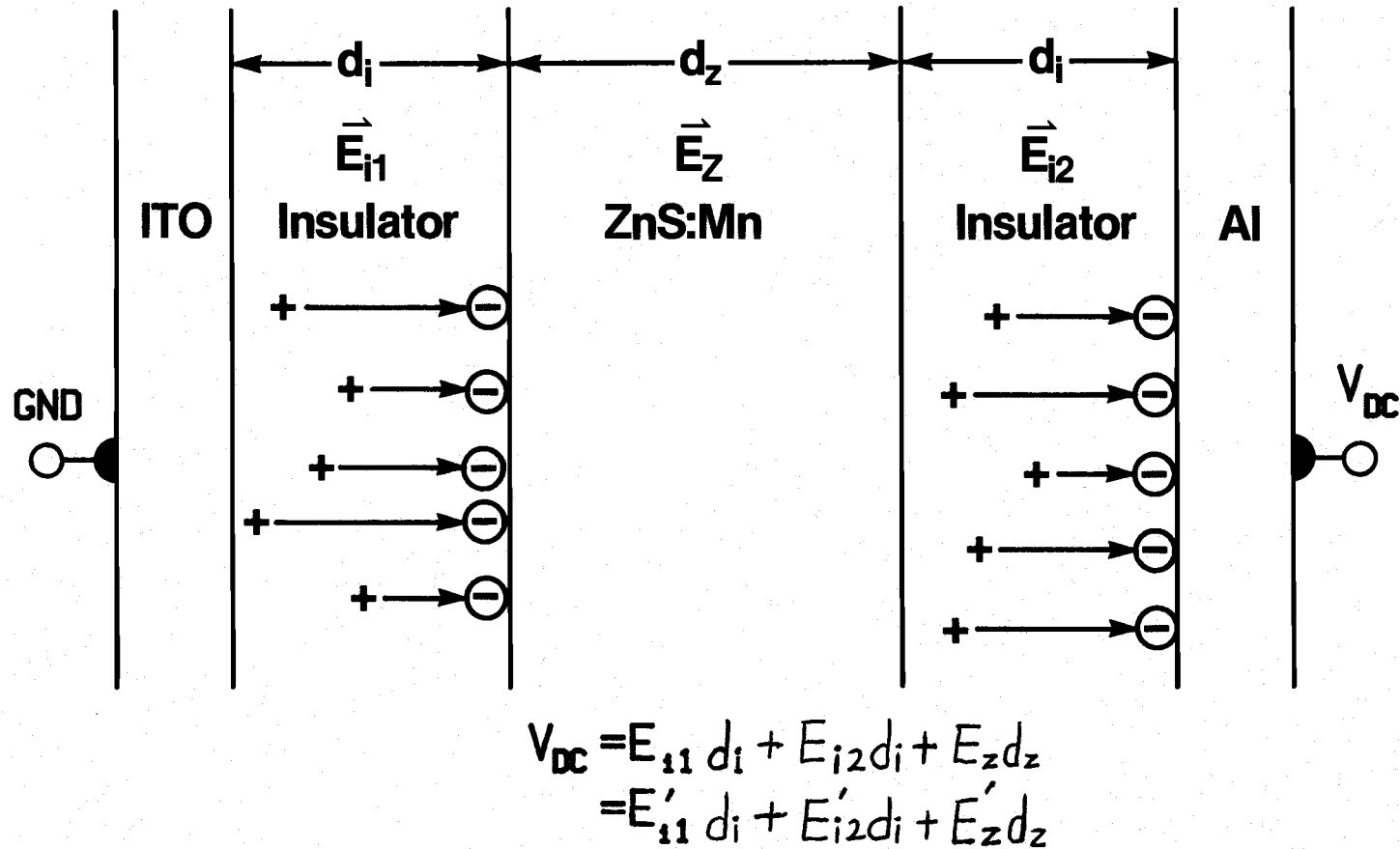


Figure 6.11 The cross-sectional view of the ACTFEL device which illustrate the field enhancement effect across the ZNS layer. The un-primed quantities correspond to the initial electric field strength while the primed ones correspond to after the insulator traps have depopulated.

corresponding traps. Equation (6.8) clearly indicates that the trap states within the ZnS layer, when depopulated during  $t_d$ , will cause the RFIC signal to decrease. The opposite effect will be induced by trap states within the insulator layer.

Experimental results of the RFIC measurement for three samples, each with a different  $Mn^{+2}$  doping, are shown in figure 6.12(a) and (b). In all these figures, the RFIC signal showed an increase at around 300K indicating that the 0.9eV insulator traps were being depopulated. Depending on the  $Mn^{+2}$  doping concentration, the signal also exhibited different levels of decrease at around 380K. The amount of this signal reduction appears to be proportional to the  $Mn^{+2}$  concentration of the ZnS film. According to the previous discussion, the decrease of RFIC signal resulted from the ZnS trap depopulation process and the amount of the decrease is proportional to the density of the corresponding trap level. It is therefore concluded that when the ZnS films are doped with  $Mn^{+2}$  ions, deep traps are introduced into the ZnS layer. Further studies of the RFIC signal, as a function of the device aging time, revealed that the aging process also caused a more pronounced RFIC signal reduction around 380K similar to that induced by the  $Mn^{+2}$  doping process. This effect strongly suggests that the deep level generation within the ZnS film, is also related with the device aging process. Perhaps by means of hot electron bombardment.

The fact that the reduction of the RFIC signal occurs at a temperature higher than that for the signal increment, indicates that the insulator traps have a higher emission rate than the ZnS traps,

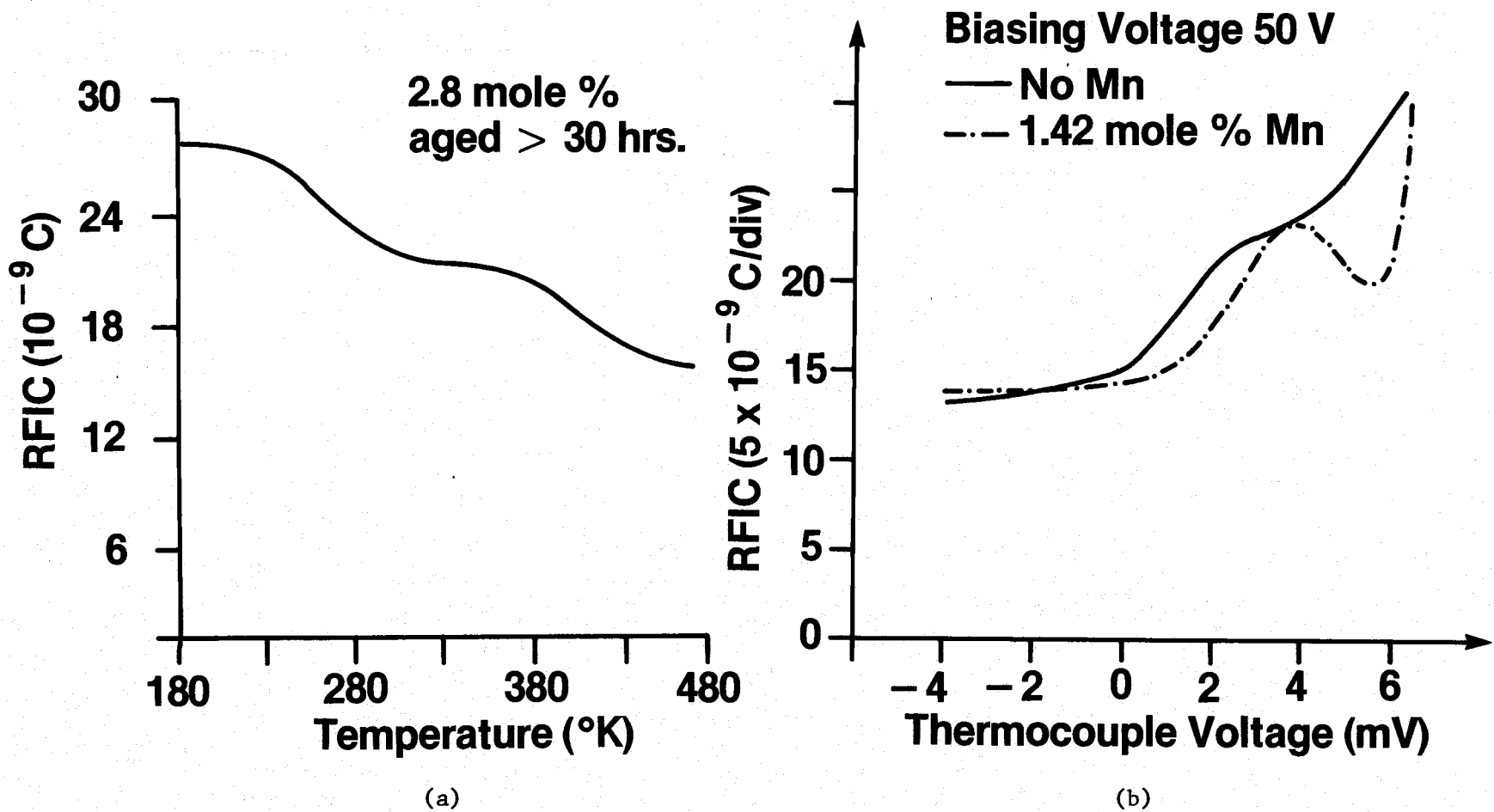


Figure 6.12 The residual field induced charge (RFIC) measurement for three samples each with a different  $\text{Mn}^{+2}$  doping concentration.

which suggests that the energy level for the ZnS traps is probably larger than 0.9eV below the conduction band edge of the ZnS film.

#### 6.4 Discussion

The above two experimental techniques, the WTRC and the RFIC measurement, provided a new approach for studying the trap distribution within thin insulating films by thermal probing. Application of these techniques to the ZnS:Mn ACTFEL devices have resulted in the following:

- (i) For the first time, conclusive experimental evidence showing that there are trap states within the forbidden band gap of the ZnS films is obtained by the RFIC measurement.
- (ii) The RFIC measurement also indicates that the trap generation within the ZnS layer is associated with both the  $\text{Mn}^{+2}$  concentration and the device aging process, which provides information on the device hysteretic behavior.
- (iii) The WTRC signal indicates that there are trap states associated with the insulating  $\text{Y}_2\text{O}_3/\text{Al}_2\text{O}_3$  films. The diverging trend of this WTRC signal above 400K may be responsible for the decrease of hysteresis width at high temperatures.



## THE PHOTOCONDUCTIVITY MEASUREMENT

### 7.1 Introduction

Those ZnS:Mn ACTFEL devices exhibiting the memory effect may be switched on and off optically. Synchronization of u.v. light pulses in phase or out of phase with a driving voltage, sustained within the memory margin [34], will cause the device to switch "on" and "off" respectively. This is due to the photoconductivity within the ZnS layer induced by the u.v. light pulses. The purposes of this photoconductivity experiment are: (i) To study the device photoconductivity spectra response and thus facilitate design of a suitable u.v. light source for efficient optical "writing" and "erasing" of the hysteretic ACTFEL devices, (ii) To verify whether the Auger process is a dominant process for nonradiative decay channels that are observed in the study of temperature effect on those ACTFEL devices [50], and (iii) To investigate the optically active deep levels within the ZnS film.

The high resistivity of the ZnS layer, and the a.c. nature of the device operation, mean that photoconductivity measurements have been very difficult and one is usually forced to use the low frequency lock-in technique. The reason for choosing a low lock-in frequency is to minimize the displacement current component and therefore to

increase the relative magnitude of the photo-current component for easier measurement. The photo conductivity signal may be enhanced by increasing the intensity of the probing monochromatic light. However, in order to avoid nonlinear optical processes, this incident light intensity must not be maintained at a high level. Thus, the photo-induced ZnS conductance is usually too small at long optical wavelengths for accurate measurement when compared with the film capacitances paralleling it, even for a lock-in frequency as low as 10 Hz. Although some improvements may be achieved by using the a.c. Schering bridge technique [68], this requires careful and tedious balancing adjustments at all wavelengths in order to obtain accurate experimental results, also automation of this measurement method is quite involved.

A new photoconductivity measuring technique which employs the d.c. biasing method, therefore eliminating the large shunting capacitance effect, has been developed. This technique has the merits of high sensitivity, very low noise, speed and simplicity of operation, and is readily interfaced with a computer for real-time data manipulation. Another unique feature which cannot be achieved by the a.c. bridge technique is that the sample can be "prepared" to ensure identical trap occupations before each photoconductivity measurement at different optical wavelengths is made. In the a.c. bridge method, the sinusoidal biasing voltage constantly sweeps the photo-released carriers toward the ZnS-insulator interfaces, where the deep interface states are located. The carriers, once trapped at these interfaces, can only be released by capturing a more energetic photon,

as compared to that needed to depopulate a shallower bulk state. This will result in changes of the occupation status of the bulk trap levels, especially when scanning the incident photon energy from low to high levels, therefore it is difficult to interpret the data thus obtained when doing the long wavelength photoconductivity measurements.

## 7.2 Experimental

In figure 7.1, a simplified schematic diagram, which illustrates the essence of the measurement, is shown. The capacitors symbolize the multi-layered device structure and the resistor in parallel with the central capacitor represents the ZnS conductance induced by photon irradiation. All the photoconductivity measurements were performed at near liquid nitrogen temperatures, in order to minimize any thermal generation of carriers. The sample biasing voltage, which was chosen to be at 50 volt d.c., generates an electrical field within the ZnS film more than four times smaller than that of the normal electroluminescence threshold level. Under these conditions there was no detectable conduction current within the ZnS layer whilst the samples were kept in the dark, indicating that neither thermal nor tunneling processes were involved. The unique "preparation" procedure prior to each photoconductivity measurement, may be achieved by two different methods: these are called optical and electrical erasure techniques. The optical erasure was done by illuminating the sample with u.v. light, whilst holding the biasing voltage at zero volt. This will eliminate any residual polarization effect within the ZnS

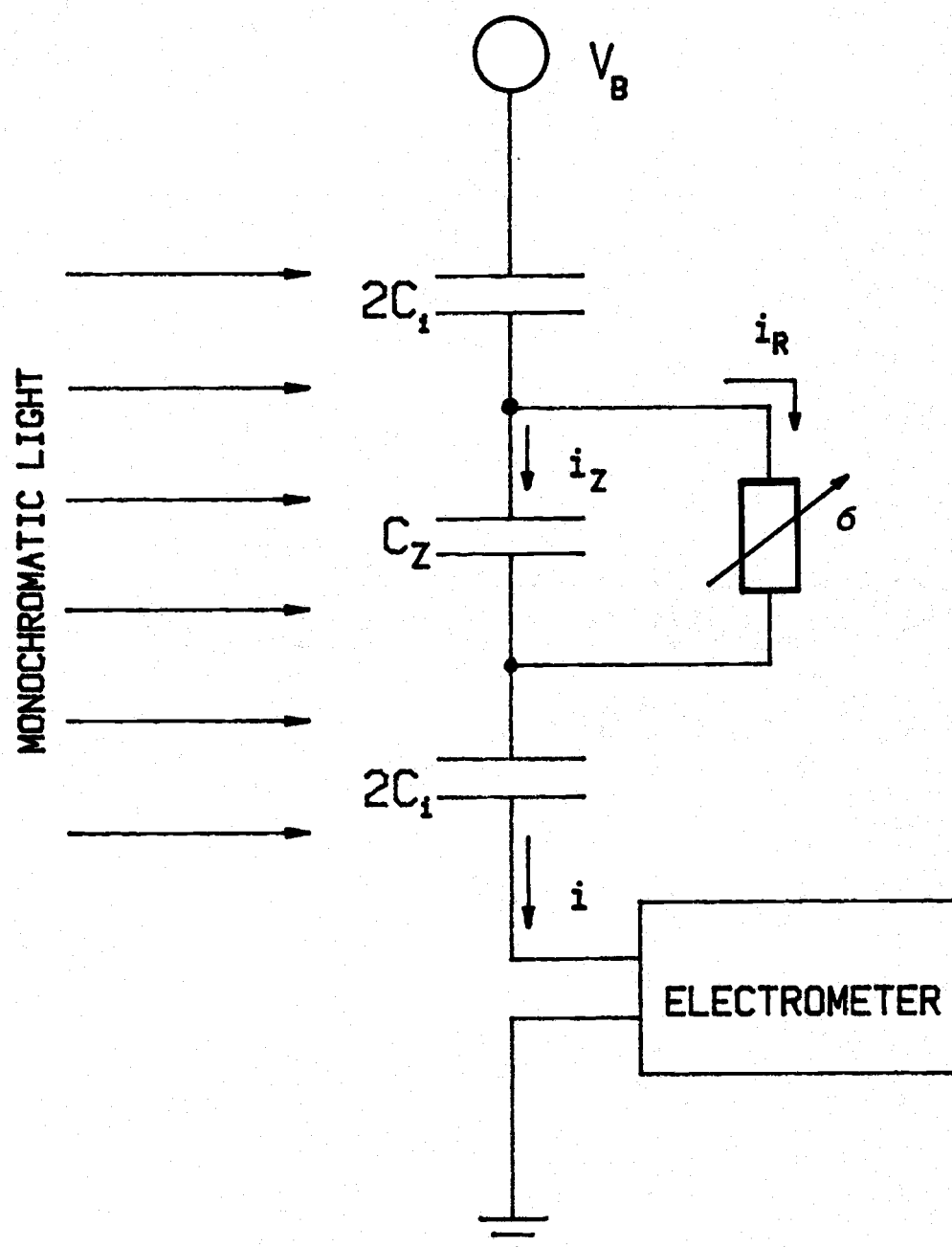


Figure 7.1 The schematic diagram for the photoconductivity measurement where  $C_i$  is the total insulator capacitance,  $\sigma$  is the photon induced ZnS conductivity, and  $V_B$  is the low d.c. biasing voltage.

layer and fill up some of the bulk trap levels. The electrical erasure was accomplished by first applying a sequence of narrow a.c. pulses until the device electroluminescence had been turned on, subsequent reduction of the driving voltage to near zero volt ensures the electrical erasure. The term "erasure" here simply means removal of the photoconductivity induced internal ZnS polarization from the previous measurement.

The optical erasing process was designed to study the ZnS bulk trap states whilst minimizing the occupation of interface states and therefore their influence on the measured signal. The electrical erasure process, on the other hand, was intended to examine the effects of residual occupied interface states on the photoconductivity measurement.

The experimental procedures are as follows: With the sample properly "prepared" for identical trap occupation via either of the erasing methods, the low d.c. biasing voltage at 50 volts was applied. This will induce a significant amount of displacement current flow and create a biasing electric field within the ZnS layer. After the displacement current has settled down, which usually took hardly any time ( $\leq 2 \mu\text{s}$ ), a monochromatic light, which was generated by a Jarrell-Ash monochromator and controlled by an electric shutter, was illuminated onto the sample. Immediately following the exposure of the sample to the probing monochromatic light, the photo-induced conduction current was integrated by a Keithley model 616 electrometer, which was operating in the coulomb mode, for a time period  $t_0$ . The amount of this integrated charge was subsequently registered on an X-Y recorder,

together with the corresponding monochromatic light wavelength. The wavelength was then changed and the measurement procedures repeated. Notice that because of the "preparing" procedure prior to each photoconductivity measurement, identical results will be obtained with the incident photon energy either scanning up or scanning down. This may not be the case if the a.c. lock-in method is used instead for the measurement, because of the interface retrapping effect mentioned previously.

Referring to figure 7.1 it is now possible to establish what this interface charge is related to. After application of the biasing voltage  $V_B$  but prior to exposure of the sample under the monochromatic light, the voltage across the ZnS layer  $V_Z^0$  is given by

$$V_Z^0 = V_B [C_i / (C_i + C_Z)] \quad (7.1)$$

where  $C_i$  is the total insulator capacitance and  $C_Z$  is the ZnS film capacitance.

As the shutter lets in the monochromatic light, the photo-induced current within the ZnS layer will start to flow and result in changes of the voltage distribution across each capacitors according to

$$V_B = V_Z + V_i \quad (7.2.1)$$

$$i = i_Z + i_R \quad (7.2.2)$$

$$i_R = V_Z \sigma \quad (7.2.3)$$

$$i_Z = C_Z (dV_Z / dt) \quad (7.2.4)$$

where  $V_i$  is the voltage across the two insulators,  $i$  is the externally observed device photo-current,  $i_Z$  is the ZnS displacement current,

$i_R$  is the ZnS conductive current, and  $\sigma$  is the photo-induced ZnS conductance.

From equation (7.2)

$$\begin{aligned} i_Z &= -C_Z(dV_i/dt) \\ &= -C_Z(i/C_i) \end{aligned} \quad (7.3)$$

thus

$$\begin{aligned} V_Z &= V_B - V_i = V_B - (1/C_i) \int_0^t i dt \\ &= i_R/\sigma = (1+C_Z/C_i)i/\sigma \end{aligned} \quad (7.4)$$

Solving for equation 7.4, one has

$$i(t) = i_0 \exp[-\sigma t/(C_i + C_Z)] \quad (7.5)$$

where  $i_0$  is the initial, externally observed, photo-current and is given by

$$i_0 = V_Z^0 \sigma = C_i \sigma V_B / (C_i + C_Z) \quad (7.6)$$

The amount of the external photo-current integrated after time  $t_0$  is given by

$$\begin{aligned} Q_{PC} &= \int_0^{t_0} i(t) dt \\ &= \int_0^{t_0} [C_i \sigma V_B / (C_i + C_Z)] \exp[-\sigma t/(C_i + C_Z)] dt \\ &= C_i V_B \{1 - \exp[-\sigma t_0/(C_i + C_Z)]\} \end{aligned} \quad (7.7)$$

If the integration time  $t_0$  is chosen to be small enough, the above equation can be approximated by

$$\begin{aligned} Q_{PC} &\approx C_i V_B \{1 - 1 + [\sigma t_0/(C_i + C_Z)]\} \\ &= C_i V_B \sigma t_0 / (C_i + C_Z) \end{aligned} \quad (7.8)$$

It is clear from equation (7.8) that by judicious choice of the integration time  $t_0$ , the charge  $Q_{PC}$  thus integrated directly measures

the ZnS photoconductivity. It must be appreciated that during each measurement, all the parameters including the trap occupation status of the ZnS layer after the erasing process, the magnitude of the low d.c. biasing voltage, as well as the timing for each measurement step, especially for the charge integration time  $t_0$ , have to be controlled precisely in order to ensure accurate experimental data. Thus it is essential to have an automated measuring system to perform this experiment. A Motorola 6800 based single board micro computer has been used as the control unit to achieve the required control precision. The complete system and the control timing diagram are shown in figure 7.2. Throughout the whole spectra range of the photoconductivity measurement on each sample, the photocurrent integration time  $t_0$  was kept at a constant level in order to minimize any error introduced by uncertainty in the timing control.

Since the spectral response of the photoconductivity varies over a wide range, if the incident monochromatic light were to be maintained at a constant intensity for all the wavelengths, and the measurement parameters are chosen such as to have a reasonable sensitivity for the long wavelength regions ( $>8000\text{\AA}$ ), equation (7.8) will probably become a bad approximation for those wavelengths which induce high photoconductivities. One way to cope with this problem, is to tailor the monochromatic light source such that its output intensity tapers off as the wavelength region that will induce a high photoconductivity is approached. The selected light source for this measuring system is a Baush & Lomb, 45 watt, quartz halogen lamp. The light intensity incident on the sample, after the Jarrell-Ash monochromator, the order sorting filters, and the focusing optics,



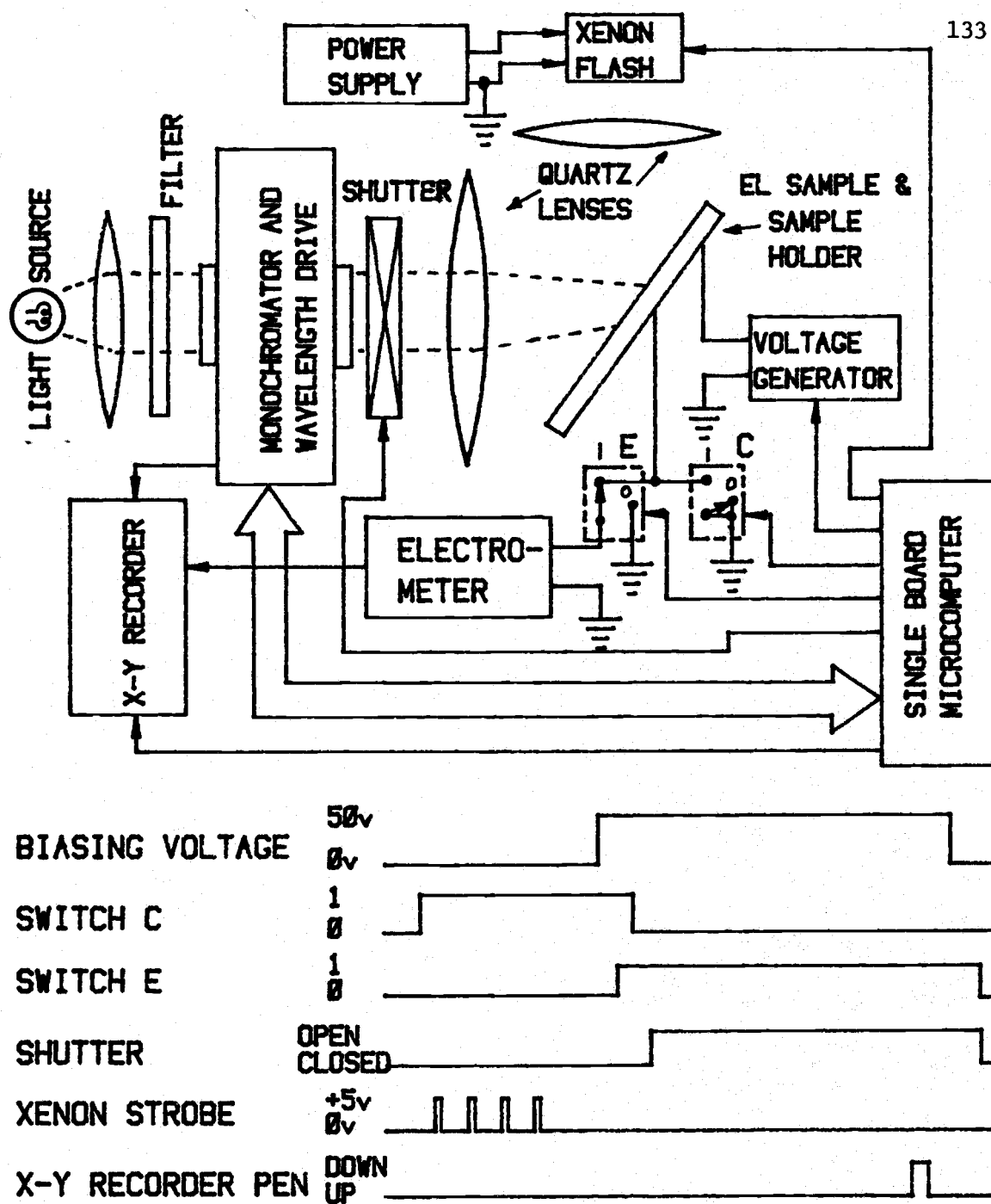


Figure 7.2 The system diagram and the control timing diagram for the photoconductivity measurement.

has a spectra response as shown in figure 7.3. These curves are later used to normalize the final photoconductivity data to the correct spectra response. With the above system as the monochromatic light source, it is ensured that equation (7.8) was always satisfied throughout the whole wavelengths for the photoconductivity measurement.

### 7.3 Results and Analysis

The photoconductivity response of a ZnS:Mn ACTFEL sample covers a wide spectral range and its magnitude has been measured over almost three decades. In figure 7.4 the photoconductivity of a sample, normalized to the incident light intensity and preceded with the optical erasing processes, is plotted against light wavelengths. The sample shown has a 0.2 mole%  $\text{Mn}^{+2}$  concentration and has been aged under a 200 volts driving voltage at  $2\text{KH}_z$  for 1 hour. Owing to the wide range of the photoconductivity, detailed curve structures for wavelengths in excess of  $6600 \text{ \AA}$  were not clearly presented in this linear plot. A supplement to this curve which details the long wavelength response, is shown in figure 7.5. It is seen that a measurable photocurrent starts to flow at an incident light wavelength as long as  $9000 \text{ \AA}$ . The small periodic peaks in these figures are due to the optical interference effect from the multi-layered thin film structure of the device and have been varified by noticing their shift in wavelengths with changes in incident light angle.

In addition to the interference peaks, the photoconductivity spectrum resembles an increasing exponential variation with decreasing wavelengths, until below  $4700 \text{ \AA}$  where a steeper rise is seen.

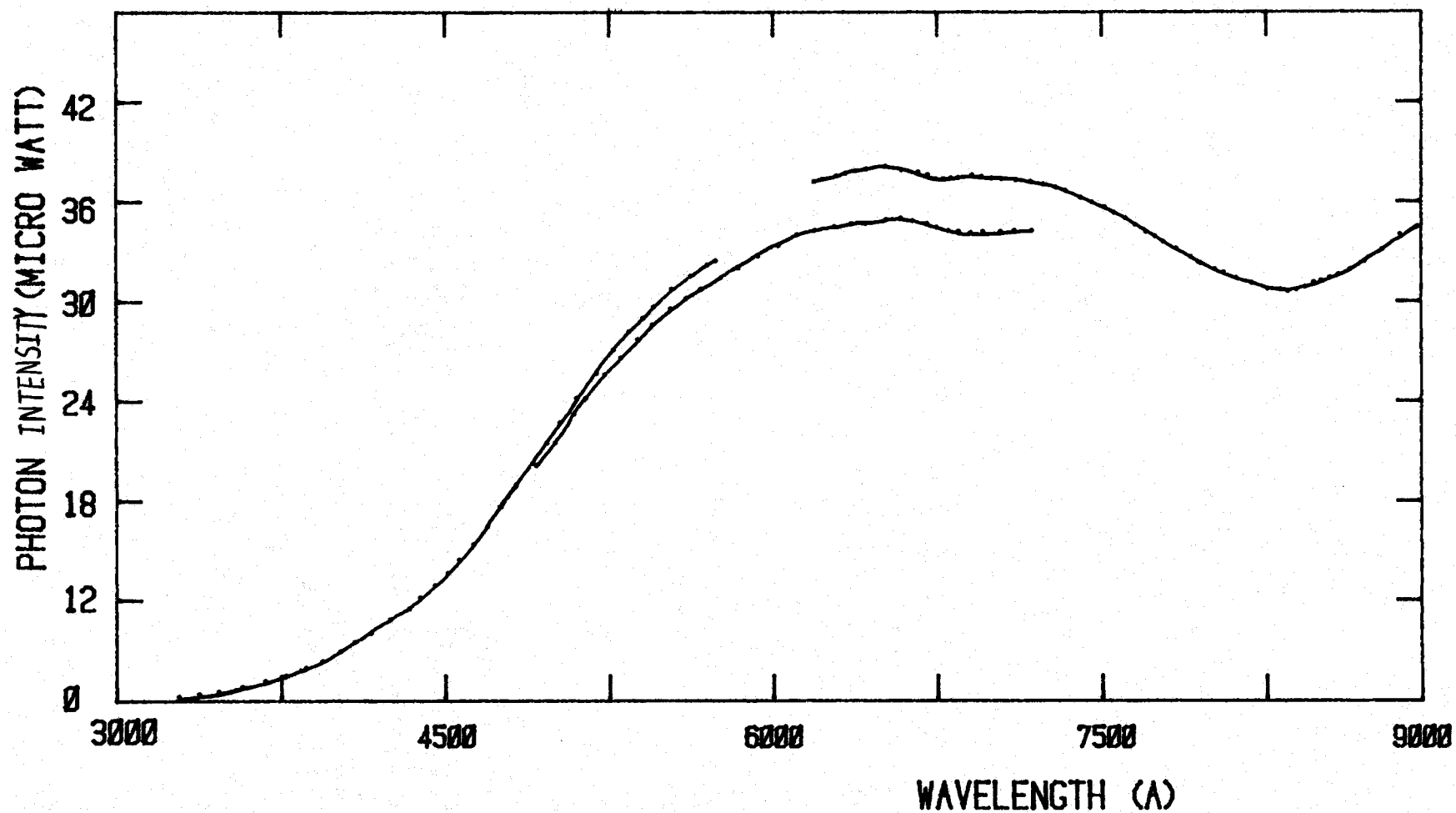


Figure 7.3 The spectra distribution of the light intensity of the monochromatic light source including the necessary focusing and order sorting optics. The segments correspond to three different order sorting filters for each wavelength region.

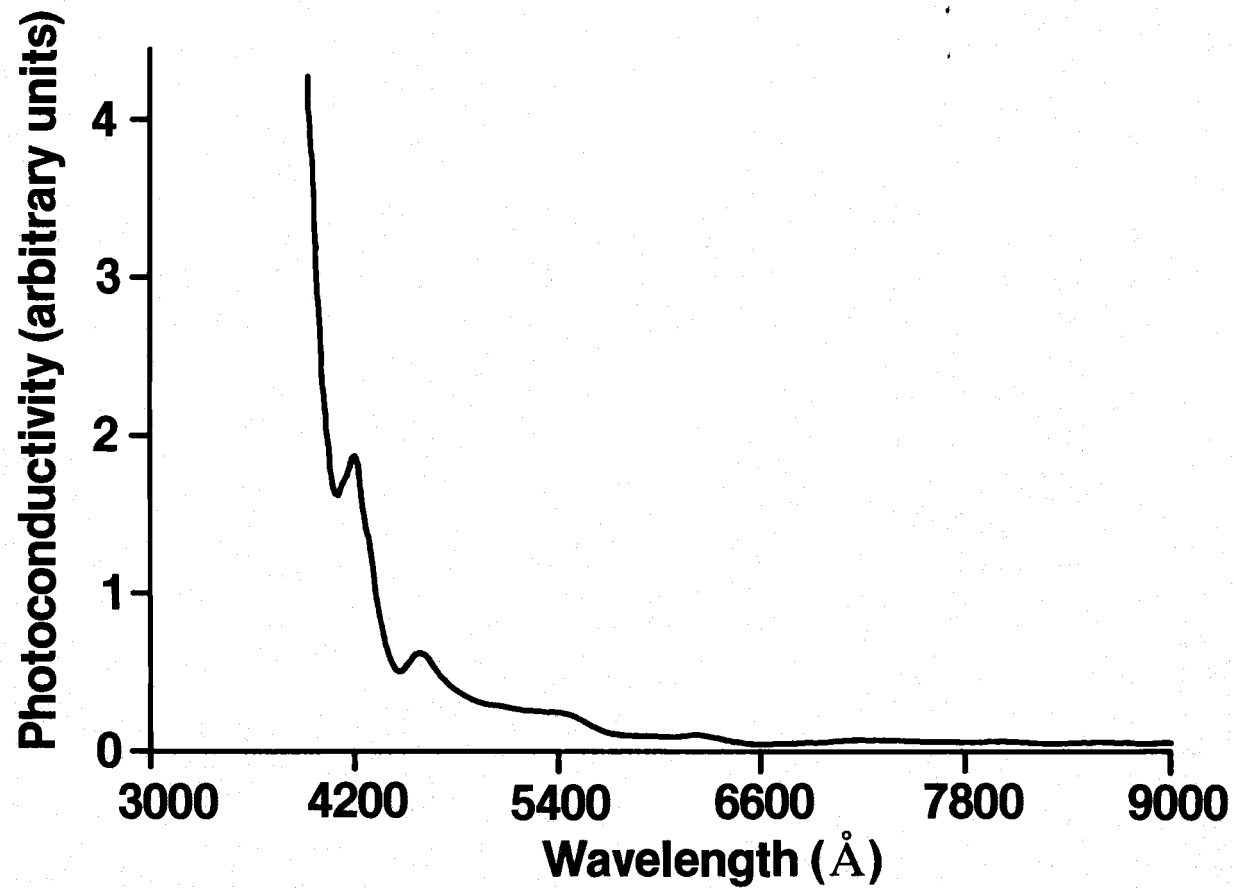


Figure 7.4 The photoconductivity response of a 0.2mole% Mn-doping sample. Detailed spectra response for wavelengths longer than 6500Å is shown in figure 7.5 next.

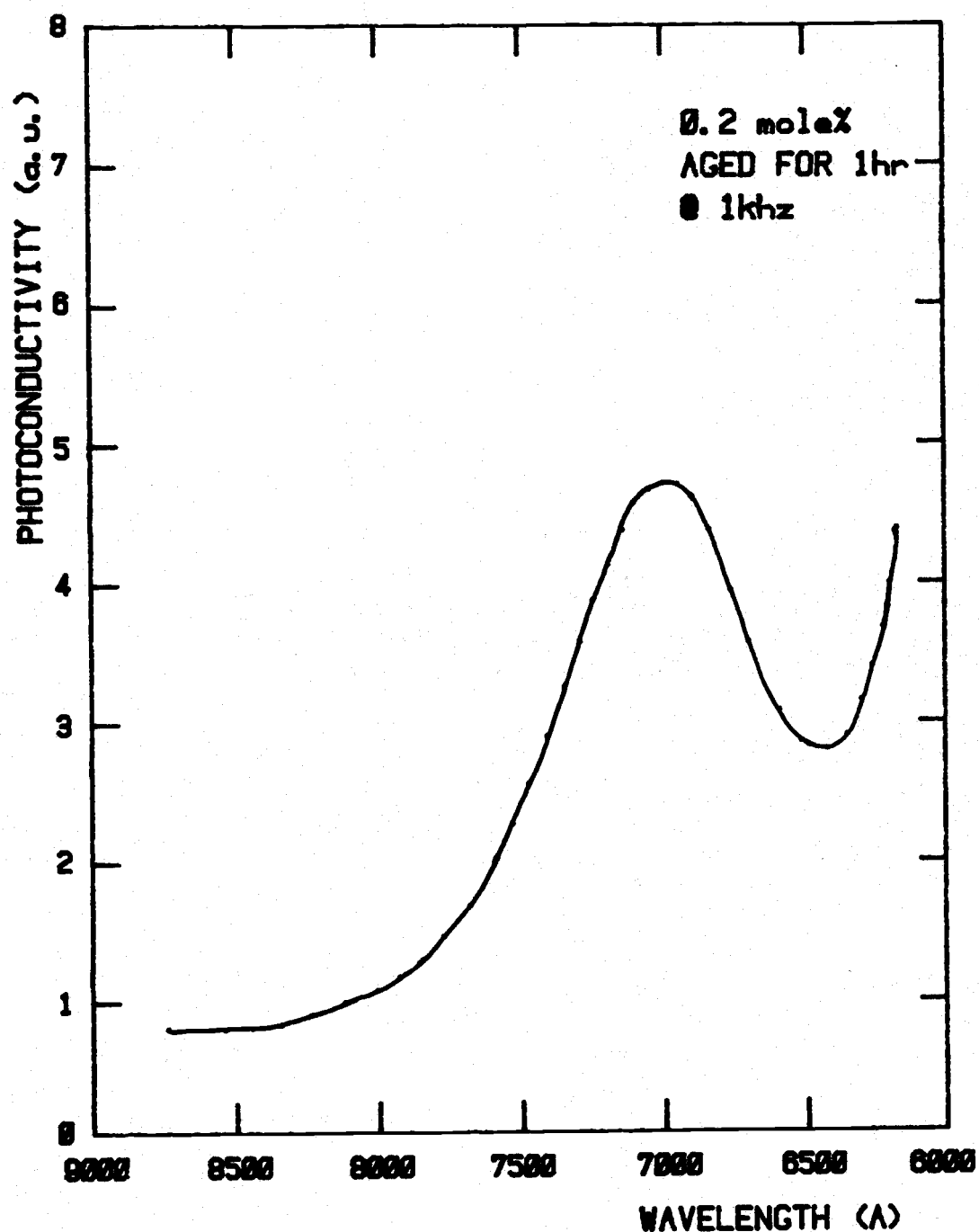


Figure 7.5 The photoconductivity response of the previous sample, figure 7.4, for incident light wavelengths longer than 6500 Å.

A semi-logarithmic plot of this photoconductivity against the corresponding photon energy, shown in figure 7.6, demonstrates this more clearly. The curve on the semi-log plot is approximated by two straight lines each with a different slope which meet at around  $4700 \text{ \AA}$ . This is, as suggested by Cusano [5], due to different transition processes at two separate sites within the ZnS layer. The higher energy portion comes from electronic transitions at self-activated centers, whilst the long wavelength segment is due to photo-ionization of deep lying impurity states. The self-activated centers manifest their existence by the appearance of a fast decaying broad band blue emission observed previously in the time resolved spectrum analysis. The deep lying impurity states in the ZnS layer are probably due to unintentionally incorporated group V elements substituting for sulfur atoms [13].

The overall photoconduction sensitivity is a function of device  $\text{Mn}^{+2}$  concentration. Figure 7.7 shows the relative photoconductivity at  $5400 \text{ \AA}$  for three samples each with a different  $\text{Mn}^{+2}$  doping level. The decrease in photo-sensitivity with increasing device manganese concentration, as show in the figure, is attributed to the introduction of deep levels into the ZnS film with  $\text{Mn}^{+2}$  doping. In the presence of trap levels, the carrier life time, and hence its mobility, is reduced. Since the photo-response of a material is proportional to the product of free carrier life time and free carrier mobility [69], a reduction of device photoconductivity with high  $\text{Mn}^{+2}$  doping levels should be anticipated.

The aging phenomenon associated with the ACTFEL devices also affects the device photoconductivity. The relative photoconductivity

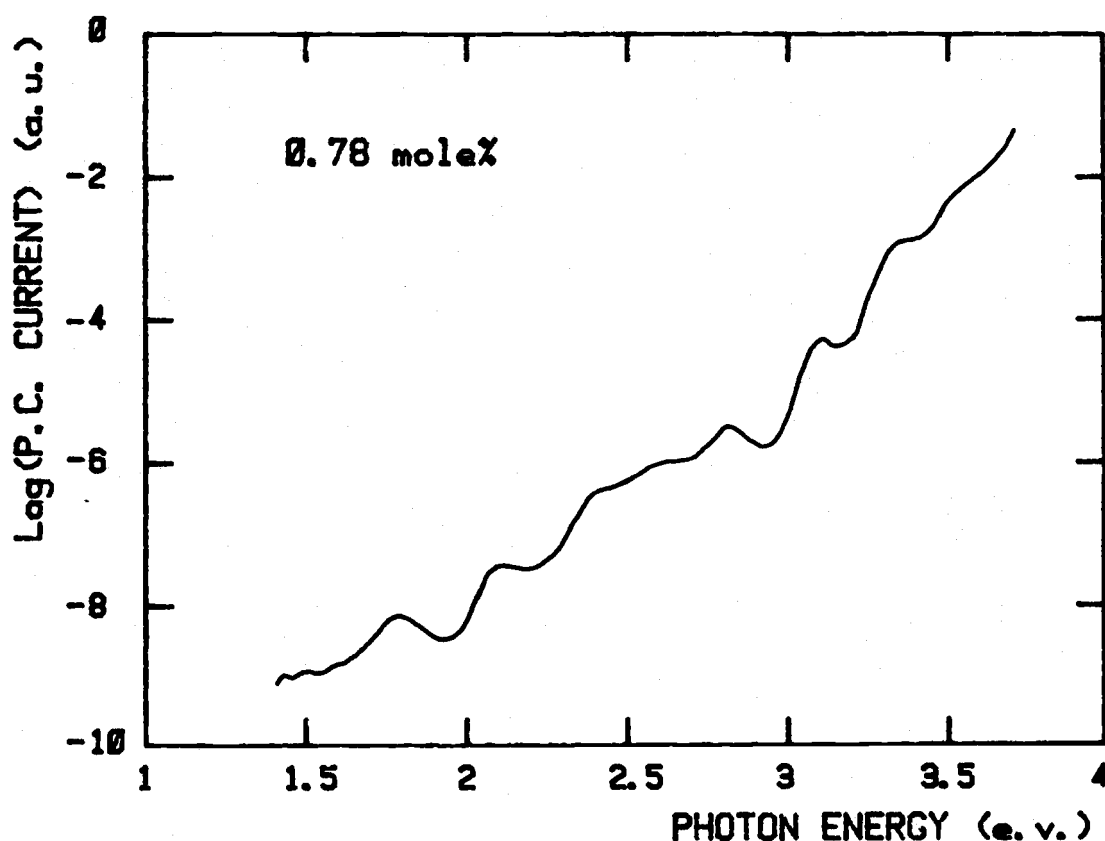


Figure 7.6 The semi-logarithmic plot of the photoconductivity versus photon energy. The two regions with apparent broken slopes correspond to the impurity photoconductivity and the electronic transitions at the donor-acceptor like self-activated centers.

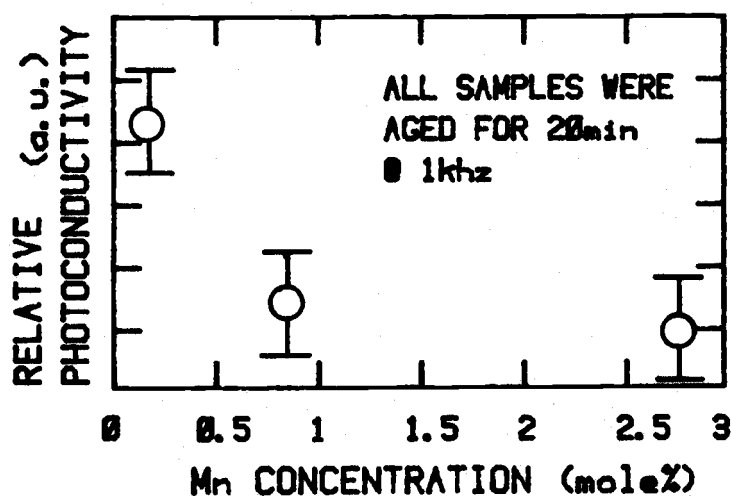


Figure 7.7 The relative photoconductivity at a photon wavelength of  $5400\text{\AA}$  as a function of the device  $\text{Mn}^{+2}$  concentration.

spectra response for a sample with a 0.82 mole%  $\text{Mn}^{+2}$  doping at two different aging status is shown in figure 7.8. It appears as if the aging process simply reduces the magnitude of the response without significant change in its shape. Since it has been shown in earlier discussions that deep levels are generated within the ZnS layer while the aging process continues, and presence of the deep traps will reduce the device photoconduction response, the above phenomenon is consistent with deep level generation being associated with the device aging. Further study of the photoconductivity spectra on different samples revealed that the general shape of the response curve is largely independent of either the aging status or the  $\text{Mn}^{+2}$  concentration of an ACTFEL device. Since both of these factors lead to generation of deep levels within the ZnS film, the lack of their influence on the shape of the photoconductivity curve suggests that those deep states have a fairly uniform energy distribution as well as small photon capture cross sections. Also, the absence of photoconductivity enhancement at around the manganese ion absorption peaks, even for samples with a high  $\text{Mn}^{+2}$  doping level, suggests that the Auger process, which is a candidate for the dominant  $\text{Mn}^{+2}$  non-radiative decay channels, may not be as active as in some rare earth doped systems [9].

Comparison of the long wavelength,  $\geq 6500 \text{ \AA}$ , photoconductivity with the sample prepared by either the optical or the electrical erasing processes does indicate some differences. Figure 7.9 shows the photoconductivity data for a sample prepared with both of the optical and the electrical erasing methods at two different aging



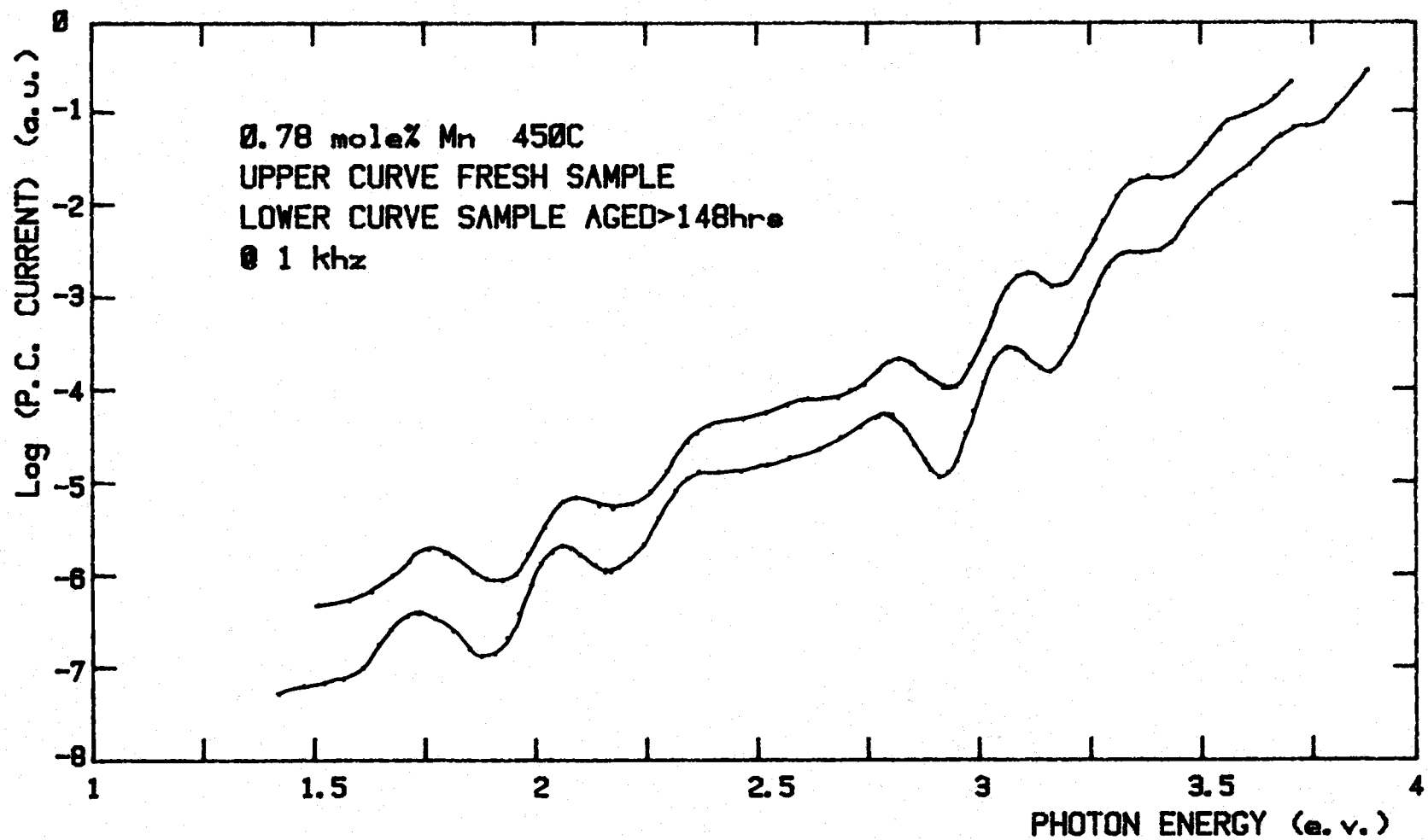


Figure 7.8 The photoconductivity spectra response of the 0.82mole% Mn -doping sample. The significant change appears to be the overall photo-sensitivity only.

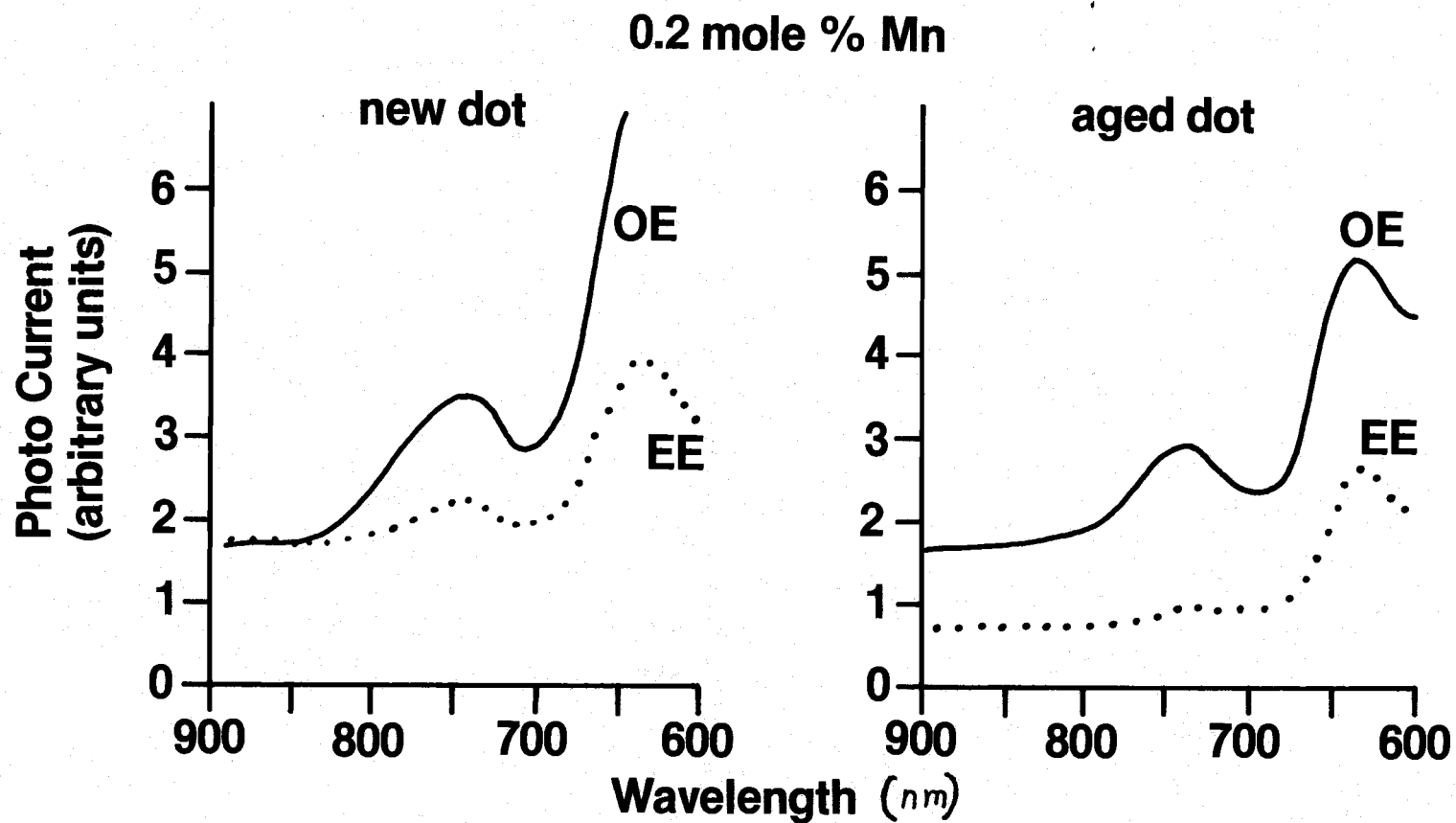


Figure 7.9 The photoconductivity response at long wavelengths, ( $>6500\text{\AA}$ ), when under either the optical erase (OE) and the electrical erase (EE) methods. The figure shows the difference between (OE) and (EE) at around  $9000\text{\AA}$  increases whilst the aging process develops.

status. In each case, the optical erasure method yielded a higher photoconductivity response than did the electrical erasure method, and the difference between them at wavelengths greater than  $8000 \text{ \AA}$  increases as device aging continues. Similar differences have also been observed in other samples with different  $\text{Mn}^{+2}$  concentrations.

Several mechanisms, whose existence have been confirmed by other measurements, may have been responsible for this phenomenon. These are, (i) increased bulk trap density from aging resulting in a higher total number of occupied shallow levels in the ZnS bulk when using the optical erasing method, probably due to retrapping of the photo-generated free carriers at those bulk traps. (ii) When using the electrical erasing method, the high electric field induced by the driving voltage causes the shallow bulk states become unstable, this disfavors the occupation of those states which would yield long wavelength photoconductivities. (iii) The deep interface states, whose density were increased by aging, once filled with electrons from turning on the device electroluminescence, will not be depleted when the driving voltage is reduced to zero volt. The electrical erasing process therefore, causes fewer electrons to be left in the shallower bulk states. This effect will become more pronounced as aging continues.

#### 7.4 Summary

A new experimental technique for measuring d.c. photoconductivity in thin film devices has been described. This technique obviates problems associated with large shunting capacitive reactances of

those thin film devices encountered in a.c. lock-in measurements. An unique "preparing" procedure further reduced the complication of interface states effects. Application of this new measuring technique to ZnS:Mn ACTFEL devices revealed that impurity photoconductivity starts at a photon energy as low as 1.3 e.V.. This is in agreement with the speculation proposed in the RFIC experiment, see chapter six, that the majority ZnS bulk traps have an activation energy of greater than 0.9 e.V.. The decrease in ZnS photosensitivity, caused by generation of deep traps within the ZnS film, has been found to be associated with increase in the Mn concentration within the ZnS, as well as with the device aging process. This confirms with the earlier observations:

- (i) When incorporating  $\text{Mn}^{+2}$  ions into the ZnS layer, deep traps are also introduced, probably due to the formation of active complexes or modification of the ZnS grain structures.
- (ii) The device aging process will generate deep bulk traps, possibly due to hot electron bombardment onto the crystal lattice.

Creation of deeper interface states has been inferred from the development of differences in long wavelength photoconductivity between the optical and the electrical erasing procedures. The increase of that difference with aging suggests the generation of interface states and is probably caused again by hot electron bombardment. From the observation that, other than sensitivity, the general shape of the photoconductivity spectrum is almost independent

of either the  $\text{Mn}^{+2}$  concentration or the sample aging status, it is suggested that:

- (i) The deep levels within the ZnS film have a fairly uniform distribution in energy.
- (ii) The deep levels have a small photon capture cross section and therefore, no significant distortion of the shape of the photoresponse curve was observed, even if the trap density had been changed over a wide range due to the large differences in the  $\text{Mn}^{+2}$  concentration.

Further it appears that the Auger process, where conduction electrons are generated from relaxation of the  $\text{Mn}^{+2}$  ions, is not the dominant nonradiative decay channel for manganese ions in their excited states because of the lack of enhancement in photoconductivity at wavelengths corresponding to the  $\text{Mn}^{+2}$  absorption peaks even for samples with very high  $\text{Mn}^{+2}$  - doping levels.

## A MODEL FOR THE NEGATIVE RESISTANCE EFFECT AND ITS IMPLICATIONS ON THE ELECTRICAL CONTROL OF HYSTERESIS IN ACTFEL DEVICES

### 8.1 Introduction

The hysteresis characteristics of the ZnS:Mn ACTFEL devices has been observed to be associated with the appearance of minute, bistable conduction filaments [30], [31]. The B-V curve of each of the conduction filaments, shown in figure 8.1, exhibits abrupt transitions between its on and off states, and a speculative model based on a negative resistance effect was proposed for the origin of these abrupt-switching conduction filaments [30]. Recently, direct experimental evidence indicating the existence of such a negative resistance behavior has been obtained from a study of the Q-V diagram of samples with large hysteretic characteristics [9], [78]. Figure 8.2 shows the typical shape of such a Q-V diagram. On the lower right corner and the upper left corner of the diagram, the amount of conduction charge continues to increase while the driving voltage is at a constant level. However, due to the polarization effect caused by the conduction charge itself, the effective ZnS electric field during that period is actually decreasing, therefore some negative resistance effect must be involved in order to maintain the continued flow of the conduction charge.

Based on the above observations, several phenomenological models have been proposed to describe the operation and hysteresis property of the ACTFEL devices [29], [44]. Although these models are quite successful in explaining some device characteristics, they do not

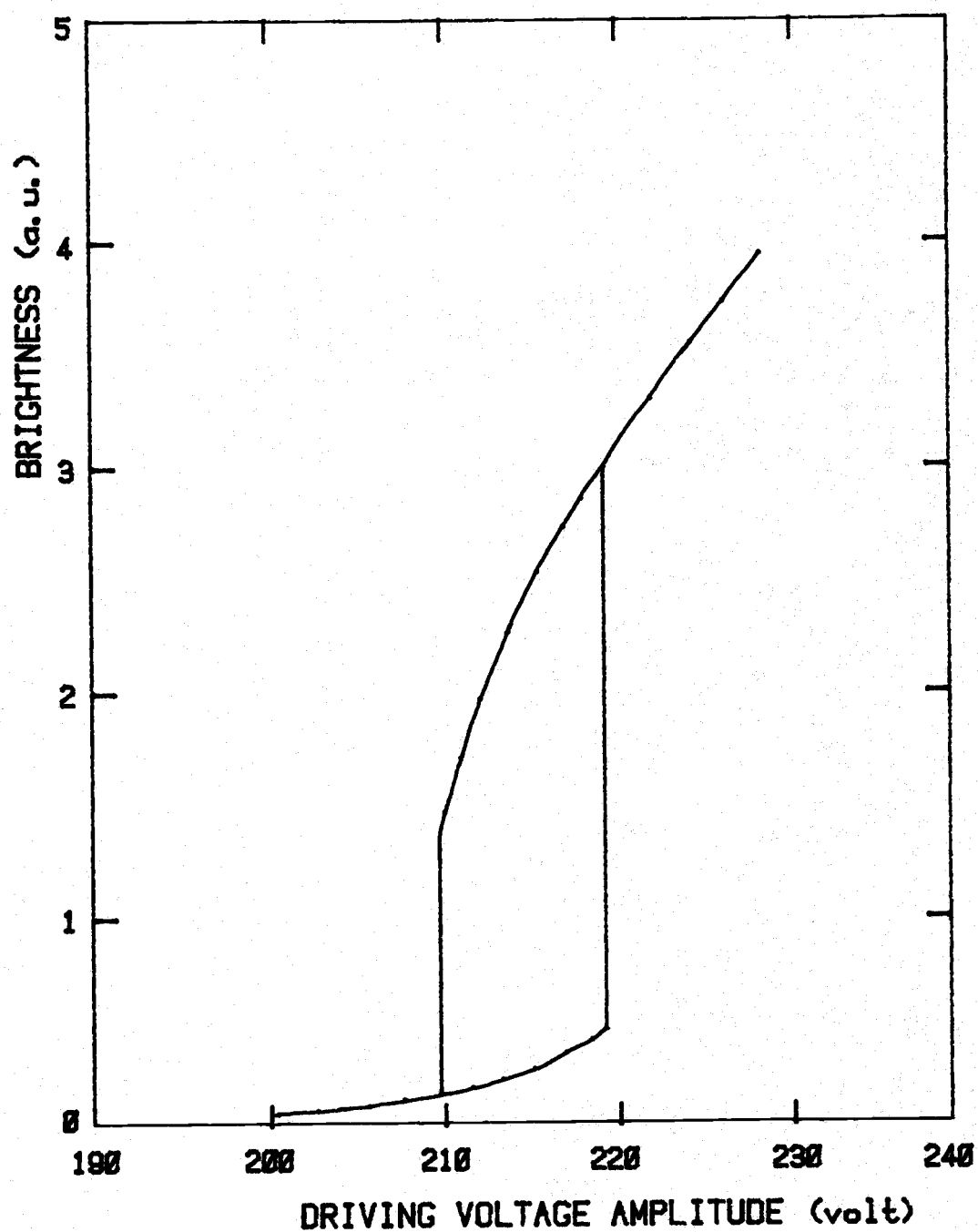


Figure 8.1 The B-V diagram of a single conduction filament.  
(after Ruhle, Marrello, and Onton [30])

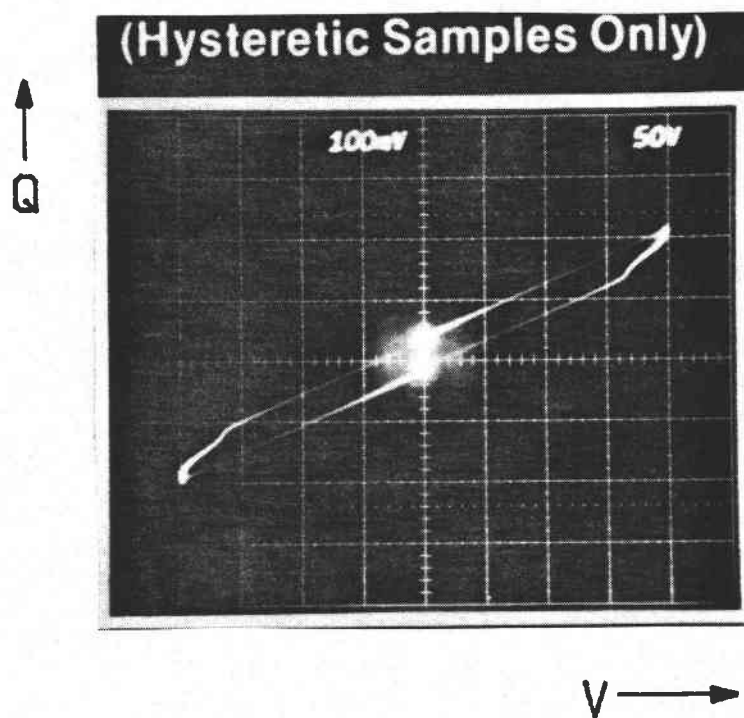


Figure 8.2 The Q-V diagram of a ZnS:Mn ACTFEL sample with a large hysteresis effect. The figure exhibits a negative resistance characteristics at the lower-right and upper-left corner of the Q-V loop.



provide a detailed mechanism for the negative resistance effect. In this chapter, a model which gives a rather detailed description of the physical processes responsible for the negative resistance behavior of the ZnS film is described. This model also explains a number of other phenomena associated with the hysteresis properties of such devices. It emphasizes the importance of the shape of the positive space charge distribution within the ZnS layer on the device hysteric behavior. Wave-form shaping of the driving voltages to affect the positive space charge distribution have resulted in an interesting effect - the electrical switching of a ZnS:Mn ACTFEL device between the hysteretic and non-hysteric states, this phenomenon will be described in more details later.

## 8.2 The Negative Resistance Model

It was learned from the polarization effect associated with the ACTFEL devices that for normal electroluminescence, the fundamental source of electrons for the ZnS dissipative current is from the ZnS - insulator interfaces. Those electrons were originally from the ZnS bulk and their being trapped at the interface states, left behind an equal number of positive space charge in the ZnS bulk. The positive space charge induces a significant distortion of the ZnS electric field as was demonstrated by Marrello and Onton with the  $\text{Mn}^{+2}$  probe layer experiment [71]. Their result showed that the electroluminescence efficiency of the probe layer is strongly dependent on both its location within the ZnS film and the polarity of the excitation voltage. For a probe layer located near one ZnS -

insulator interface, the electroluminescence efficiency is about two orders of magnitude greater for the cathodic conduction cycle than for the anodic conduction cycle of that interface. This phenomenon clearly indicates that there is indeed a positive space charge distribution within the ZnS bulk which has strongly enhanced the electric field strength at regions near the cathodic ZnS - insulator interface.

From extensive studies of the dielectric break down process in insulators, especially for the  $\text{SiO}_2$  thin films [72-74], it was found that there usually is a negative resistance type instability during the break down process. A model, which was first proposed by O'Dwyer [75] and refined by other workers [76], [77], suggested that the negative resistance instability is due to impact generation and retrapping of positive space charge near the cathodic electrode along with their positive feed back effect on the cathodic electric field strength, which leads to further injection of electrons from the cathodic electrode. Similar situations may also exist within the ZnS:Mn ACTFEL devices, and the important underlying physical processes are described in the following.

Consider a simple case where only a ZnS layer is fabricated in between the two electrodes. When a biasing voltage  $V_B$  is applied, the energy band diagram of this system will be tilted by the induced electric field  $E_0$  as shown in figure 8.3(a). As the biasing voltage becomes sufficiently high, the electrons having their energy at the Fermi level of the metal electrode, will begin to be injected from the cathodic electrode into the ZnS film via field

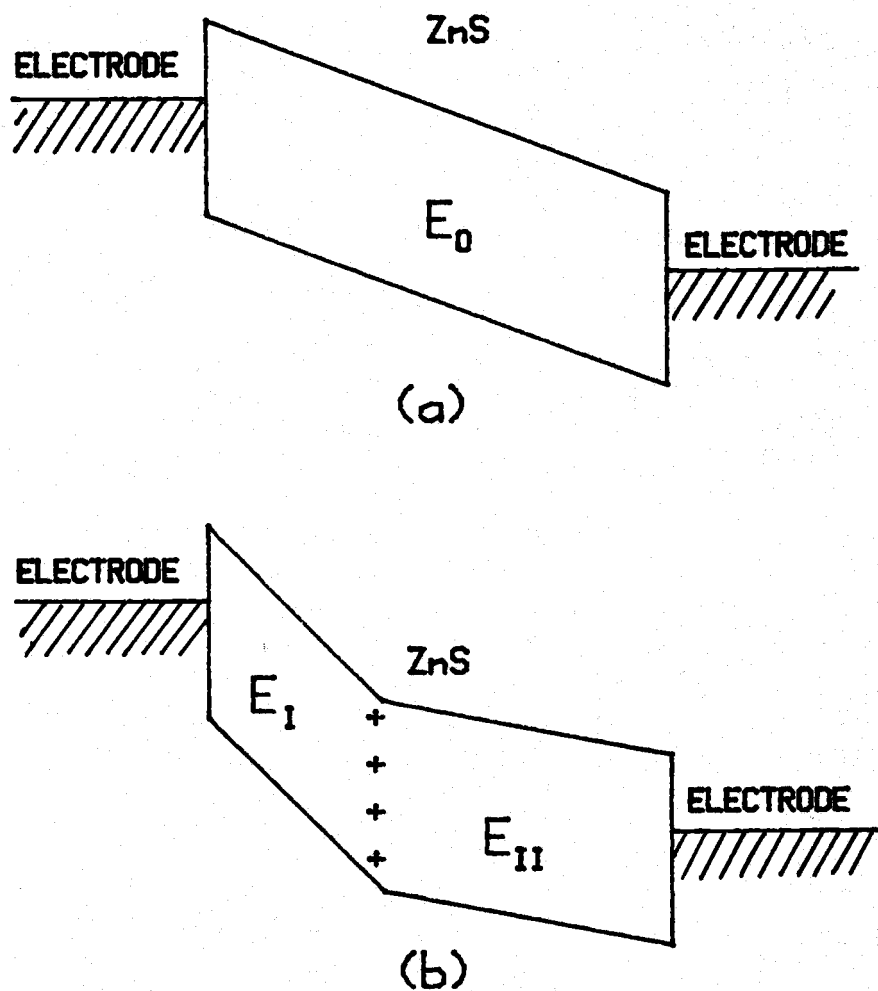


Figure 8.3 The band diagram of a metal-ZnS-metal system before (a) and after (b) the generation of a positive space charge layer. Notice that  $E_I$  becomes larger than  $E_0$  due to the space charge effect.

enhanced processes. They then will be accelerated along the biasing field and make collisions with various scattering centers, such as the  $Mn^{+2}$  ions, self-activated centers, deep impurity states, and ZnS lattice defects etc. Depending upon both the kinetic energy of the electrons and the details of the scattering process, those electrons may or may not induce either generation of electron-hole pairs or ionization of deep lying impurity states. For the situation that the biasing voltage is large enough such that the above process occurred and suppose this lead to the creation of a layer of positive space charge at a distance  $X_0$  from the cathodic electrode due to the ionized impurity centers as well as the deeply trapped holes, figure 8.3(b). The resulting electric field at the region adjacent to the cathodic electrode  $E_I$  as shown in the figure, is then given by the following equations:

$$E_I = E_{II} + (\sigma_1/\epsilon_Z) \quad (8.1.1)$$

and

$$E_I X_0 + E_{II} (d_Z - X_0) = V_B \quad (8.1.2)$$

where  $\sigma_1$  is the surface charge density of the positive space charge layer,  $d_Z$  is the film thickness of the ZnS layer with  $\epsilon_Z$  as its dielectric constant, and  $E_{II}$  is the electric field strength in region II as specified in figure 8.3 (b). Solving equations (8.1) for  $E_I$ , one has

$$\begin{aligned} E_I &= (V_B/d_Z) + (\sigma_1/\epsilon_Z)[1 - (X_0/d_Z)] \\ &= E_0 + (\sigma_1/\epsilon_Z)[1 - (X_0/d_Z)] \end{aligned} \quad (8.2)$$

It is seen that due to the creation of the positive space charge layer, the electric field strength adjacent to the cathodic

electrode is increased by an amount

$$\Delta E_I = (\sigma_1 / \epsilon_Z)(1 - X_0 / d_Z) \quad (8.3)$$

which will lead to injection of additional electrons from the cathodic electrode, since there are unlimited supply of free electrons at its Fermi level. This effect will cause an increased amount of current flow, even if the biasing voltage is at a constant level, thus a negative resistance mechanism is established. Equation (8.3) also indicates that the amount of field enhancement  $\Delta E_I$  is larger if (a) the ZnS film thickness  $d_Z$  is larger or (b) the distance from the positive space charge to the cathodic electrode,  $X_0$ , is smaller. Apparently, the first case can be achieved easily, but the situation for the second case is complicated and will be discussed later.

For a complete ACTFEL device where two additional insulators are inserted between the ZnS - metal electrode interfaces, the situation becomes more involved than the previous case and there are two more conditions which need to be considered: (i) The two insulator layers will provide a negative feedback effect on the voltage across the ZnS layer, as the ZnS conduction current flows, this will be against the field enhancement effect, (ii) now the fundamental source of electrons is from the occupied ZnS - insulator interface states. There is a finite density of states for a given energy interval, whereas there is a continuum of states below the Fermi level for the case of the metal electrode. Having indentified the additional conditions to be considered, it is now possible to examine the negative resistance model for the complete ACTFEL devices.

When the driving voltage establishes an electric field  $E_0$  across

the ZnS film, which is capable of tunneling out electrons from the interface states whose energy levels are less than  $\epsilon_{t1}$  below the conduction band edge of the ZnS film, figure 8.4(a), those electrons will accelerate along  $E_0$ , collide with some scattering centers, as well as induce generation of positive space charge as in the previous case. Let the surface charge density of the injected electrons be denoted as  $P_s$  and suppose that through the collision processes, they have created a layer of positive space charge of surface density  $\sigma_1$  at a distance  $X_0$  from the cathodic ZnS-insulator interface, via either ionization of deep lying impurity states or retrapping of impact generated holes, figure 8.4(b). This process will induce a change of the ZnS polarization level by an amount  $\Delta P$ , which is given by

$$\Delta P = \sum_i q_i X_i = P_s d_Z + \sigma_1 (d_Z - X_0) \quad (8.4)$$

In order to introduce the physical concept of the negative resistance model, without going through complicated mathematic calculations, equation (8.4) implicitly assumes that after the free electrons were created, they all eventually made their way to the anodic ZnS-insulator interface. This polarization change  $\Delta P$  leads to a redistribution of voltages across the ZnS and the insulator films. From equations (3.17) and (3.18), the change in ZnS voltage is given by

$$\begin{aligned} \Delta V_Z &= -\Delta V_i = -2\Delta P / [(C_i + C_Z) d_Z] \\ &= -[2 / (C_i + C_Z)] (P_s + \sigma_1 - \sigma_1 X_0 / d_Z) \end{aligned} \quad (8.5)$$

where  $d_Z$  is the ZnS thickness,  $C_i$  and  $C_Z$  are the capacitances of the insulator and ZnS layers respectively, and  $V_i$  is the change of insulator voltage. The resultant electric field in region I of figure 8.4(b) can then be derived from

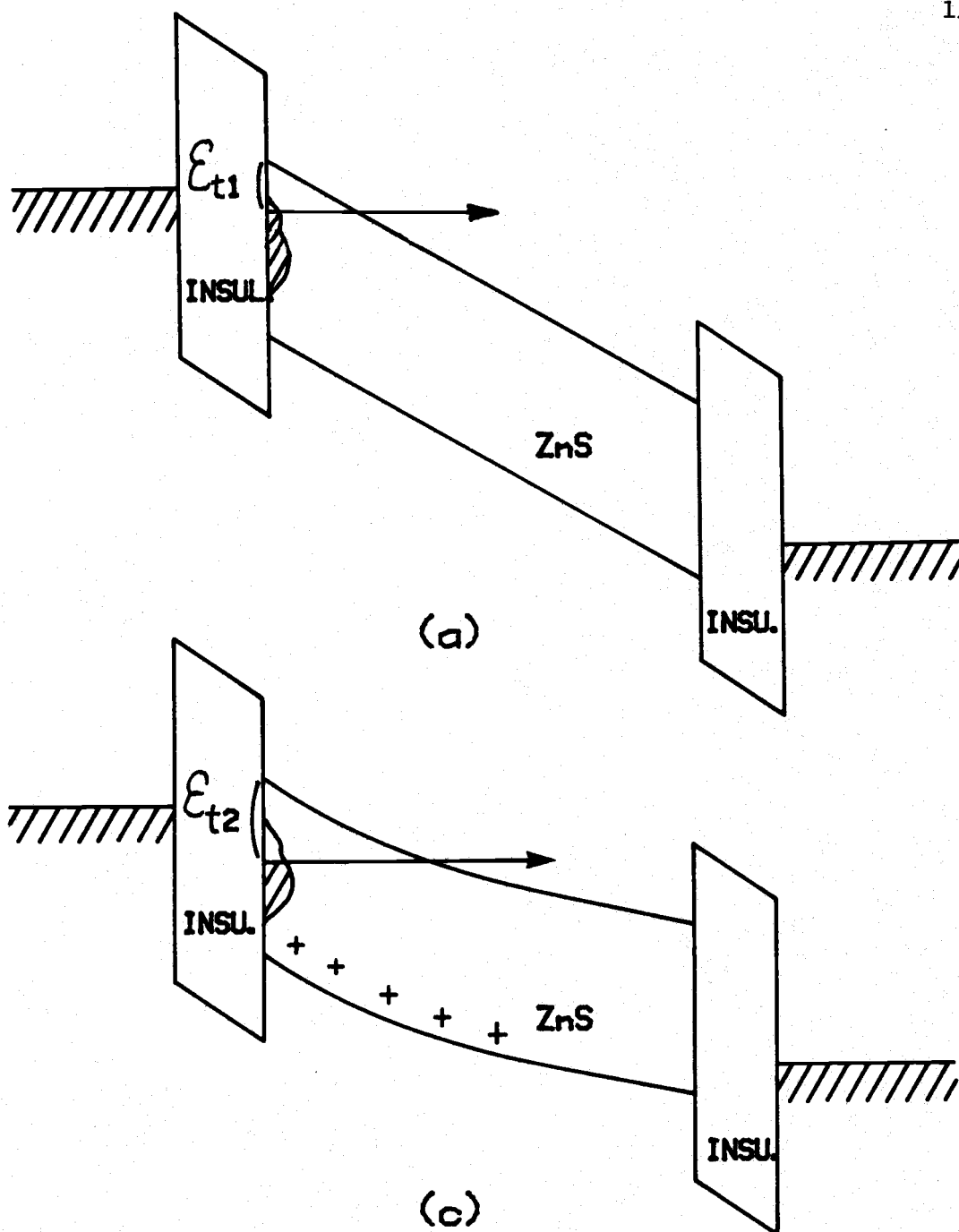
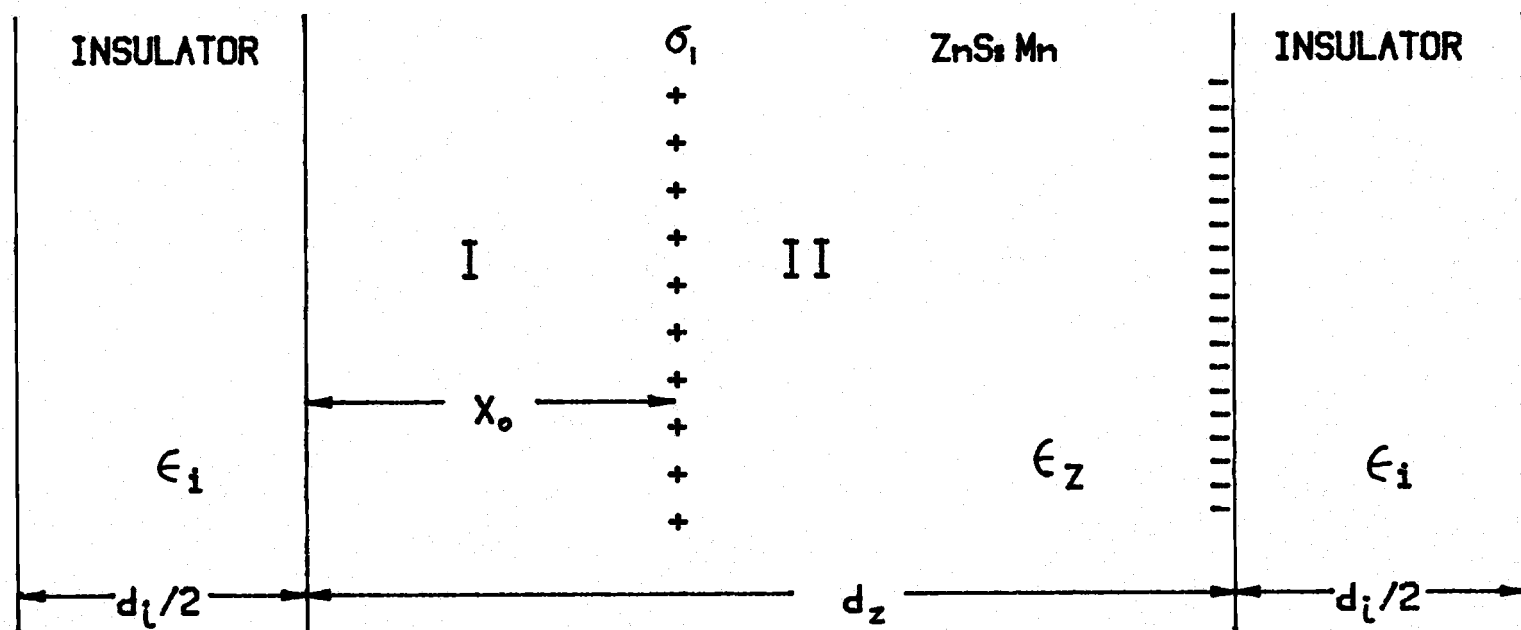


Figure 8.4 (a)&(c) The band diagram of the ACTFEL device. Initially, the biasing voltage is capable of tunneling out interface traps up to  $\epsilon_{t1}$  below the conduction band edge, figure 8.4 (a). After the space charge generation, deeper traps up to depth  $\epsilon_{t2}$  are readily tunneled out by the biasing voltage, due to the field enhancement effect, as shown in figure 8.4 (c).



(b)

Figure 8.4 (b) The cross-sectional view of the ACTFEL device where  $\delta_1$  is the positive space charge generated by the hot electron collision process.



$$E_I = E_{II} + \sigma_1/\epsilon_Z \quad (8.6)$$

and

$$E_I X_0 + E_{II}(d_Z - X_0) = E_0 d_Z + \Delta V_Z \quad (8.7)$$

Solving the aboves for  $E_I$  yields

$$E_I = E_0 + \sigma_1/\epsilon_Z - 2(P_s + \sigma_1)/[(C_i + C_Z)d_Z] \\ - [X_0 \sigma_1/(d_Z \epsilon_Z)](1 - (2\epsilon_Z/d_Z)/(C_i + C_Z)) \quad (8.8)$$

or

$$\Delta E = E_I - E_0 = \sigma_1/\epsilon_Z - \{2(P_s + \sigma_1)/[(C_i + C_Z)d_Z] \\ + [X_0 \sigma_1/(d_Z \epsilon_Z)][1 - (2\epsilon_Z/d_Z)/(C_i + C_Z)]\} \quad (8.9)$$

Examination of equation (8.9) reveals that in order to have a more pronounced field enhancement effect of the ACTFEL device, the second term of the equation is to be kept as small as possible. Further computer simulation of equation (8.9), figure 8.5, shows that the field enhancement effect increases as the ZnS thickness,  $d_Z$ , increases, and will also increase if the distance of the positive space charge from the cathodic interface,  $X_0$ , decreases. The results also indicate that for samples with either a very thin ZnS film (small  $d_Z$ ) or a long positive space charge distance (large  $X_0$ ), the amount of field enhancement can even become negative, under this situation, there will be no negative resistance and therefore device hysteresis observed.

Equation (8.9) provides an answer to the first additional condition, i.e., the negative voltage feedback effect from the insulators to the ZnS film, in determining if the electric field enhancement at the cathodic ZnS-insulator interface would occur after the dissipative

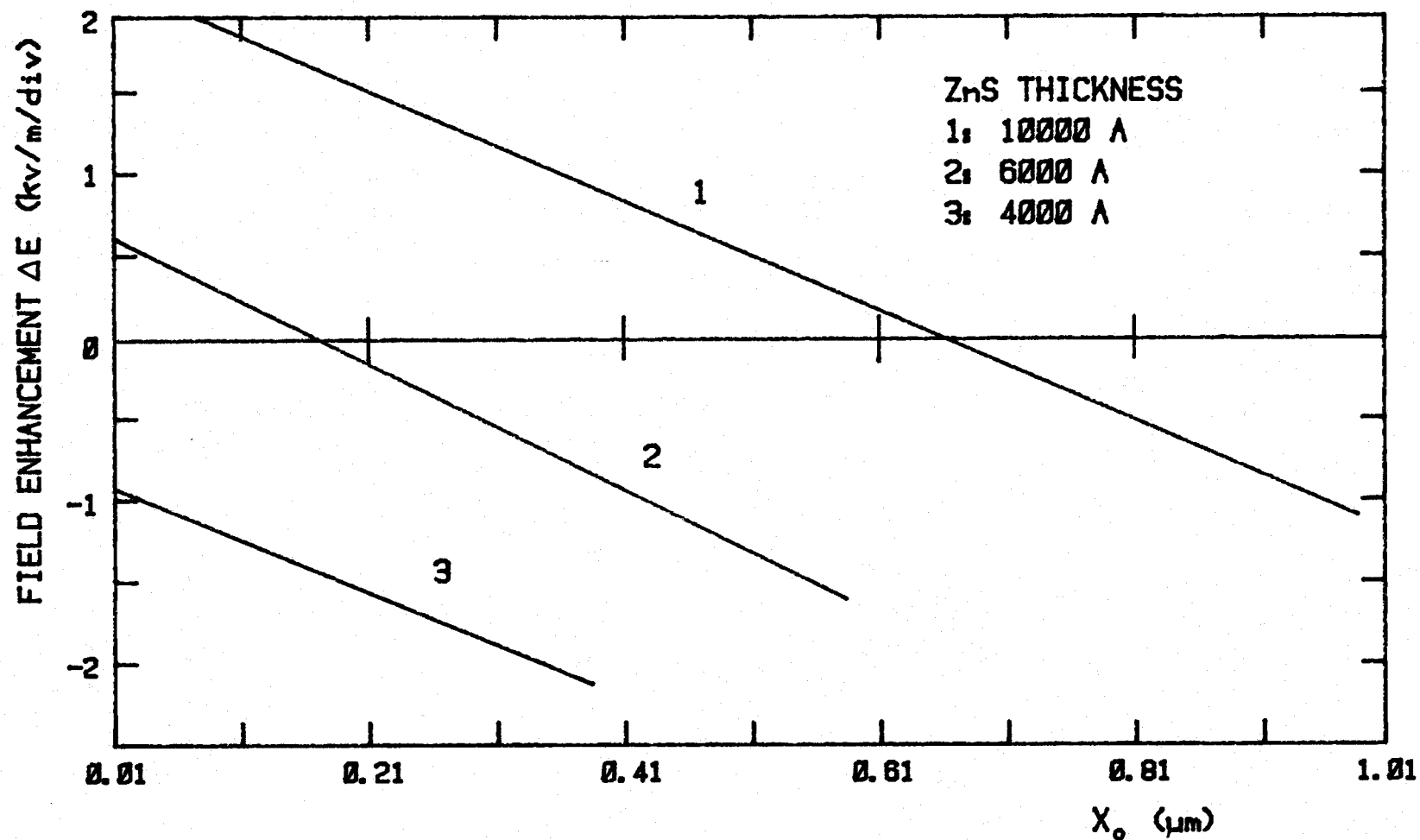


Figure 8.5 The enhancement of the cathode regions electric field as a function of the positive space charge distance  $X_0$  from that interface with the ZnS thickness as the parameter.

conduction process has initiated. For the case that the field enhancement effect will occur, it is still necessary to examine the situations listed in condition (ii) previously, before concluding that the negative resistance behavior will occur. Earlier, it was assumed that before the conduction process took place, the electric field at the cathodic interface  $E_0$ , is able to tunnel out electrons from those interface states whose energy levels are smaller than  $\epsilon_{t1}$  below the bottom of the ZnS conduction band. As the cathodic electric field strength is increased to the new level  $E_I$  due to the field enhancement effect from the positive space charge generated by the initial conduction current, the energy demarcation level, above which electrons become unstable in their interface traps under the biasing field, will move from the original level  $\epsilon_{t1}$  to a new lower level  $\epsilon_{t2}$  as shown in figure 8.4(c). The negative resistance effect will now be strong if the interface states density between energy levels  $\epsilon_{t1}$  and  $\epsilon_{t2}$  is high, since the interface states will be able to supply more conduction electrons to increase the dissipative current as is demanded by the new electric field  $E_I$ . Similarly if the interface states are of low density more conduction electrons will not be available even if  $E_I$  is increased, therefore one would have no or very little negative resistance effect.

All of the above discussions for the negative resistance model are based on an ideal situation and several simple assumptions, where a layer of positive charge  $\sigma_1$  was generated uniformly at a distance  $X_0$  from the cathodic interface, and all of the electrons involved eventually made their way to the anodic interface. However in

practice the situation is quite complicated: the positive space charge is created randomly, and retrapping of free electrons before they reach the anodic interface state will also occur. Nevertheless, this model outlines the essence of the negative resistance process and can be used to estimate qualitatively the device hysteresis behavior. The model suggests that in order to increase the device hysteresis width, a number of parameters can be adjusted to achieve the desired goal;

- (i) Increase the ZnS thickness and maximize the insulator capacitance. This is easily seen from equation (8.9) and the computer simulated result shown in figure 8.4. The electric field enhancement effect increases with either or both of the two adjustments. This effect was also varified experimentally by noticing that there is a superlinear dependence of the hysteresis voltage  $\Delta V_{\text{hys}}$  on the ZnS thickness [42], [31].
- (ii) Shorten the positive space charge distance,  $X_0$ , from the cathodic interface. The effect of decreasing  $X_0$  can also be seen from analyzing equation (8.9) and figure 8.4. The positive space charge distance can be reduced if (a) electrons are scattered by high density of scattering centers, i.e., the mean free path between scatterings are short, and (b) the biasing field is large so that electrons can acquire enough kinetic energy between collisions to ionize either the deep lying impurity states or create electron hole pairs. Criteria

(b) will automatically be satisfied if the device showed negative resistance characteristics, or it can be achieved by applying driving voltages having a very fast rise time. As for criteria (a), it can be fulfilled either by doping the ZnS film with more  $Mn^{+2}$  ions or by aging the sample. The reason is that from the RFIC and the photoconductivity experiments it was learned that deep trap concentration within the ZnS layer increases with either of the above processes. This high density of deep traps provides new scattering centers for the hot electrons which is desired for criteria (a), it also helps to stabilize any free holes shortly after their generation so that the cathodic field enhancement process can develop. The effectiveness of the scattering centers was further checked in the time resolved electroluminescence spectrum analysis earlier, where the intensity of the broad band self-activated emission decreases as the  $Mn^{+2}$  concentration increases, which suggests that the average kinetic energy of hot electrons is reduced by the  $Mn^{+2}$  doping. Although, the increased scattering process disfavors creation of electron hole pairs, due to the existence of deep impurity states [5], the positive space charge generation can be obtain by ionizing those impurity states which requires lesser energy from the electrons, therefore the electrons need not to be too "hot".

(iii) Increase the density of states for the ZnS-insulator

interfaces. This can be achieved by either aging the sample or by choosing an appropriate material for the insulator layers. The effect of the aging process has been discussed earlier and will not be repeated here. The effect of the second consideration has been demonstrated with a special sample where one of the insulator layer is made of  $Y_2O_3$  and the other layer made of  $Al_2O_3$ . This sample showed a large net accumulation of electrons at the  $Y_2O_3$ -ZnS interface as the ZnS conduction begins, which offset its Q-V diagram away from a symmetrical position to the  $Q = 0$  axis. The net accumulated electrons will remain at the ZnS- $Y_2O_3$  interface even after the driving voltage has been gradually reduced to zero [78]. One way of releasing those trapped electrons is to illuminate the sample with an u.v. light source. The origin for electron accumulation at the ZnS- $Y_2O_3$  interface is obviously due to the better electron holding capability for the ZnS- $Y_2O_3$  interface than that for the ZnS- $Al_2O_3$  interface. This is presumably due to a higher interface state density associated with the former interface than the latter. The importance of a high interface state density in generating the negative resistance behavior is verified from examining the Q-V diagram of the special sample which is shown in figure 8.6. This Q-V diagram shows that a negative resistance phenomenon is observed only for the conduction cycles when electrons are ejecting from the

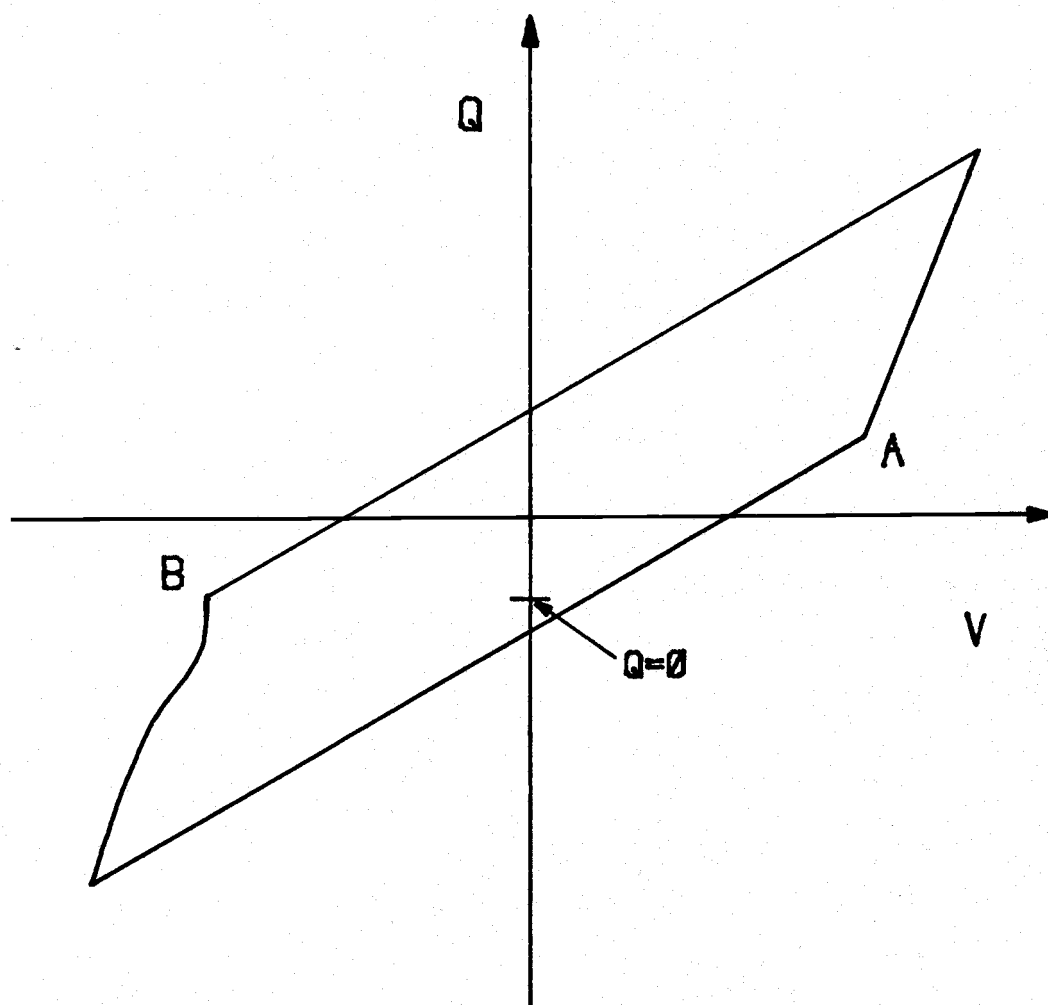


Figure 8.6 The Q-V diagram of an asymmetric ACTFEL sample with  $\text{Y}_2\text{O}_3$  on one side of the ZnS film and with  $\text{Al}_2\text{O}_3$  on the other side. Figure showed an offset on the Y-axis and a negative resistance effect associated with only the cycle where the voltage at the aluminum dot is negative.

interface on the  $Y_2O_3$  side. For samples with both insulator layers made of  $Al_2O_3$  no hysteresis effect, regardless of their  $Mn^{+2}$  concentrations, has been observed. This indicates that, although the field enhancement effect may exist due to the properties of the ZnS film, the negative resistance behavior will not occur unless the density of interface states also fulfills the requirement.

One effect resulting from decreasing  $X_0$ , is that the positive space charge density  $\sigma_1$  will be increased, since the increased collision rate and a higher biasing field provides more possibilities for the positive charge generation to occur. This will lead to a large ZnS polarization level. From figure 3.16 it is noticed that a larger polarization level is indeed associated with samples having higher  $Mn^{+2}$  concentrations. All the suggested procedures mentioned above, are geared toward creation of a higher polarization level, this will correspond to having a larger  $\alpha$  factor, the effects of which have been discussed in chapter three.

### 8.3 Transitions Between The Hysteretic And Nonhysteretic States Via Electrical Control

According to the negative resistance model just described, it is seen that some features which control the device hysteresis are determined by the physical structure of the device, such as the insulator capacitance, the ZnS thickness, the  $Mn^{+2}$  concentration, and the insulator material next to the ZnS film. However, a partial control of the factors described in the model which influence the device hysteretic behavior, can be achieved by appropriate design of the



driving voltages. This is discussed in the following.

It was seen that a stronger negative resistance effect will induce a larger device hysteresis width. In order for an electron to acquire enough kinetic energy between collisions to generate positive space charge over a short distance, i.e., to reduce  $X_0$ , increase  $\sigma_1$ , and therefore increase the negative resistance effect, a high effective electric field strength is needed. Due to the a.c. nature of the device operation, a higher effective electric field strength can be achieved if the driving voltage has a faster rise time. Experimental results also show that for a sinusoidal driving voltage the hysteresis width is larger if the driving frequency is higher, and the hysteresis width will also be larger if instead of the sinusoidal driving wave, a square wave or a pulsed wave is used, these are all the results of having a faster rise time.

With the driving voltage sustained in the hysteretic regime, the electric field strength induced by the sustaining voltage alone will not be able to trigger the ZnS conduction current. However, if the sample has been turned on, a bulk positive space charge will be created by the driving voltage which forms a polarization field. This field, when superimposed on the following driving pulse of the opposite polarity, will be able to initiate the ZnS conduction current and induce the negative resistance effect, which in turn maintains the sample in its on state. Suppose that before the sustaining driving pulse arrives, the space charge distribution was altered such that the polarization field strength at the would-be cathodic inter-

face becomes small, the effective electric field strength under the next sustaining pulse would then be small and the negative resistance effect is reduced. It has been shown that by appropriate tailoring of the driving voltage waveform, the above supposition can actually be achieved. Figure 8.7 shows one such a tailored driving waveform which has been used.

The pedestal voltage has a pulse width of  $100\ \mu\text{s}$  and an amplitude of  $V_p$  volts, the spike voltage on top of it has a pulse width of  $2\ \mu\text{s}$ , an amplitude of  $V_s$  volts, and a delay time of  $40\ \mu\text{s}$  with respect to the rising edge of the pedestal voltage. The B-V curves of a hysteretic sample under such a driving waveform and with a number of different choices of the pedestal voltage, are shown in figure 8.8. The B-V loops were traced out by plotting the device brightness against the amplitude of the spike voltage while holding the pedestal voltage at a specific level. Notice that figure 8.8 shows that the sample made a transition from the high hysteric state to the low hysteric state as the pedestal voltage changes from 90 volt to 100 volt. The detailed mechanism for this transition is as follows:

After the previous driving voltage has established a polarization field, the next excitation voltage that the sample will see is the pedestal voltage  $V_p$  of the following driving pulse after a delay of  $t_d$  seconds. When  $V_p$  is very small, such that even if with the help from the polarization field, few trapped electrons at the cathodic interface can be tunneled out from their trapping centers under the influence of  $V_p$ , as  $V_s$  arrives, the device will see a situation as

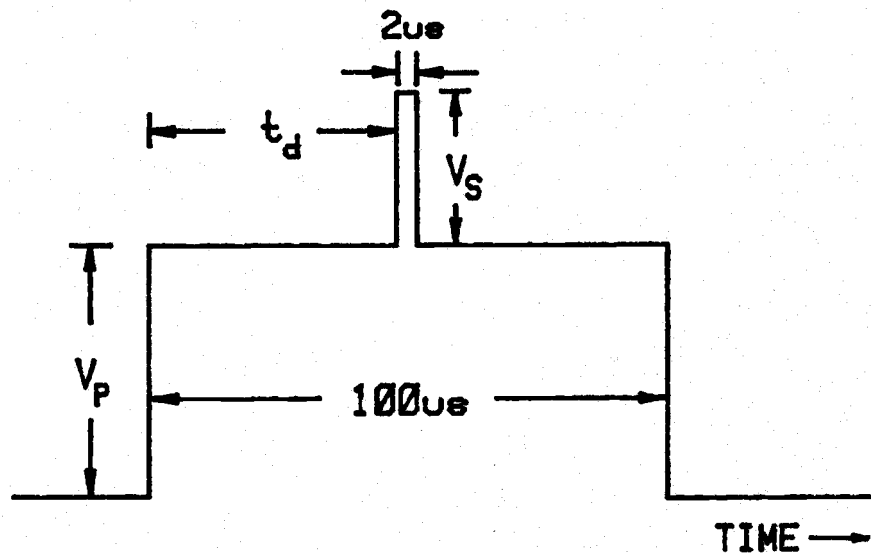


Figure 8.7 The waveform used for electrical control of the hysteresis behavior.

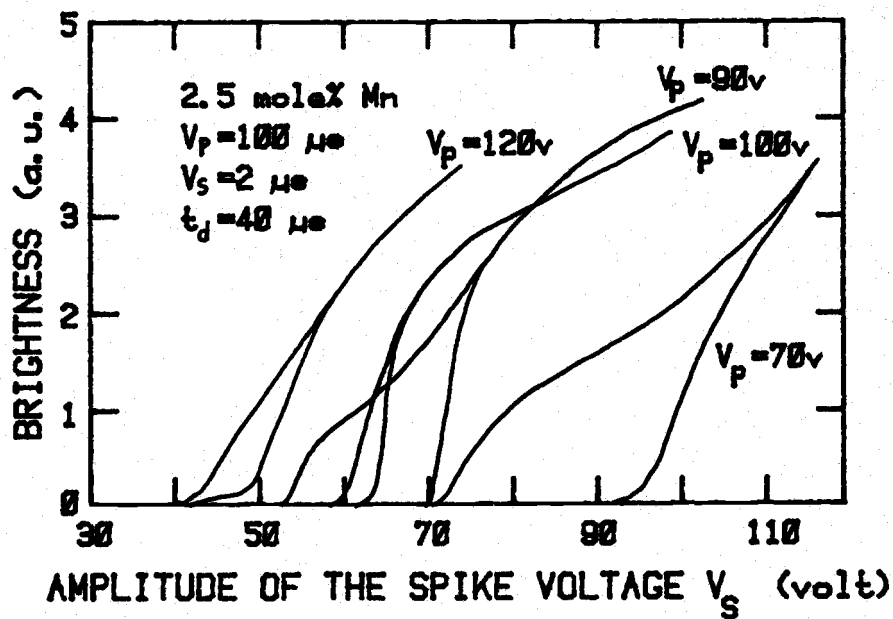


Figure 8.8 The effect of the spike driving waveform, shown in figure 8.7, on the hysteresis behavior of a hysteretic ACTFEL device.

if it were excited by a narrow pulse voltage having a pulse width the same as  $V_S$ . Therefore the sample will exhibit the normal hysteretic behavior. If  $V_P$  is now set at a higher level such that with the assistance of the existing polarization field, it can cause a significant amount of interface electrons to be tunneled out from their trapping states over the time period  $t_d$  prior to the arrival of the spike voltage  $V_S$ . Those released electrons will then see a weak accelerating electric field strength and thus can acquire only small kinetic energies between collisions, therefore will probably not be able to cause positive space charge generation. Nevertheless, these electrons will change the ZnS polarization field and reduce the effective field strength within the ZnS to a level dependent upon the total number of such electrons. As the following spike voltage  $V_S$  arrives, the effective electric field strength at the cathodic ZnS-insulator interface that can be induced by it, will now be smaller than that while the pedestal voltage was small. According to the negative resistance model, if the electric field strength at the cathodic interface region is too weak, it will make the generation of positive space charge at a short distance away from the cathodic interface difficult. This strongly disfavors the occurrence of a negative resistance effect and the sample is therefore, switched to the non-hysteric state.

#### 8.4 Discussions

In this chapter, a model for the fundamental mechanism responsible for the hysteretic behavior of the ZnS:Mn ACTFEL devices, the negative

resistance effect, was described. The model, although based on some crude assumptions, successfully interprets a number of observed phenomena associated with the hysteresis samples. Further computer simulation of this model suggests several methods for acquiring better hysteretic samples. Some of the suggestions are in good agreement with experimental results, whilst some of them have yet to be verified. Nonetheless, applications of this model have disclosed a way to control the device hysteretic behavior electrically by appropriate tailoring the shape of the excitation voltage.

## CONCLUSIONS

In this thesis, the electrical and optical characteristics of ZnS:Mn ACTFEL devices were investigated. This research has characterized many interesting properties of the device via a number of newly developed experimental techniques. These measurements resulted in results which allow a better understanding of the fundamental physical processes controlling the behavior of these ACTFEL devices. The results accomplished in this study are now summarized.

The basic properties of the ACTFEL device which are important for a practical display device were studied in chapter III. The discussions include the principle of light emission and the electronic structure of the  $\text{Mn}^{+2}$  luminescent dopant. The  $\text{Mn}^{+2}$  ion within the ZnS active layer are in an isoelectronic state and therefore are stable under high electric field operation. The unique feature of the device which has many potential applications - the memory effect - was also introduced. A phenomenological model for electrically triggering the on and off states of the electroluminescence of a memory ACTFEL device, sustained in its memory regime, was developed in the final section of this chapter.

Chapter IV was devoted to a study of the time resolved spectra of the ACTFEL devices, where in addition to the normal yellowish  $\text{Mn}^{+2}$  emission band, a fast decaying broad self-activated emission band was observed. This broad emission band provides a convenient way to compare the relative average kinetic energy of the hot electrons associated with the device electroluminescent behavior.

In chapter V, results of systematic observations of temperature effects on the ACTFEL devices were reported. A model for the nonradiative decay process of an excited  $\text{Mn}^{+2}$  ion was introduced which explained the temperature and  $\text{Mn}^{+2}$  concentration dependence of the nonradiative decay activity. The study also showed that tunneling is the dominant process for primary carrier generation because that the electrical characteristics are largely independent of temperature over a wide temperature range.

The subsequent two chapters, VI and VII, are devoted to study the trap distribution within the  $\text{ZnS:Mn}$  ACTFEL devices. The newly developed experimental techniques used for this purpose include both the thermal and the optical probing methods. Data indicates that deep levels exist in both the  $\text{ZnS}$  and the  $\text{Y}_2\text{O}_3\text{-Al}_2\text{O}_3$  insulator layers. The  $\text{ZnS}$  trap levels were further found to be associated with  $\text{Mn}^{+2}$  doping, as well as with the device aging process. The photoconductivity measurement in chapter VII also suggested that more interface states were generated with the device aging process.

Chapter VIII is a condensation of all the previous work, where a model for the device memory behavior was proposed. A computer simulation of this model for a simple and ideal situation suggested that in order to have a better memory characteristics for an ACTFEL device, certain practices can be adopted. These include:

- (i) Maximization of the ratio of the insulator capacitance to the  $\text{ZnS}$  capacitance.
- (ii) Increase of the  $\text{ZnS}$  film thickness.
- (iii) Minimization of the distance at which a hot electron tunneled out from the interface state will generate a

positive space charge. This can be achieved by doping the ZnS film with more  $\text{Mn}^{+2}$  ions, which introduce trap states and scattering centers into the ZnS.

- (iv) Maximization of the interface state density by choosing the appropriate insulator material next to the ZnS film.

Finally, an application of this model was made to achieve an electrical control of the memory behavior of the ACTFEL device, where the samples were switched between its memory and nonmemory states by appropriate tailoring the driving voltage waveform.

Possible future work which may provide more understanding of the ACTFEL devices include:

- (i) Studies of the temperature dependence of the broad self-activated emission band, as well as the driving waveform effect, on differently doped samples, to give better understanding of the transport properties of the hot electrons. This is important in terms of clarifying the  $\text{Mn}^{+2}$  excitation efficiency and the scattering mechanism associated with the device electroluminescent efficiency.
- (ii) When using the tailored driving waveform discussed in chapter VIII, it was found that if instead of sweeping the spike voltage  $V_S$ , the pedestal voltage  $V_P$  was swept, some interesting structures were observed in the B-V and P-V curves. This appears to be related to the trap distribution within the ACTFEL device. Therefore this measurement might well be developed to provide a fast and



simple method of characterizing the trap distribution within the device.

- (iii) Examination of the structure of the interface states within the ACTFEL devices and identification of the physical processes affecting the trap distribution, might provide results enabling a better control over the device hysteresis behavior.
- (iv) Studies of the insulator properties and correlate subsequent results with the device aging characteristics. It was reported that the threshold voltage of an ACTFEL device whose  $\text{Al}_2\text{O}_3$  insulators were fabricated by the atomic layer epitaxy (ALE) technique, changed by a much smaller amount in comparison with the electron beam evaporated insulators. This may be due to the better insulator property of the ALE films. An understanding of this effect is very important in solving the problems which originate in the device aging process.

## BIBLIOGRAPHY

- [1] A. Chiang, "Electrophoretic Displays: The State of The Art", conference record of the Biennial Display Research Conference, Oct. 1980, N.J., P. 10.
- [2] W.E. Howard, "Electroluminescent Technology and Characteristics", SID mtg., San Diego, Apr. 1980, session S-3, P. 77.
- [3] T. Inoguchi, M. Takeda, Y. Kakiyama and M. Yoshida, "Stable High Luminance Thin-Film Electroluminescent Panels", Digest 1974 SID Int. Symp., Los Angeles, 1974, P. 84.
- [4] J.M. Hurd and C.N. King, "Physical and Electrical Characterization of co-deposited ZnS:Mn Electroluminescent Thin Film Structures" J. Electronic Materials, Vol. 8, No. 6, P. 879, 1979.
- [5] D.A. Cusano, "Thin Films and Electro-Optical Effects", Physics and Chemistry of II-VI Compounds, North-Holland Publishing Co., 1967, P. 716.
- [6] Private communications with R. Tuenge at Tektronix.
- [7] W.E. Howard, "Memory in Thin Film Electroluminescent Devices", to be published in J. of Lum. 1981.
- [8] C.B. Sawyer and C.H. Tower, "Rochelle Salt as a Dielectric", phys. Rev. Vol. 35, P. 269, 1930.
- [9] D.H. Smith, "Electrical and Optical Characteristics of Thin-Film Electroluminescent Devices and Device Models", IEEE Trans. Electron Devices, Vol. ED-26, P. 1850, 1979.
- [10] V. Marrello, W. Ruhle, and A. Onton, "The Memory Effect of ZnS:Mn AC Thin-Film Electroluminescence", Appl. phys. lett., Vol. 31, No. 7, P. 452.
- [11] F.A. Cotton, "The Crystal Field Theory", Chemical Applications of Group Theory, John Wiley & Sons, Inc., New York and London, P. 215, 1964.
- [12] Y. Yamauchi, H. Kishishita, M. Takeda, T. Inoguchi, and S. Mito, "Red Electroluminescence From ZnS:Mn-F Thin Film", Digest 1974 Int. Elect. Dev. Mtg., (IEEE, New York, 1974), P. 352.
- [13] D. Curie and J.S. Prener, "Deep Center Luminescence", Physics and Chemistry of II-VI Compound, North-Holland Publishing Co., 1967, P. 473.

- [14] D.S. McClure, "Optical Spectra of Exchange Coupled  $Mn^{+2}$  Ion Pairs in  $ZnS:Mn$ ", The J. of Chem. Phys., Vol. 39, No. 11, P. 2850, 1963.
- [15] D. Langer and S. Ibuki, "Zero Phonon Lines and Phonon Coupling in  $ZnS:Mn$ ", Phys. Rev. A, Vol. 138, P. 809, 1965.
- [16] D. Curie, "Luminescence Centers", Luminescence in Crystals, John Wiley & Sons Inc., New York, 1963, P. 122.
- [17] J.C. Slater, "The Vector Model of the Atom", Quantum Theory of Matter, 2nd edition, 1972, P. 202.
- [18] J.C. Slater, "The Hydrogen Atom", Quantum Theory of Matter, 2nd edition, 1972, P. 129.
- [19] See chapter five of this thesis.
- [20] J.L. Powell and B. Crasemann, "Time Dependent Perturbations; Transition Probability", Quantum Mechanics, Addison-Wesley Publishing Co., 1961, P. 401.
- [21] M. Mizushima, "Quantum Theory of Radiation Process", Quantum Mechanics of Atomic Spectra and Atomic Structure, W.A. Benjamin Inc., New York, 1970, P. 72.
- [22] D.C. Krupka, "Hot Electron Impact Excitation of  $Tb^{+3}$  Luminescence in  $ZnS:Tb^{+3}$  Thin Films", J. Appl. Phys., Vol. 43, P. 476, 1972.
- [23] S. Tanaka, H. Kobayashi, H. Sarsakura and Y. Hamakawa, "Evidence of the Direct Impact Excitation of Mn Centers in Electroluminescent  $ZnS:Mn$  Thin Films", J. Appl. Phys., Vol. 47, P. 5391, 1976.
- [24] H.-E. Gumlich, "Electro- and Photoluminescence Properties of  $Mn^{+2}$  in  $ZnS$  and  $ZnCdS$ ", J. of Luminescence, 1981, (to be published).
- [25] F. Williams and D.C. Morton, "Some Recent Advances in Thin Film Electroluminescence", Presented at European Physical Society Mtg., Antwerp, W. Germany, April, 1980.
- [26] W.W. Piper and F.E. Williams, "Electroluminescence of single crystal of  $ZnS:Cu$ ", Phys. Rev., Vol. 87, PT. 1, P. 151, 1952.
- [27] W.E. Howard, "Memory in Thin Film Electroluminescent Devices", J. of Luminescence, 1981, (to be published).
- [28] See chapter four of this thesis.
- [29] D.H. Smith, "Modeling AC Thin-Film EL Devices", J. of Luminescence, July, 1981, (to be published).

- [30] W. Ruhle, V. Marrello, and A. Onton, "AC thin film Electroluminescences Filamentary Emission and its Memory Effect", J. of Luminescence, Vol. 18/19, P. 729, 1979.
- [31] H. Rufer, V. Marrello, and A. Onton, "Domain Electroluminescence in a.c. Thin-Film Devices", J. Appl. Phys., Vol. 51(2), P. 1163, 1980.
- [32] Y. Yamauchi, H. Kishishita, M. Takeda, T. Inoguchi, and S. Mito, "Inherent Memory Effects in ZnS:Mn Thin Film EL Devices", Digest 1974 Int. Elect. Dev. Mtg., (IEEE, New York, 1974), P. 348.
- [33] C. Suzuki, Y. Kanatani, M. Ise, E. Misukami, K. Inazaki, and S. Mito, "Optical Writing on a Thin-Film EL Panel with Inherent Memory", Digest 1976 SID Int. Symp., (Soc. of Inf. Display, Los Angeles, 1976), P. 52.
- [34] C. Suzuki, M. Ise, K. Inazaki, and S. Mito, "Optical Writing and Erasing on EL Graphic Display", Digest 1977 SID Int. Symp., (Soc. for Inf. Display, Boston, 1977), P. 90.
- [35] O. Cahni, W.E. Howard, and P.M. Alt, "Optical Switching in Thin-Film Electroluminescent Devices with Inherent Memory Characteristics", IEEE Trans. Electron Device, Vol. ED-28, No. 5, P. 459, 1981.
- [36] G. Vincent, A. Chantre, and D. Bois, "Electric Field Effect on the Thermal Emission of Traps in Semiconductor Junctions", J. Appl. Phys., Vol. 50(8), P. 5484, 1979.
- [37] O. Sahni, P.M. Alt, D.B. Dove, W.E. Howard, and D.J. McClure, "Device Characterization of an Electron-Beam-Switched Thin-Film ZnS:Mn Electroluminescent Face Plate", IEEE Trans. on Electron Devices, Vol. ED-28, No. 6, P. 708, 1981.
- [38] M.E. Dunham, D.H. Smith, C.N. King, and G. Barta, "A Storage CRT Using a Thin-Film Electroluminescent Screen", Digest 1980 Int. Elect. Dev. Mtg., (IEEE, New York, 1980), P. 711.
- [39] T. Inoguchi, C. Suzuki, and S. Mito, "Memory Effect in EL Devices Points Way to New Usages", Optoelectronic Devices, JEE, Oct., P. 30, 1976.
- [40] K.W. Yang, S.J.T. Owen, and D.H. Smith, "Energy Spectra of Bulk and Interface Trap States within ZnS:Mn AC Thin-Film Devices", extended abstract of the 159th Electrochem. Soci. Mtg., Minneapolis, 1981, P. 422.
- [41] Refer to chapter six and seven.

- [42] M. Yoshida, K. Yoshinobu, T. Yamashita, K. Taniguchi and T. Inoguchi, "The Mechanism of Inherent Memory in Thin Film EL Device", proceedings of the 9th conference on Solid State Device, Tokyo, 1977; Japan J. of Appl. Phys., Vol. 17, suppl. 17-1, P. 127, 1978.
- [43] M.S. Skolnik, "Time Resolved D.C. Electroluminescence Studies in ZnS:Mn, Cu Powder Phosphors", J. Phys. D., 1981, (to be published).
- [44] P.M. Alt, W.E. Howard, and O. Sahni, "On The Memory Behavior of Thin-Film Electroluminescent Devices", IEEE Trans. Electron Devices, Vol. ED-26, P. 1850, 1979.
- [45] M. Aven and J.S. Prener, "Deep Center Luminescence", Physics and Chemistry of II-VI Compounds, North-Holland Publishing Co., 1967, P. 448.
- [46] T. Koda, and S. Shinonoya, "Nature of the Self-Activated Blue Luminescence Center in Cubic ZnS:Cl Single Crystal", Phys. Rev., Vol. 136A, P. 541, 1964.
- [47] S. Shionoya, T. Koda, H. Katayama, "Decay Characteristics of Luminescence in ZnS Phosphors By Pulse Light Excitation", J. Phys. Chem. Solids, Vol. 26, P. 697, 1965.
- [48] V. Marrello and Onton, "Dependence of Electroluminescence Efficiency and Memory Effect on Mn Concentration in ZnS:Mn ACTFEL DEvices", IEEE Trans. Electron Devices, Vol. ED-27, No. 9, P. 1767, 1980.
- [49] G. Blasse, Luminescence of Inorganic Solids, B. Dibandjo, ed. New York, Plenum, 1977, P. 491.
- [50] K.W. Yang, S.J.T. Owen, and D.H. Smith, "Studies of Temperature Effects in AC Thin Film EL Devices", IEEE Trans. on Electron Devices, Vol. ED-28, P. 703, 1981.
- [51] M. Morita, "Photoacoustic Measurement of ZnS:Mn Phosphors", Japan. J. Appl. Phys., Vol. 20, No. 1, P. 295, 1981.
- [52] W. Busse, H.-E. Gumlich, B. Meissner, and D. Theis, "Time Resolved Spectroscopy of ZnS:Mn by dye Laser Technique", J. of Luminescence, Vol. 12/13, P. 693, 1976.
- [53] W. Busse, H.-E. Gumlich, W. Knaak, J. Schulze, "Analysis of Polymorphic Properties of ZnS(Mn) By Laser Spectroscopy", Int. Conf. on Phys. of Semicond., 1980.
- [54] D.L. Dexter, and J.H. Schulman, "Theory of Concentration Quenching in Inorganic Phosphors", The J. of Chem. Phys., Vol. 22, No. 6, P. 1063, 1954.

- [55] J.G. Simmons, G.W. Taylor, and M.C. Tam, "Thermally Stimulated Currents in Semiconductors and Insulators Having Arbitrary Trap Distribution", Phys. Rev. B, Vol. 7, No. 8, P. 3714, 1973.
- [56] K.H. Nicholas, and J. Woods, "The Evaluation of Electron Trapping Parameters From Conductivity Glow Curves In Cadmium Sulfide", Brit. J. Appl. Phys., Vol. 15, P. 783, 1964.
- [57] D.V. Lang, "Fast Capacitance Transient Apparatus: Application to ZnO and O Centers in GaP ; -n Junctions", J. Appl. Phys., Vol. 45, No. 7, P. 3014, 1974.
- [58] D.V. Lang, "Deep Level Transietn Spectrospy: A New Method to Characterize Traps In Semiconductors", J. Appl. Phys., Vol. 45, No. 7, P. 3023, 1974.
- [59] Private communication with C.N. King at Tektronix.
- [60] Y. Nigara, "Measurement of the optical constants of Yitrium Oxide", Jap. J. of Appl. Phys., Vol. 7, No. 4, P. 404, 1968.
- [61] N. Szydlo and R. Piorier, "Internal photoemission Measurements in a Metal -  $\text{Al}_2\text{O}_3$  - Si system", J. Appl. Phys., Vol. 42, No. 12, P. 4880, 1971.
- [62] F.L. Schuermeyer and J.A. Crawford, "Interpretation of low voltage photomeasurements in Metal - Insulator - Metal Films", Appl. Phys. Lett., Vol. 9, No. 8, P. 317, 1966.
- [63] A.S. Grove, Physics and Technology of Semiconductor Devices, New York, 1969, P. 496.
- [64] S.M. Sze, "Physics of Semiconductor Devices", John Wiley & Sons, New York, 1969, P. 496.
- [65] G.M. Martin, D. Bois, "A New Technique for The Spectroscopy of Deep levels in Insulating Materials, Application to The Study of Semi-insulating GaAs", Semiconductor Characterization Techniques, Electronics Division, Electrochemical Society, Proceedings, Vol. 78-3, P. 32, 1978.
- [66] G.F. Derbenwick, "Mobil Ions in  $\text{SiO}_2$ :Potassium", J. Appl. Phys., Vol. 48, No. 3, P. 1127, 1977.
- [67] M. Yamin, "Charge Storage Effects in Silicon Dioxide Films", IEEE Trans. Electron Device, Vol. ED-13, P. 256, 1966.
- [68] F.K. Harris, "Alternating Current Bridges", Electrical Measurements, New York, John Wiley & Sons Inc., 1952, P. 713.
- [69] R. Bube, Photoconductivity of Solids, John Wiley & Sons Inc., 1960, P. 59.

- [70] Refer to the RFIC measurement.
- [71] V. Marrello and A. Onton, "Electroluminescence Efficiency Profile of Mn in ZnS a.c. Thin-Film Electroluminescence Devices", Appl. Phys. Lett., Vol. 34, No. 8, P. 525, 1979.
- [72] R. Williams, "Dielectric Breakdown in Cadmium Sulfide", Phys., Rev., Vol. 125, P. 850, 1962.
- [73] R.C. Hughes, "High Field Electronic Properties of  $\text{SiO}_2$ ", Solid State Electronics, Vol. 21, P. 251, 1978.
- [74] R.C. Hughes, "Charge-Carrier Transport Phenomena In Amorphous  $\text{SiO}_2$ :Direct Measurement of The Drift Mobility and Life Time", Phys. Rev. Lett., Vol. 30, P. 1333, 1973.
- [75] J.J. O'Dwyer, "Theory of High Field Conduction in a Dielectric", J. Appl. Phys., Vol. 40, No. 10, P. 3887, 1969.
- [76] M. Shatzkes, M. Av-Ron, and R.M. Anderson, "On The Nature of Conduction and Switching in  $\text{SiO}_2$ ", J. Appl. Phys., Vol. 45, No. 5, P. 2065, 1974.
- [77] T.H. Distefano, and M. Shatzke, "Dielectric Instability and Break Down in  $\text{SiO}_2$  Thin-Films", J. Vac. Sci. Technol., Vol. 13, No. 1, P. 50, 1976.
- [78] Private communications with D.H. Smith at Tektronix.
- [79] Private communications with C.N. King and R. Coover at Tektronix.